

**STATIC AND DYNAMIC MODELING OF
DNA BIOSENSORS FOR BIOMEDICAL
APPLICATIONS**

**STATIC AND DYNAMIC MODELING OF DNA
BIOSENSORS FOR BIOMEDICAL APPLICATIONS**

By

M. Waleed Shinwari

Master of Applied Science

McMaster University

June 2007

A THESIS

SUBMITTED TO THE SCHOOL OF GRADUATE
STUDIES IN PARTIAL FULFILLMENT OF THE
REQUIREMENTS FOR THE DEGREE OF
DOCTOR OF PHILOSOPHY

McMaster University

Hamilton, Ontario, Canada

© Copyright by M. Waleed Shinwari, June 2011

DOCTOR OF PHILOSOPHY (2011)

McMaster University

(Electrical and Computer Engineering)

Hamilton, Ontario

TITLE: Static and Dynamic Modeling of DNA Biosensors for
Biomedical Applications

AUTHOR: M. Waleed Shinwari, M. A. Sc. (McMaster University)

SUPERVISOR: Prof. M. Jamal Deen

NUMBER OF PAGES: xvii, 171

Abstract

Achieving control over the construction and operation of microfabricated label-free DNA biosensors would be a big leap in the quest for highly reliable clinical laboratory tests. Whether it is for the purpose of food and water supply monitoring, early screening of diseases, routine walk-in medical checkups, or forensic analysis, controlled design of these sensors is essential. Reliable outcomes of critical medical tests mean less need for repetitions, earlier isolation of outbreaks, and even a better legal system. Nanotechnology has lent itself well to this purpose, with a plethora of work that attempt to produce highly sensitive and reliable nano-biosensors for detection of DNA strands. The problem of achieving a repeatable outcome is crude at best. Additionally, the mechanism of sensing in label-free Field-Effect based DNA sensors is still a matter of dispute. Simulation of the sensors using physical models can shed light into these mechanisms and help answer this question. Furthermore, computational calculations can allow designers to assess the importance of several parameters involved in the fabrication, and provides a framework to which experimental results can be compared.

In this thesis, the problem of modeling FET-based DNA hybridization sensors (named BioFET) is approached using mean-field simulation. Using the Finite-Element Method, a scalable model for the BioFET is produced and solved in 3D. The results are compared to an earlier work and we find that higher dimension physical modeling is essential for more realistic results. Additionally, we present a model for the impedance of the BioFET, which allows predictions of the change in the complex impedance of the sensor due to DNA hybridization, and which also allows the calculation of parasitic components that can contaminate the impedance measurements. Such components have been judged critical to proper characterization of impedance-based DNA biosensors.

The issue of variations in the sensed signal from the BioFET is addressed by performing hybrid Finite-Element/Monte Carlo simulations on the conformation of single-stranded DNA. A simplified model for the DNA is used. From electrostatic considerations alone, it is concluded that the change of conformation upon hybridization,

from a flailing chain to a stiff cylinder, is a main contributor to the induced signal. The hybrid simulation is then performed on a complete three dimensional BioFET, with emphasis on the positional variations of the DNA molecules on the sensitive surface. This computation yields an estimate for the amount of variation in the sensed signal due to the random placement of DNA molecules, and an estimate for the total signal-to-noise ratio is deduced.

In the Name of God, Most Merciful, Most Compassionate

Acknowledgements

I am very indebted to my supervisor, prof. M. Jamal Deen, for his support and encouragement throughout the course of my research. Without his guidance and support, this work would have not gotten off the ground. He has consistently pushed me to deliver my best, and I am very grateful to him for supervising me throughout the years.

I also would like to acknowledge my committee members: prof. Xun Li and prof. Ravi Selvaganapathy for their insightful ideas and guidance. They have always pointed me in the right direction with their experience and their contributions to this research are greatly appreciated. In addition, many thanks are due to the external examiner, prof. Thomas Thundat, for agreeing to be on my examining committee and for committing the time and resources to thoroughly read and comment on this thesis. I would also like to acknowledge prof. Bhagwati Gupta for chairing my defense and for his insightful comments.

I am grateful to the research team of the microelectronics laboratory here at McMaster University for giving me an unforgettable experience during my graduate studies. There are too many of them to fit this small area, but each and every one of them is remembered for contributing, in one way or another, to the success of this work. The support of my friends is also greatly appreciated. I would like to especially thank Dr. Munir El-Desouki and his wife Noora Dabbagh El-Desouki, Aalia Parker, Zuzana Wilcox and husband Joel, Mousa Kfourri, Robert Karam, Salma Trabelsi-Roberts and husband Matthew, Vista Eydatollah, Lara Ghaddar, Mostafa El-Sayed, Sherif Abdou, Ibrahim Sheerah, Rayan Mufti, Waleed Kabli, Eyad Al-Huthail, Turki Al-Shuail, Mohammad Hamed, Thamer Al-Rumaih, Ismail Al-Ani, Faris Al-Hammadi, and the countless other great friends that I have, for all their encouragement and support.

Next, I would like to extend my thanks to Dr. Khalid Al-Biyari and Mr. Ziad Al-Musallam, for standing beside me throughout this entire journey and providing their help

and support in many different ways. The encouragement and support of my professors at the undergraduate levels, prof. M. Taher AbuelMa'atti, prof. Alaeddin Amin, prof. M. Saber Musazay, and prof. Nawar Tabet, are gratefully acknowledged.

Finally, I would like to thank my family: My father, prof. M. Anwar Shinwari, my mother, Kamila Shinwari, my brothers Daoud, Fareed (whom I also thank for facilitating computational resources for my work), Merwaise, and Noor Ahmad, and my sisters Neptune, Mahera, Zakiya, Jameela, Zarghuna, and Tasneem. Thank you all for being there for me.

Table of Contents

Abstract.....	iii
Acknowledgements.....	vi
Table of Contents.....	viii
List of Figures.....	xi
List of Tables.....	xvii
INTRODUCTION.....	1
1.1 Biosensor Technologies.....	1
1.2 DNA Biosensors.....	9
1.3 The Need for Mathematical Modeling.....	15
1.3.1 Explaining Experimental Observations.....	16
1.3.2 Optimizing the Design and Operation of the Biosensor.....	17
1.3.3 Investigating Novel Phenomena.....	18
1.3.4 Handling Complex Geometries.....	18
1.3.5 Integration with Existing Numerical Packages.....	19
1.4 Main Contributions of this Thesis.....	20
1.5 Organization of this Thesis.....	23
MATHEMATICAL MODELING STRATEGIES.....	24
2.1 Introduction.....	24
2.2 Physics Required for Characterizing the BioFET.....	25
2.2.1 The DNA Molecule.....	25
2.2.2 The Electrolyte.....	30
2.2.3 The Insulator's Surface.....	37
2.2.4 The Reference Electrode.....	42
2.2.5 The Semiconductor.....	44
2.3 Modeling Strategies.....	46
2.3.1 Ab-initio Methods.....	47
2.3.2 Molecular Dynamics.....	49

2.3.3 Monte-Carlo Model	51
2.4 The Finite-Element Method	52
2.4.1 The Variational Principle	52
2.4.2 The Finite Element Discretization and Meshing	56
2.4.3 Solving the System	62
2.5 Summary	63
HIGHER DIMENSION MODELS OF DNA BIOSENSORS	64
3.1 Introduction	64
3.2 Goals of Higher Dimensional Modeling	64
3.3 Basic Geometry and Equations	65
3.3.1 Two-Dimensional Case	65
3.3.2 Three-Dimensional Case	75
3.4 Numerical Conditioning	77
3.5 Numerical Results and Design Implications	78
3.6 Other Effects	86
3.7 Summary	94
IMPEDANCE MODEL FOR FET-BASED DNA SENSORS	96
4.1 Introduction	96
4.2 Sources of Frequency Response	96
4.3 Model Details	98
4.4 Simulation Results	106
4.5 Other Effects	113
4.5.1 Electrolyte Concentration	113
4.5.2 Drain Bias	116
4.5.3 Steric Effects	119
4.6 Summary	122
MONTE-CARLO SIMULATIONS ON DNA BIOSENSORS	123
5.1 Introduction	123
5.2 MCM-FEM Model of DNA Conformation	123

5.2.1 Hemispherical Model.....	124
5.2.2 Basic Statistical Model of DNA Polymers	127
5.2.3 Simplified Model of DNA	131
5.2.4 Results.....	136
5.3 MCM-FEM Model of DNA Distribution within the BioFET	140
5.3.1 Evidence for DNA aggregation.....	141
5.3.2 Monte Carlo Model.....	144
5.3.3 Results.....	145
5.4 Conclusion	150
SUMMARY, CONCLUSIONS, AND FUTURE WORK	151
6.1 Thesis Summary and Main Contributions	151
6.2 Future Work	152
6.2.1 Quantum Modeling of Nanowire Sensors.....	153
6.2.2 Hybrid Methods	156
6.2.3 Modeling Reaction Kinetics of the Biosensor	158
6.2.4 Modeling of Filtration and Purification of DNA	159
References.....	161

List of Figures

Figure 1.1 Gram staining of mixed bacteria, showing purple (Gram positive) and pink (Gram negative) bacteria. Source: www.wikipedia.org	2
Figure 1.2 The Fuchs NBC Reconnaissance Vehicle. Source: www.wikipedia.org	3
Figure 1.3 Schematic of an electrode-based glucose sensor	3
Figure 1.4 Steps of replicating DNA fragments using PCR and a primer	4
Figure 1.5 Simplified schematic of Southern blotting technique	5
Figure 1.6 Illustration of affinity biosensors, with immobilized probes on a transducer surface, surrounded by potential targets in a test solution	6
Figure 1.7 (A) Number of publications on biosensing related topics by year (source: ISI web of Knowledge). (B) Number of patents granted to inventions in the biosensing industry by year (source: Google patents search).	8
Figure 1.8 Illustration of good vs. poor immobilization of probes	12
Figure 1.9 Esterification reaction, used to link the oligonucleotide with alkanethiols.	13
Figure 1.10 Simplified structure of a DNA BioFET, shown with the bias applied	14
Figure 1.11 Number of transistors (reflecting computational power) for common commercial processors, with the dashed line showing Moore's law trend [69].	16
Figure 2.1 Structure of the DNA molecule [75]	26
Figure 2.2 Electron density map for a DNA base pair (Adenine-Thymine) [80]	28
Figure 2.3 Coarse-grained model of DNA for molecular dynamics calculations [85]	30
Figure 2.4 Electrical potential (left) occurs due to the presence of a net electric field due to the organization of ions. Chemical potential (right) is the reduction of the ion's energy due to surrounding by other ions and molecules, and the presence of chemical bonding and nonbonding forces between them.....	33
Figure 2.5 Illustration of osmotic pressure. Before any ions are dissolved, no net water molecules move across the semi-permeable membrane (left). As ions are dissolved, they trap a portion of the water molecules, which lowers the chemical potential of free water molecules, causing an influx of water through the membrane.	35

Figure 2.6 Concentration vs. coverage plots of some isotherms	39
Figure 2.7 Typical current-voltage characteristics of the three electrode types	42
Figure 2.8 In an outer-sphere reaction, electrons directly tunnel to/from the ions (left), whereas inner sphere reactions require an adsorption intermediate step (right).....	43
Figure 2.9 Forces in molecular dynamics simulation	50
Figure 2.10 Using a Monte-Carlo simulation to estimate the area of the inner complex curve (see text)	51
Figure 2.11 Example of a triangular 2D mesh on a subdomain.....	57
Figure 2.12 Conforming mesh (left) and a non-conforming mesh (right), with the non- conforming edges dashed.....	57
Figure 2.13 Voronoi diagram (dashed), and Delaunay triangulation (solid) of the mesh nodes	58
Figure 2.14 Linear 1-D hat functions (left) and 2-D tent function (right)	59
Figure 2.15 Transformation of a triangular element from global coordinates to local coordinates using the Jacobian matrix	61
Figure 2.16 Illustration of a domain decomposition method using two overlapping domains.	63
Figure 3.1 2-D model of the BioFET with the DNA probes modeled as rectangles. Depth of the bulk was truncated to save page space.....	66
Figure 3.2 Chemical reactions at the OHP and the IHP between the electrode's surface states and the solutions components	70
Figure 3.3 Sample 2-D mesh for the BioFET. The mesh is made finer around the DNA molecules (not visible in this figure due to surrounding mesh) for added accuracy at the critical locations	75
Figure 3.4 Cartoon illustration of the 3-D slice of a BioFET with cylindrical DNA molecules placed randomly on the SAM surface. A tetrahedral mesh is applied to the entire domain for solving.....	76

Figure 3.5 Top view of the 3-D BioFET channel. Periodic boundary conditions applied to the top and bottom boundaries in the figure allow spillover charge profiles to be reflected to the opposite boundary, causing a bulk effect overall.....	77
Figure 3.6 Comparison of the 1-D, 2-D, and 3-D simulation of the drain current in the BioFET with similar characteristics.....	79
Figure 3.7 Comparison between the simulated hybridization current changes in 1-D, 2-D, and 3-D models, showing the drastic reduction in case of the 3-D model.	81
Figure 3.8 Relative sensitivity of the BioFET between: A) 2-D and 1-D models, B) 3-D and 1-D models	81
Figure 3.9 Variation in the hybridization current change with positioning of the DNA molecules along the channel's length	83
Figure 3.10 Shift in the average surface potential of the BioFET as a function of the electrolyte concentration, in the case of a perfect SAM monolayer and an ion-permeable layer.....	84
Figure 3.11 Simulated output current for three cases: 1) With one source-drain polarity, 2) with an inverted polarity, and 3) the averaged result of these two measurements	85
Figure 3.12 Simulated response of BioFET to hybridized charge, and to charge from spurious nonspecific molecules	86
Figure 3.13 Simulated inversion charge under the DNA molecule at different electrolyte concentrations. (Inset: percentage relative error in simulation with and without steric effects, as a function of the electrolyte concentration)	89
Figure 3.14 Inversion charge change upon hybridization as a function of the electrolyte concentration for two different biases. Each simulation is carried out twice, with and without a permeable DNA molecule. (Inset: percentage relative error in simulation with and without permeation, as a function of the electrolyte concentration)	91
Figure 3.15 Hybridization inversion charge with several different buffers. Dashed lines are the results with ideal buffering capability, whereas solid lines neglect the buffer solution.....	93
Figure 3.16 Charge-potential curves for proton adsorption on SiO ₂ [4].....	94

Figure 4.1 Different current components across the BioFET key interfaces [149]	101
Figure 4.2 A sample reaction energy diagram. The forward and reverse reaction energies are only the same for a completely reversible reaction in equilibrium.....	103
Figure 4.3 Simulated CV diagram of the FET, with the body and contacts capacitances separately shown.....	108
Figure 4.4 Capacitances in a FET structure	108
Figure 4.5 Comparison of the CV diagram of a regular FET and a BioFET, showing the shift due to the presence of DNA molecules and the electrolyte solution	109
Figure 4.6 Differential capacitance change due to hybridization as a function of the gate bias, showing that the onset of inversion and accumulation result in the maximum sensitivity	110
Figure 4.7 Electrochemical admittance diagram for the BioFET. The sweep is from deep accumulation to deep inversion	111
Figure 4.8 Nyquist plot for the relative change in the admittance of the BioFET upon hybridization in inversion. (Inset: absolute change in admittance in accumulation).....	112
Figure 4.9 Absolute change in the admittance of the BioFET in inversion. The anomalous negative change in admittance in deep inversion are clearly seen.....	113
Figure 4.10 Nyquist diagram of the admittance change due to hybridization of DNA, for different electrolyte concentrations.....	114
Figure 4.11 Nyquist diagram of the admittance change in a BioFET for low frequencies	116
Figure 4.12 Nyquist plot of the change in the transconductance of the BioFET	118
Figure 4.13 Relative change in the admittance of the BioFET due to hybridization, with and without steric effects included	121
Figure 5.1 Conformation of single and double-stranded tethered DNA.....	125
Figure 5.2 Comparison of the simulated BioFET signal with and without geometry considerations	126
Figure 5.3 Illustration of charge distribution before and after hybridization of the hemispherical DNA, showing the regions of local depletion (see text).....	127

Figure 5.4 Freely-Jointed Chain model, showing the links and the nodes	129
Figure 5.5 Comparison of the spherical Gaussian distribution (Equation 5.2) and the summed Gaussian (Equation 5.5)	130
Figure 5.6 Ball and stick model used for the MCM simulation.....	132
Figure 5.7 Atomic organizational structure of a DNA backbone	133
Figure 5.8 Superimposed conformation profile of the single stranded DNA molecule throughout the Monte Carlo simulation, without energy bias (left) and with energy bias (right).	137
Figure 5.9 Histogram of the simulated radial (left) and angular (right) positions for the DNA segments.	138
Figure 5.10 A sample conformation from the MCM-FEM algorithm.....	138
Figure 5.11 Histogram of the DNA conformation with a reference electrode bias of -1V.	140
Figure 5.12 Simulated potential profile with six DNA molecules.....	142
Figure 5.13 Total free energy of the system of six DNA molecules as a function of their inter-distance, at different electrolyte concentrations	143
Figure 5.14 Grid used to place the randomized DNA molecules	144
Figure 5.15 Mean BioFET signal for different DNA probe densities	146
Figure 5.16 Resistor network used to examine the conductance sensitivity of the BioFET's channel to parallel and series image charges	146
Figure 5.17 Calculated standard deviation of the observed BioFET current for different Monte Carlo runs	147
Figure 5.18 Signal-to-noise ratio, as simulated for different DNA densities. Inset: magnified signal-to-noise-ratio for 50 DNA molecules as a function of source-drain bias	148
Figure 5.19 Comparison of the signal histograms for different DNA probe densities, at different electrolyte concentrations.....	150
Figure 6.1 Possible hybrid FEM/MD model for the BioFET, emphasizing variations in the double layer through accurate MD simulations	157

Figure 6.2 Illustration of the overlap between nonlocalized Ab-initio elements and FEM elements in a hybrid model	157
Figure 6.3 Different possibilities during DNA probe-target hybridization	158

List of Tables

Table 1.1 Biosensor companies and their emerging technologies	9
Table 2.1 Physical phenomena showing Fickian behavior	36
Table 2.2 Several common isotherms and their uses	40
Table 2.3 Some common basis sets used in computational chemistry	48
Table 3.1 The change in simulated sensitivity as a function of different variables	95
Table 4.1 Permittivity of water at various frequencies [143]	100

Chapter 1

INTRODUCTION

1.1 Biosensor Technologies

Biosensors can be used for various purposes: to detect complete organisms, isolated cells, or biomolecules. Organism biosensors are often optical-based, with a staining phase and a recognition phase. An example is Gram staining of bacteria (Figure 1.1). The recognition phase is often administered manually by a trained laboratory technician and a microscope, or more recently using image processing software and computers. An organism biosensor can also measure the abundance of most food and water-borne pathogens by measuring the amount of Adenosine-triphosphate (ATP) in a sample using photon-inducing labels [1]. Several commercial products based on staining assays are available and extensively used for food supply monitoring. Examples include the RedAlert™ product line from Merck, and the Mericon kits from Qiagen. In addition, several digitally-controlled assays are available for most common pathogens such as E. coli O157 and Salmonella. Examples of these are the Dynabeads® kit by Invitrogen and the BAX® Salmonella kit by Dupont Qualicon. However, these are highly customized biosensors that exploit certain traits of the target organism and cannot be extended to detection of other organisms. Additionally, specificity is not ensured since nonspecific staining can occur. Such biosensors are best suited for rapid testing of food supplies, and are not necessarily suitable for low concentration, high sensitivity analyte detection.

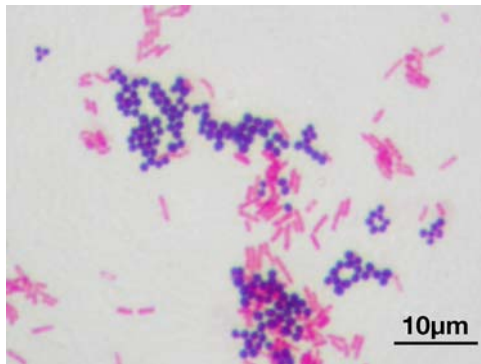


Figure 1.1 Gram staining of mixed bacteria, showing purple (Gram positive) and pink (Gram negative) bacteria. Source: www.wikipedia.org

Biomolecular sensors cater to a different range of applications. Military bio-warfare vehicles, such as the Fuchs NBC reconnaissance vehicle (Figure 1.2), detect biochemical toxins in the environment using mass spectrometry. The extracted sample is purified and heated in an oven to very high temperatures such that the molecular bonds break and all atoms are ionized. This “soup” of atoms is taken to the mass spectrometer, with the outcome being a spectrum of relative abundance of atoms with different molecular masses. The spectrum is correlated against a database of spectra of several known toxins, and a warning is triggered when a high correlation coefficient is obtained. This method can be useful for detection of certain chemical agents like Sarin. The main drawback of this technique is the destruction of the molecular structure, which leads to ambiguity in discerning molecules with similar mass distribution but different biological significance. This method would, therefore, not be used when detecting DNA sequences or proteins.



Figure 1.2 The Fuchs NBC Reconnaissance Vehicle. Source: www.wikipedia.org

Another class of chemical biosensors exploits specific reactions of the analyte. Glucose sensors are perhaps the oldest example of this. Glucose sensors monitor the consumption of oxygen at a surface of an oxygen-rich electrode [1]. A layer of glucose oxidase, an enzyme, is confined to the surface of the oxygen electrode, as shown in Figure 1.3, and oxidation can be monitored by monitoring the electrochemical cell potential using the oxygen as a working electrode and an inert platinum counter electrode. Several alterations to the enzyme, the electrode, or the introduction of other species that mediate electron transfer, can alter the performance and sensitivity of the sensor. The electrochemical cell can be operated in the constant voltage (amperometric), or constant current (potentiometric) mode.

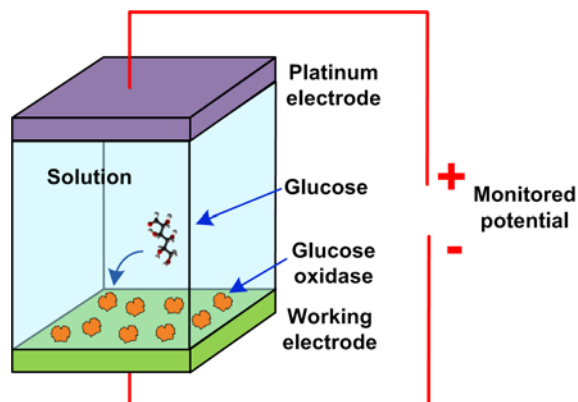


Figure 1.3 Schematic of an electrode-based glucose sensor

A very common technique in detecting biomolecules is the Polymerase Chain Reaction (PCR). Developed by Kary Mullis in 1983, PCR is a chemical technique for

rapid exponential replication of fragments of DNA using DNA polymerase enzyme and a short DNA primer [3] . Replication of the unknown target will occur only if the primer contains exactly complementary bases to a segment in the target (Figure 1.4). Successful replication, as measured by different labels, is therefore a direct evidence of the recognition of the primer's sequence. This method can, therefore, be used to identify a segment of an unknown DNA molecule, and correspondingly, the source organism [4] . The procedure of PCR is relatively simple. However, its success depends on many factors, including purity of the samples, efficient cycling of temperatures for the PCR and denaturation phases, and abundance of the labels, the polymerase enzyme, the primers, and suspended nucleotides in the solution. These issues make it hard to realize a portable, low cost biosensor based on PCR, despite its extreme sensitivity.

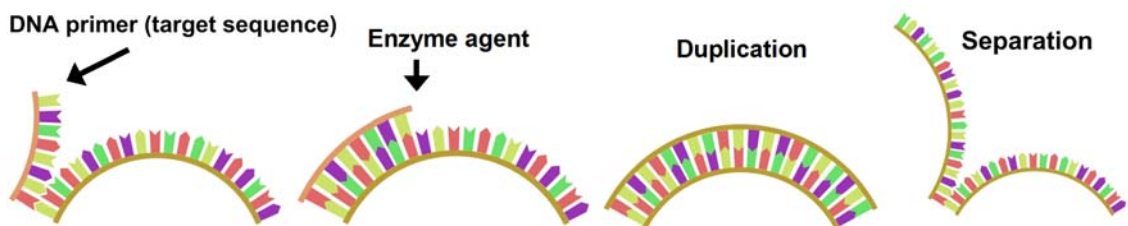


Figure 1.4 Steps of replicating DNA fragments using PCR and a primer

Affinity biosensors are considered state-of-the-art methods for detecting biomolecules. Their earliest manifestation was the blotting techniques, first introduced by Edwin Southern, and named the Southern blot. This was used to detect DNA fragments by hybridizing them to probes suspended in a gel matrix (Figure 1.5). Similar techniques were developed for detecting different biomolecules such as proteins and RNA molecules, and were eponymously named Western blot, Northern blot, Eastern blot and Southwestern blot. Contemporary solid-substrate biosensors use the same technique of specific recognition, but the detection takes place at a solid surface. DNA hybridization sensors can detect the presence of specific genetic material in a sample by means of the specific pairing of single-stranded DNA fragments (oligonucleotides or ssDNA). Several protein sensors can utilize antigen/antibody or receptor/ligand specific interactions to detect the presence of proteins with specific active sites. Detection of viruses can be done in this way, by detecting antibodies produced by the immune system in response to the

virus. This is the principle of operation of Enzyme-Linked ImmunoSorbent Assay (ELISA).

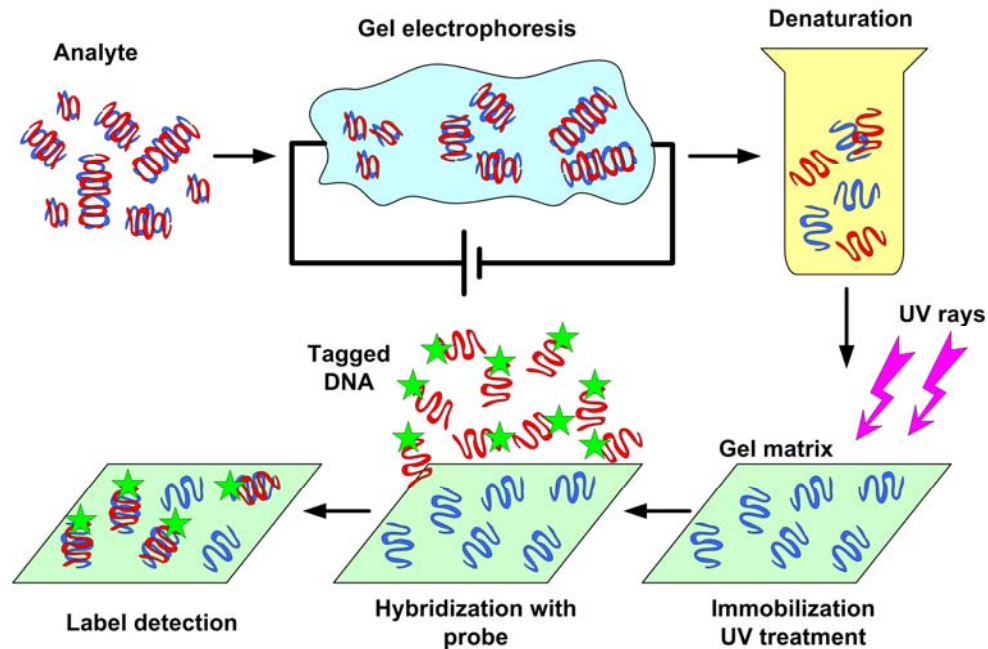


Figure 1.5 Simplified schematic of Southern blotting technique

Affinity biosensors (Figure 1.6) consist of a substrate, immobilized specific capture probes, and a test solution with the targets. Specificity is obtained by the unique affinity of binding between the probe and target. Although biomolecular sensors have been used for food and water monitoring, they are mostly used for gene expression profiling and single nucleotide polymorphism detection. Detection of successful capture is accomplished by first staining the targets with a fluorescent dye, generally a Cyanine dye like Cy3 or Cy5. The target and solution are applied to the sensor's surface, and a binding to the probes occurs if the sensed biomolecule is found in the solution. Detection of successful binding is done by monitoring the residual fluorescence obtained after washing away the test solution. Any remaining fluorescent molecules are attached to targets that have been captured, and the intensity of the observed fluorescence is proportional to the abundance of the molecule. These affinity sensors generally manifest as cells in a larger array, called a microarray. The microarray allows parallel detection of many species and yield extremely informative data about the target organism.

Microarrays are classified based on the target molecule (e.g. protein microarray and DNA microarray), or based on the method of fabrication, array density, or even the method of use (e.g. complementary DNA (cDNA) microarray and oligonucleotide microarray).

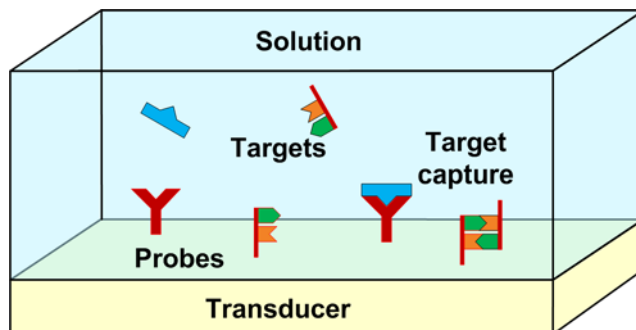


Figure 1.6 Illustration of affinity biosensors, with immobilized probes on a transducer surface, surrounded by potential targets in a test solution

Recently, much research effort [5] -[24] has been put into the development of label-free DNA and protein biosensors. The same technique of affinity biosensors is used: a specific interaction between probe and target molecules. The new technologies for detection can also, at least in principle, be grouped into microarrays. However, detection of successful target capture is measured by different means, eliminating the need for any kind of dyes. Several versions of label-free biosensors have been presented. Electrochemical biosensors detect the capture by monitoring its effect on electron transfer reactions at the bio-sensitive surface [5] -[8] . They can also be used for detection of specific chemical ions (ion-sensitive electrodes) or pH level [9] . Piezoresistive sensors have utilized Micro-Electro-Mechanical Systems (MEMS) to produce a deflection of suspended micro-cantilever beams due to target capture. This deflection modulates the properties of piezoresistive materials, causing a direct electrical readout [10] -[13] . Nanomaterials have recently attracted a lot of interest due to their high surface-to-volume ratio, enabling high sensitivity and the detection of a very small number of molecules [14] [18] . Nanowires [19] -[22] have been used to detect target capture by monitoring the direct effect of the capture on the conductive properties of the nanomaterial. Nanobeads attached to ssDNA probes would aggregate closer together, due to DNA hybridization,

which would modulate the localized surface plasmon absorption band, leading to a change in the observed color of the nanobeads [23] -[24] .

Although nanotechnology has pushed the limit for high sensitivity detection of the lowest possible concentrations (down to femtomolars), it remains too expensive to be commercialized. Alternatively, biosensors based on the field-effect [25] -[30] , allow very low-cost detection of biomolecules, and can be readily integrated with mainstream signal processing circuits on the same chip. This biosensor is based on post-processing mainstream **Field-Effect-Transistors (FETs)**, chemically attaching the probe molecules to the surface of the insulator, and replacing the gate connection with a reference electrode [9] [31] [33] . Capture of target molecules causes a shift in the threshold voltage of the FET structure, which, again, can be sensed in amperometric or potentiometric mode [34] [37] .

The current surge in biosensor technologies is mirrored by an equivalent surge in the area of microfluidics. Preprocessing of samples requires many steps such as mixing, heating, and separating of molecules using electrophoresis. Much work has been published on microfabrication of fluid channels and micro-chambers for these purposes [38] [45] . The goal is to replicate the processes of sample preparation and purification in micro-scale, using only nanoliters of fluid and a countable molecular ensemble. This allows smaller volume processing and cost reduction, as well as faster and more reliable results [46] -[47] . Many of the technologies used to build microfluidic systems are compatible with those used for integrated circuits, allowing the sensor devices and peripheral electronics to be integrated with fluid-processing systems. The offspring of this union is the so-called “lab-on-chip” or “micro-total analysis system” (μ TAS), which is an integrated chip that can replicate one or many functions of a complete lab, and provide results that are just as accurate, with minimal time and use of energy and chemicals.

The diverse spectrum of technologies that surround molecular biosensors stems from the increasing demand for research into reliable electronic biosensors that are cheap and easy to deploy. Figure 1.7a shows the growth in the number of publications that

address newer biosensor technologies. It shows an unambiguous tendency for research to target integrated label-free biosensors and microfluidic technologies that allow processing of small volumes of fluids, as compared to conventional blotting techniques which are on the decline. Similarly, newer biosensor technologies are taking a larger market share in the diagnostic industry, albeit at a much slower pace [48]. Figure 1.7b summarizes the growth of patents on biosensor technologies in the past two decades. As apparent from the figure, the innovative ideas that are being groomed for marketing mostly belong to newer biosensor technologies, such as microarrays and microfluidic assays. Legacy lab techniques have since fallen short of catching up with the newer technologies, and the increase in funding for biosensor research (estimated to reach USD 14.42 billion by 2016 [49]), will only widen this gap. Table 1.1 gives a summary of companies that are involved in emerging biosensor technology research.

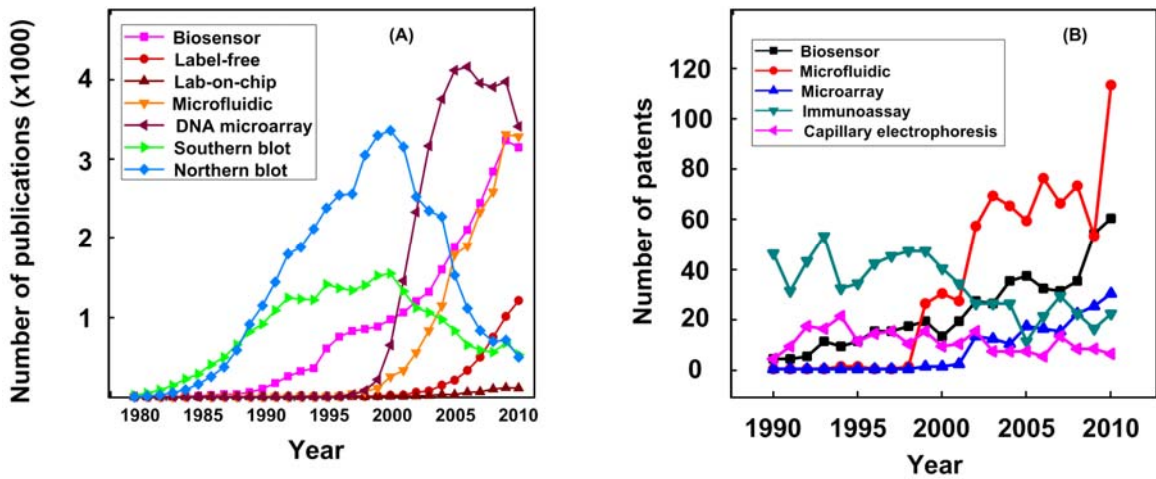


Figure 1.7 (A) Number of publications on biosensing related topics by year (source: ISI web of Knowledge). (B) Number of patents granted to inventions in the biosensing industry by year (source: Google patents search).

Table 1.1 Biosensor companies and their emerging technologies

<i>Company</i>	<i>Product(s)</i>	<i>Purpose</i>	<i>Website</i>
Affymetrix Inc.	Axiom™, GeneAtlas™	Gene expression profiling high density microarrays	www.affymetrix.com
Applied Biophysics	ECIS array station	Impedance measurement of cells to quantify cell behavior	www.biophysics.com
Applied Biosystems	TaqMan®	PCR/labeled microarray for detection of salmonella, lysteria, and other food-borne pathogens	www.appliedbiosystems.com
Attana sensor technologies	Attana sensor chips	Label-free quartz-crystal microbalance detection of molecules	www.attana.com
Biacore Intl. AB	Bioacore™	Label-free molecular interaction and kinetics analysis hardware and software	www.biacore.com
Biosensing Instrument	BI sensor chips	Surface-plasmon resonance based biosensing	www.biosensingusa.com
Cantion	CantiChip8	MEMS-cantilever based molecular sensing	www.cantion.com
Invitrogen	Luminex®	Protein assays for detection of intra- and extracellular proteins	www.invitrogen.com
LifeScan	OneTouch® UltraLink™	Glucose meters with wireless transmission	www.lifescan.com
Maven Biotechnologies	LFIRE™	Label-free internal reflection ellipsometry for detection of molecular binding	www.mavenbiotech.com
NeoGen	GeneQuence®	DNA microwell assay for pathogen detection	www.neogen.com
NimbleGen	ChIP-chip	Protein-DNA interaction analysis via microarrays for immunoprecipitation	www.nimblegen.com
Nova Biomedical	Bioprofile®	Cell culture analysis	www.novabiomedical.com
OWLS Sensors	OWLS	Label-free biosensor by modulation of laser propagation in waveguides	www.owls-sensors.com
QIAGEN	Mericon kits	PCR labeled assays for detection of organisms	www.qiagen.com

1.2 DNA Biosensors

Affinity biosensors that are made to detect DNA molecules have attracted special interest and have dominated biosensor research for several reasons:

1. DNA is the most stable biological molecule that contains information about the source organism, and is therefore the most likely to be stable over time and to provide accurate identification results. This makes it the ideal molecule for forensic or archaeological studies, as well as pathogen detection. A sensor built with DNA probes will also be more immune to degradation than a protein sensor.
2. The chemistry of DNA is far more understood than that of proteins or RNA, and a lot can therefore be done with DNA molecules (e.g. amplification using PCR, reverse transcription of RNA to DNA, separation by electrophoresis). Some of the biochemistry of DNA that occurs inside cells has allowed biochemists to replicate the experiment *in vitro* for other purposes. For example, restriction enzymes, found in bacteria, can cut portions of the DNA out of the bacterial genome. This mechanism is thought to be a defense mechanism against viral attacks. Biologists use this idea to cut up DNA molecules in labs to a more manageable size for lab experiments.
3. DNA molecules remain intact at higher temperatures, and denature at around 80°C. As temperature is lowered, the denatured DNA will self-recognize and “hybridize” once again. When proteins denature, it is impossible, without cellular machinery, for them to fold back into their original shape. This makes the design of DNA sensors more robust.
4. The pair-recognition property of DNA molecules is highly specific. A single mismatch for a ~20-mer probe can destabilize the complex such that its melting temperature is reduced by 5°C [50] . This makes detection using DNA strands extremely specific, given that the probe length is short enough for the mismatch to be significant, but long enough for global stability of the molecular complex.

On the other hand, the use of DNA molecules for organism detection has the limitation that it gives no information about the living state of the organism, whereas a positive RNA test is a good indication of the target being alive, since RNA cells are quick to degrade. Additionally, DNA sensors might not be sufficient for detecting diseases caused by prion infections, such as Creutzfeldt-Jakob’s disease. Such infectious agents

are diagnosed by highly-specialized protein conformation biosensors [51] , or by symptom monitoring of the disease.

The ability to synthesize DNA oligonucleotides allows for the low-cost design of DNA biosensor microarrays. A lithographic technique is used by Affymetrix [52] , and it allows for the low-cost synthesis of DNA probes directly onto the sensor. Label-free DNA sensors have also been built on many different substrates and materials, including gold and carbon [53] , silicon dioxide [54] , diamond [55] , quartz [56] , optical fiber [57] , and conducting polymers [58] . One of the challenges of building DNA sensors is the attachment of the probes to the substrate. DNA probes are expected to be intimately bond to the transducer's substrate. This is particularly important for sensors that rely on electron transfer reactions that travel along the DNA molecule [59] , but is also useful for all other types of transducers. ssDNA probes can be captured on a surface via long-range electrostatic forces, or by chemical attachment to an activated (or functionalized) surface. For a durable, highly sensitive biosensor, the following must be observed when immobilizing probe DNA:

1. The probe ssDNA molecule must be secured in its position, with little chance of breaking free. DNA Biosensors are rinsed before detection to allow unhybridized and non-complementary targets to be washed away, so as not to contaminate the measured results. If probes get washed away as well, the effective sensitivity of the sensor is lowered and the final reading can be ambiguous.
2. The probes should only attach at one terminus onto the surface, and be suspended otherwise into the host solution (Figure 1.8). This allows for the highest degree of thermodynamic freedom, which significantly speeds up the hybridization rate. Binding should not occur at the nucleotide bases, since those sites are the target capture sites.
3. The probes should not aggregate too close to one another. Close-packed DNA molecules can cause cross-hybridization between probes and can lead to reduction in the sensor's speed [60] . As will be seen later in this thesis, non-uniform

distribution of DNA probes will reduce the reliability and sensitivity of the biosensor.

- Any functionalization layer used should not compromise the functionality of the biosensor. This can occur if the functionalization layer prohibits electron-transfer reactions in an electrochemical sensor, or if it can repel target molecules away from the probes. Strong affinity between the surface and the probe can alter its shape, making hybridization less likely.

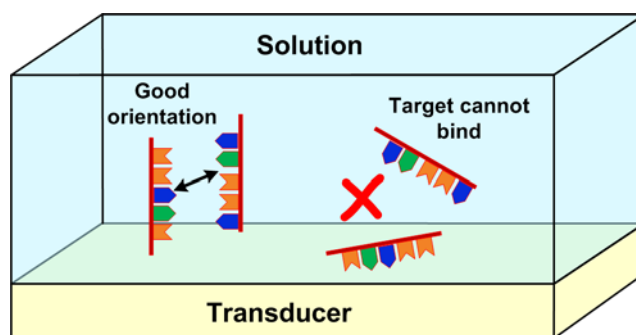


Figure 1.8 Illustration of good vs. poor immobilization of probes

For DNA sensors, many methods of binding have been reported. One popular immobilization technique is the use of thiol-gold chemisorption. The 5' end of ssDNA molecules are attached to an alkanethiol molecule, using an esterification reaction of the DNA and a related alcohol, such as 6-mercapto-hexanol [61]. This reaction is shown in Figure 1.9. The thiol group can be used to attach to many different metallic surfaces as well, although they might not be bio-compatible [62]. When designing DNA sensors using mainstream semiconductor technology, it is generally desired to attach the DNA molecules to a dielectric material, often silicon dioxide. For silicon oxide or silicon nitride, silane groups are used instead of thiols, as they can form a cross network on the surface and yield a very high quality Self-Assembled Monolayer (SAM) [63]. Common molecules in use are aminopropyl-triethoxysilane (APTES) [64], and glycidyoxypropyl-triethoxysilane (GPTES) [65]. These molecules form a cross-network with the underlying substrate on the silane end. The other end (amine in APTES and glycidyl in GPTES) is used to bind to the DNA molecule at the 5' end. The energy of this bond is critical to the stable operation of the biosensor. Improper covalent bonding can lead to the

probes being washed away during the rinse phase. It can also lead to lateral diffusion of the probes which can adversely affect the reliability of the sensor's reading.

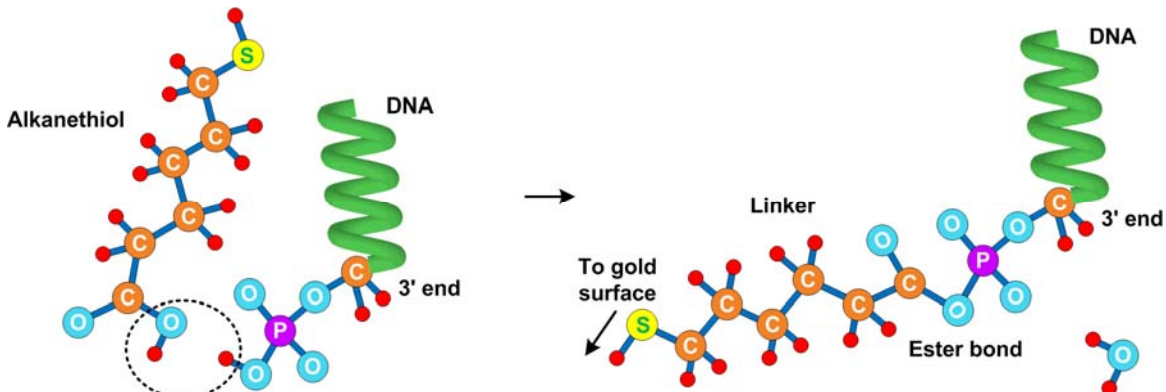


Figure 1.9 Esterification reaction, used to link the oligonucleotide with alkanethiols.

The success of a DNA sensor depends on the high specificity of capturing only the exact complementary target, allowing DNA sensors to detect Single-Nucleotide Polymorphism (SNP). For this, the DNA probes should be made short such that the energy of binding is severely changed with a single mismatch, prohibiting nonspecific pairing. Additionally, the probe density should be made high enough such that targets do not absorb and attach to vacant sites in the SAM layer. The vacant sites might be deactivated by a chemical step, but such processes are not perfect, and active sites can still exist. The hybridization experiment must be conducted in a buffer solution with carefully selected ionic concentration (often a saturated or near-saturated monovalent salt). This will allow the hybridized pair to achieve a local minimum in energy and remain stable.

Most label-free DNA sensors utilize the effects of hybridization on electron transfer at a surface as a means of transduction. This could be by modulating the electrochemical properties of the electrode by the DNA hybridization, or by steric (or perhaps electrostatic) blocking of ionic diffusion into the ssDNA brush layer [66]. The electrochemical reaction might not be with ions in the solution, but instead with a moiety, such as ferrocene, attached to the target DNA [67]. Although this does not qualify as strictly label-free, it does not require optical methods of detection, which still makes it an attractive option. Such means of transduction are extremely sensitive to the electrode's

surface characteristics, the thermodynamics of the electrochemical reaction, and the exact nature and chemistry of the SAM molecules. Field-effect DNA sensors, on the other hand, are less sensitive to the chemistries and electronic structures of the molecules, but more so to their charge, dipole moment, and geometry. A field-effect DNA sensor consists of a normal field-effect transistor, with a source terminal, a drain terminal, a channel, and a gate insulator. However, instead of the gate connection, which sets the potential of the channel, a bio-active membrane is placed on top of the insulator, and a reference electrolyte solution and reference electrode are added, as shown in Figure 1.10 [25] , [29] , [36] . Capture of target DNA molecules causes a modulation in the channel's resistance, which can be sensed as a change in the amount of drain current. This is equivalent to a shift in the threshold voltage.

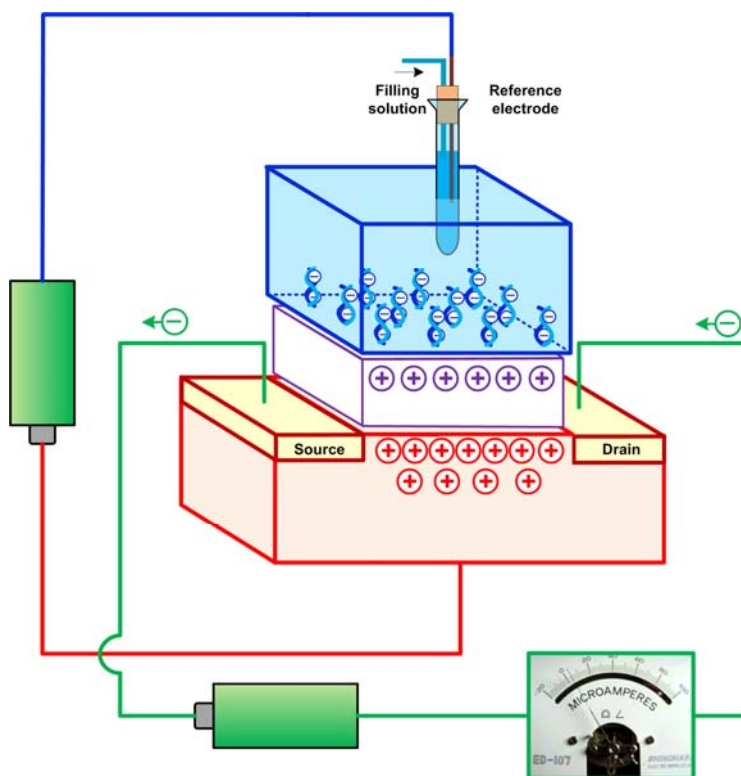


Figure 1.10 Simplified structure of a DNA BioFET, shown with the bias applied

Field-effect DNA sensors (sometimes called BioFET), have been attracting much attention in research, fabrication methods, and operation. One of the main advantages of a BioFET is its low cost: being derived from one of the cheapest contemporary

technologies, which is CMOS integrated circuit technology, the BioFET is guaranteed to be fabricated at extremely low cost, using a few post-processing steps of standard CMOS processes. This also allows all signal transduction and processing circuits to be fabricated on the same chip, alleviating the need for chip-level assembly. The low-power operation of CMOS devices, and by extension the BioFET, allows for the DNA biosensor chip to be deployed on portable devices. Equipped with proper wireless communication circuits, this chip could be part of a wireless biosensor network system for continuous environmental monitoring. Such portable biosensors have been identified as a highly sought technology by the Environmental Protection Agency (EPA) [68]. Furthermore, CMOS processes are very highly reliable, owing to decades of improvement in the fabrication process. This gives the BioFET an edge over the more sensitive emerging technologies such as silicon nanowire and carbon nanotubes.

1.3 The Need for Mathematical Modeling

Biosensor technology is one of the newer research areas that have only gained considerable momentum in the past two decades. Part of this is due to the demands and the success of the human genome project in year 2003, which pushed for proper design and characterization of DNA microarrays. This resulted in a big spike in the amount of work that targeted biomolecular structures and functions, and the appearance of the Worldwide Protein Data Bank. Another reason is the deeper understanding of the mechanics of diseases such as cancers, their evolutionary tendencies, and their microscopic structure and function. The scientific community is better equipped with tools that allows drug synthesis and delivery in a much more efficient and targeted manner. This, in turn, causes many new methods of targeting diseases to be proposed. Laboratories and medical centers thrive on such opportunities, and in turn, require better and faster technologies of isolating, identifying, and synthesizing molecules. Biosensor technology is ideal for such requirements.

Whatever the reason, it is fortunate for research on biosensors to occur at a time when computational resources are available at low cost. The power of computation has

been following closely, and in some cases superseding, Moore’s law, which predicts a doubling of the transistor count in commercial processors every two years (Figure 1.11) [69] . No known technology has been able to evolve at such speed and become available at such a low cost. The computation requirements for biosensors can be very large, and are therefore only feasible under the abundance of high computation power. On the other hand, laboratory experiments remain extremely expensive, with reagents and chemicals costing thousands of dollars. A biosensor will have to be designed and tested many times before its reliability can be assured. The time and cost for such a task is great, and the design must be done by very skilled personnel. Therefore, proper physical modeling and computer simulations can help identify the main characteristics, strengths, and weaknesses of a biosensor implementation with no need for any expensive resources, other than computational time.

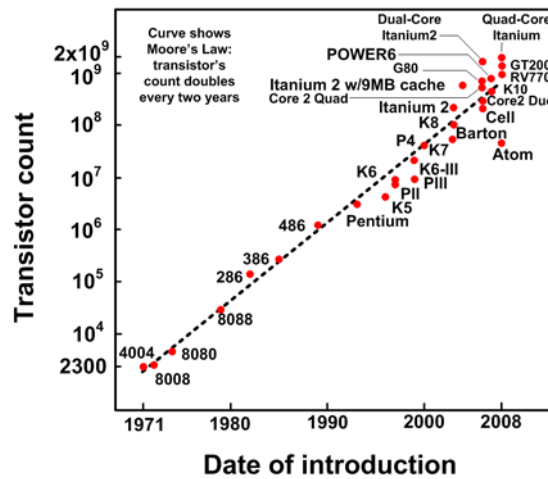


Figure 1.11 Number of transistors (reflecting computational power) for common commercial processors, with the dashed line showing Moore’s law trend [69].

The following sections illustrate the main advantages of using mathematical models and simulations in designing and characterizing biosensors:

1.3.1 Explaining Experimental Observations

Most experiments conducted on biosensors are concerned with direct measures of sensitivity, and demonstrations of selectivity, without direct attribution of the sensor’s

output to a physical process. Often, the output is fitted to an empirical or semi-empirical model, and some conclusions are derived. This abstracts away much of the physics that could otherwise give hints on how to build more reliable sensors. The variables of an experiment are huge, and it is financially prohibitive to try and exhaust all experimental combinations and come up with a complete set of data points. It is, however, very important to know what mechanisms cause the biosensor to operate. In the case of DNA biosensors, many mechanisms have been proposed for the sensitivity, including ionic reorganization at the surface, direct field-effect from the DNA backbone charge, and the change in the dielectric constant of the DNA membrane due to hybridization [70]. There are several valid justifications to each one of these mechanisms. However, even if they are all contributors, it is difficult to state which of these mechanisms has the dominant effect without proper computational analysis and simulations. Knowing the dominant mechanism can help resolve the conflicts and large discrepancies reported in measurements [70]. There are several parameters, including sensor's geometry, material type, temperature, electronic properties, fabrication procedure, and tolerances that could severely alter the response of the biosensor. Modeling and simulations can shed light into which of these parameters play the most critical role in the performance.

1.3.2 Optimizing the Design and Operation of the Biosensor

With science based models and computer simulations, it is possible to examine the performance of the sensor under several operating conditions. For example: The sensor can be simulated for different device sizes, different molecular binding scenarios can be simulated for different host solutions, several biasing and current readout scenarios can be investigated, and many others. Optimization techniques can be used in the given model to predict local maxima of sensitivity and the corresponding design/operation parameters. We could also make good predictions about the expected variation in the received signal due to uncontrollable fluctuations in several parameters. We have used simulations previously to predict that the biasing point for the BioFET to achieve the optimum Signal-to-Noise Ratio (SNR) was in the subthreshold region [71], [72], and

this has been shown to hold true in the case of silicon nanowire DNA sensors [73] . Simulation outputs like these can give guidelines on proper design and operation of DNA biosensors, and can save an experimentalist several attempts in building a suitable device.

1.3.3 Investigating Novel Phenomena

Sometimes, a computer simulation can give results that might seem counter-intuitive at first. However, upon closer inspection, it turns out that these results were logical but overlooked. In our simulations, we have encountered such cases a few times (details in Chapters 3,4, and 5). Just as many scientific discoveries were made by mistakes in the lab, the same thing can be said of computer calculations. The anomalies could sometimes be traced back to an implementation error or non-accounted for physical or chemical process. However, in some cases, they can be characteristics of the device that could lead to better designs.

1.3.4 Handling Complex Geometries

The geometries of biomolecules are often very complex, and the description of their interactions is even more complex, requiring simultaneous solution of many coupled nonlinear equations. The need to capture details at small scales and fine geometries, as well as the complexity of the equations and models, yields a problem that is impervious to analytical, simplified treatments. Coupling of many physical phenomena in different domains requires a complete numerical treatment that is versatile enough to capture all the physics in one single framework. This is especially the case for the BioFET. The physics that describes the signal transduction consists of several nonlinear differential equations that span different regions in the geometry. The size of the DNA molecule is very small in comparison with the size of the biosensor, yet both large and small levels of detail are required for a complete simulation. This problem is not amenable to analytical treatments without very rough, and sometimes partially valid, simplifications. Numerical calculations are, therefore, our best option to capture the operation of the entire biosensor

with a high degree of accuracy, and using the most detailed physics on the most detailed geometries.

1.3.5 Integration with Existing Numerical Packages

As the technology of label-free DNA biosensor mature, there will be a need to integrate it with circuit analysis software. Although the two domains of simulation are quite different (compact modeling for circuit analysis software vs. physical modeling for DNA sensors), they can nevertheless be integrated by proper middleware design. We have previously derived a compact model for a one-dimensional DNA BioFET [74] . However, newer circuit simulation packages push harder for more physics-based modeling, as compact models are not accurate enough to model deep sub-micron devices. Successful integration of physical BioFET models with circuit simulation packages can allow the simulation of circuit ideas that can provide better experimental environments. An example of this would be an electronic temperature regulator of the BioFET. A simulation would include an electronic temperature sensor and heater, coupled to a physical model of the BioFET that includes heat transfer effects. Such a complete simulation could allow for the investigation of several interesting phenomena, such as the effect of temperature gradients on the performance of the biosensor. Equally useful would be the coupling of the chemistry/physics of the BioFET with **Computational Fluid Dynamics (CFD)** packages. One could then see the effect of phenomena such as convective mixing, or electroosmotic and electrophoretic effects, on the BioFET.

Although the merits of complete physical simulation are numerous, it should be mentioned that the validity of the mathematical models and the geometries used should be well-established. Lack of computation resources and/or proper software can force severe simplifications on the model, and limit its usefulness. Nevertheless, simplified models can still give good hints at performance characteristics and limitations of the biosensor, but not the complete picture.

1.4 Main Contributions of this Thesis

This thesis aims to apply numerical physical modeling to static and dynamic aspects of the DNA BioFET. The work in this thesis has resulted in many important observations about the BioFET which, to our knowledge, has not been reported previously. Many of our results apply to the newer nanowire DNA sensors that have been recently reported as well:

1. A first, complete model of the DNA BioFET, with all terminals included and the nonlinearities in the solution and in the semiconductor fully coupled. This model was implemented in both 2D and 3D. The results are compared with the previous 1D simulation, and it is established that higher dimensional modeling is essential for proper characterization of the BioFET.
2. Although commonly believed that the saturation mode of operation is preferable for the BioFET, due to the high transconductance, we show that saturation desensitizes a portion of the channel to hybridized DNA, which can have an adverse effect. This is particularly true for short-channel devices and nanowires.
3. Our investigation into the conformation of single-stranded DNA probes, by means of simulation, show that the conformation change of DNA upon hybridization, from a flailing molecule to a stiff, compact rod, is the main mode of sensitivity in the BioFET.
4. We have developed the first impedance model, from physical principles, for the BioFET. Our model predicts the change in the frequency response due to hybridization of the DNA. Once again, it is established that subthreshold operation is the optimum biasing condition for maximum impedance sensitivity.
5. We investigate the effect of varying the locations of immobilized probes onto the surface of the BioFET on its sensitivity. We establish that for low-density, high speed microarray cells, the locations of the DNA probes are crucial to the sensitivity, with the maximum sensitivity found at uniform coverage. We calculate estimates for the variance in the signal of microarray cells based on this model.

Our collective work on DNA biosensors has resulted in several journal publications. These are listed below:

1. **M. W. Shinwari**, M. F. Shinwari, M. J. Deen, and P. R. Selvaganapathy, “The Effect of DNA Probe Distribution on the Reliability of Label-Free Biosensors,” *Sensors and Actuators B: Chemical* (In press, 2011).
2. **M. W. Shinwari**, and M. J. Deen, “Impedance Modelling of FET-based Biosensors,” *Journal of the Electrochemical Society*, Vol. 198, No. 6, pp. J189-J194, 2011.
3. **Feature Article: M. W. Shinwari**, M. J. Deen, E. B. Starikov, and G. Cuniberti, “Electrical Conductance in Biological Molecules,” *Advanced Functional Materials*, Vol. 20, pp.1865-1883, 2010.
4. **Review Paper: M. W. Shinwari**, D. Zhitomirsky, I. A. Deen, P. R. Selvaganapathy, M. J. Deen, and D. Landheer, “Microfabricated Reference Electrodes and their Biosensing Applications,” *Sensors*, Vol. 10, pp. 1679-1715, 2010.
5. **M. W. Shinwari**, M. J. Deen, and P. R. Selvaganapathy, “Finite-Element Modelling of Biotransistors,” *Nanoscale Research Letters*, Vol. 5, pp. 494-500, 2010.
6. **Invited Paper: M. W. Shinwari**, M. J. Deen, and P. R. Selvaganapathy, “Analytic Modelling of Biotransistors,” *IET Circuits, Devices, and Systems*, Vol. 2, pp. 158-165, 2008.
7. **Invited Paper: M. W. Shinwari**, M. J. Deen, and D. Landheer, “Study of the Electrolyte-Insulator-Semiconductor Field-Effect Transistor (EISFET) with Applications in Biosensor Design,” *Microelectronics Reliability*, Vol. 47, pp. 2025-2057, 2007.
8. D. Landheer, W. R. McKinnon, G. Aers, Weihong Jiang, M. J. Deen, and **M. W. Shinwari**, “Calculation of the Response of Field-Effect Transistors to Charged biological Molecules,” *IEEE Sensors Journal*, Vol. 7, pp. 1233-1242, 2007.

9. M. J. Deen, **M. W. Shinwari**, J. C. Ranuárez, and D. Landheer, “Noise Considerations in Field-Effect Biosensors,” *Journal of Applied Physics*, 100, 074703, 2006.

Additionally, the following conference presentations were also results of this work:

1. **M. W. Shinwari**, M. J. Deen, and P.R. Selvaganapathy, “Geometric and Conformational Considerations in Biotransistors,” *217th Electrochemical Society Conference*, Vancouver, 2010.
2. **Invited Keynote Paper:** M. J. Deen, **M.W. Shinwari** and R. Selvaganapathy, Towards Low-cost, High-sensitivity, Integrated Biosensors, *26th IEEE Int. Conf. on Microelectronics (MIEL 2008)*, Nis, Serbia, Electron Devices Society, IEEE Press, Piscataway, NJ, pp. 307-314 (11-14 May 2008).
3. **M. W. Shinwari** and M. J. Deen, “Optimization of DNA Detection Using FETs,” *1st Microsystems and Nanoelectronics Research Conference*, Ottawa, 2008.
4. M. J. Deen, **M. W. Shinwari**, and D. Landheer, “Noise Characteristics in Integrated Biosensing Devices,” *Proceedings of the 19th International Conference on Noise and Fluctuations*, Vol. 922, pp. 399-404, 2007.
5. **Invited Paper:** M. J. Deen, and **M. W. Shinwari**, “Modeling the Electrical Characteristics of FET-Type Sensors for Biomedical Applications,” *NSTI Nanotech Workshop on Compact Modeling*, Santa Clara, 2007.
6. **Keynote Paper:** M. J. Deen, **M.W. Shinwari**, D. Landheer, G. Lopinski, “High Sensitivity Detection of Biological Species via the Field-Effect,” *Proceedings of the 6th International Caribbean Conference on Devices, Circuits, and Systems*, Playa del Carmen, 2006.

Finally, we have co-authored the following chapter, which goes into deeper details of the practical aspects of this research:

1. D. Landheer, W. R. McKinnon, W. H. Jiang, G. Lopinski, G. Dubey, N. G. Tarr, **M. W. Shinwari**, and M. J. Deen, “Bioaffinity Sensors Based on MOS Field-Effect Transistors,” *In Semiconductor Device-Based sensors for Gas, Chemical, and Biomedical Applications*. Boca Raton: CRC Press, 2011.

1.5 Organization of this Thesis

- Chapter 2 introduces the methods generally used for simulating DNA and DNA sensors, with focus on our method of choice: the Finite-Element Method.
- Chapter 3 gives details about the model used for the biosensor development, both in 2D and in 3D. The geometry is defined, and the equations are given. Simulation results are compared to our earlier 1D simulation, and several observations on the sensitivity of the BioFET are given based on the results.
- Chapter 4 explains our impedance model for the BioFET. The derivation of the equations is given, followed by the results of the calculations. Electrochemical Impedance Spectroscopy (EIS) diagrams for the BioFET are produced, and several conclusions and observations are made.
- Chapter 5 introduces the application of a hybrid Monte-Carlo/Finite Element Analysis to the BioFET. This is used to address the conformation problem of single-stranded DNA. Then, the same method is used to calculate the variations in the BioFET due to random placements of DNA probes on the surface. The geometries of the problem are described, followed by the mathematical model and results.
- Chapter 6 concludes the thesis, and gives prospective problems for future research.

Chapter 2

MATHEMATICAL MODELING STRATEGIES

2.1 Introduction

Mathematical modeling of DNA biosensors can be a daunting task, since the system under consideration is quite dynamic and complex. Additionally, there are many potential levels of abstraction in the mathematical description of the system, which lead to different paradigms in designing the simulation software. Capturing of all the physics of the DNA molecules and coupling them to the physics of the underlying semiconductor, especially for large area biosensors, requires such a huge computational effort that makes it inaccessible to today's most resourceful computers. For this reason, scientists often resort to several simplifications to the geometry, equations, and boundaries to obtain simpler solutions that, nevertheless, capture the essential physics that is intended to be studied.

This chapter gives an introduction to the different levels of physics that surround the BioFET, which include the description of the DNA molecules, the surrounding aqueous medium, and the underlying semiconductor. Several mathematical models for dealing with these complex physics modes, and that are frequently used in the literature, will be briefly introduced. After that, our chosen simulation method, the finite-element method, will be explained in detail. This chapter will conclude with an overview of an emerging "hybrid" solution paradigm that is ideal for the field of biosensors.

2.2 Physics Required for Characterizing the BioFET

A mathematical description of the BioFET requires two seemingly incompatible models: those of the highly dynamic, chemistry driven interactions of the DNA molecule, the surrounding electrolyte, and the immobilization surface, and those of the more rigid regions of the sensor, like the insulator and the semiconductor region. The former is very common to computational chemists and physicists, whereas the latter is more pronounced in engineering and material science. This heterogeneous nature of DNA biosensors makes it very hard to come up with an accurate model that captures all of the physics. Nevertheless, several approximations can be made, based on the phenomenon that is to be focused on. The following sections give an overview of the different modeling levels required for different areas of the BioFET.

2.2.1 The DNA Molecule

The DNA molecule in itself is by far the hardest part to model. This is due to the complex nature of its geometry, in addition to the molecule's flexibility and its versatile chemistry. A diagram of the DNA molecule is shown in Figure 2.1 [75], where it is shown that the DNA molecule is a polyelectrolyte comprised of two helically-wound sugar-phosphate backbones, joined in the middle by nucleobases (Adenine, Thymine, Cytosine and Guanine). The two strands are joined by means of hydrogen bonds between matching nucleobases (AT and CG), as well as with dispersion forces that occur between the stacked flat nucleobases [4]. The phosphate groups are negatively charged in biologically relevant conditions (25°C, 1mM-1M monovalent salt concentration, pH 7). It is believed that these negative charges are either directly or indirectly responsible for the signal change in a BioFET due to DNA capture.

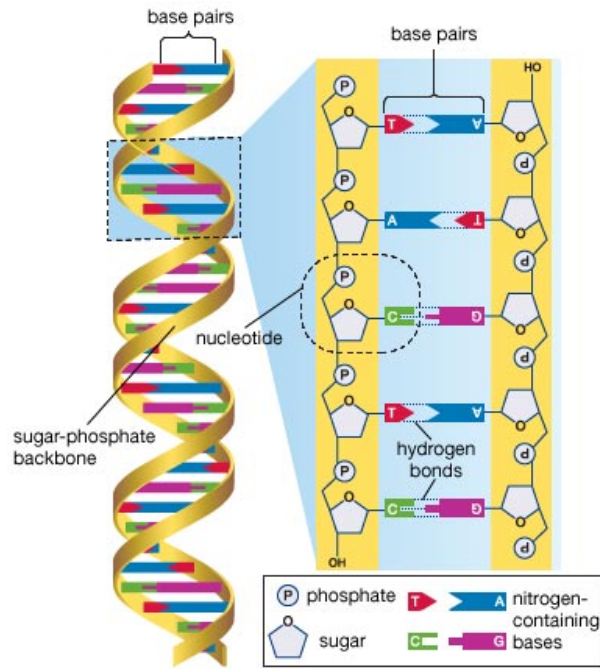


Figure 2.1 Structure of the DNA molecule [75]

In a BioFET, the DNA molecules used as probes are short (typically 20-30 bases long). Shorter probes (oligonucleotides) allow faster and more specific hybridization rate. However, their descriptions can vary widely from models used to describe longer chains. Two problems are associated with the description of the DNA molecule: the conformation and motion dynamics, and the electrostatics/chemistry. The motion of longer DNA molecules is generally handled by simplified continuous models, such as the worm-like chain (WLC) model [76] or the free-jointed chain model (FJC) [77]. Shorter DNA strands are stiffer and cannot be modeled by such continuous models, but are rather treated using complete molecular dynamics studies [78]. Unfortunately, for such studies, simulations on the most powerful computers are limited to a few nanoseconds, limiting the observation of longer timescale effects. The DNA conformation and flexibility will be revisited in Chapter 5.

The molecular electrostatics and chemistry of the DNA molecule are very important in dictating the interaction of the DNA with its surroundings. On the deepest

level, the charge distribution of a DNA molecule is determined by solving the many-body Schrödinger equation:

$$\left(-\hbar^2 \sum_i (2m_i)^{-1} \nabla_{\vec{r}_i}^2 + \sum_j V(\vec{r}_i, \vec{r}_j) \right) \psi(\vec{r}_1, \vec{r}_2, \dots) = i \hbar \frac{\partial}{\partial t} \psi(\vec{r}_1, \vec{r}_2, \dots). \quad (2.1)$$

In Equation (2.1), \vec{r}_n is the position vector for the n -th body, ψ is the wavefunction amplitude, m_i is the effective mass of the i -th object, V is the potential energy between two objects, and \hbar is the reduced Planck constant. The summations in Equation (2.1) go over all nuclei and electrons of the molecule. The eigenvalue time-independent version of Equation (2.1) gives the many-body wave function which describes the shape of the molecule. Unfortunately, Equation (2.1) is too complicated to solve for even the simplest two-body system, and many approximations are therefore used to make the solution more tractable. The Born-Oppenheimer approximation allows decoupling of nuclei and treating them as classical particles. The problem then reduces to finding the energy and shape of the electronic cloud as a function of the nucleic coordinates. Since all nucleic conformations cannot be exhausted, especially not for a polyelectrolyte like the DNA, the approximate locations of the nuclei have to be determined from other, classical molecular dynamics simulations, or by resorting to X-ray crystallography data.

Even with all of these approximations, the many-body electronic wave function has to be decoupled. A typical approximation is to replace the dependency of the electronic mutual potential energies by an effective average potential [79]. This is called the **Hartree-Fock (HF)** approximation. The equation then reduces to a single-particle wave equation that must be solved self-consistently, since the average potential will be a function of the wavefunction. For this reason, the method is named the **Self-Consistent-Field (SCF)** method as well. Application of this method results in a coupled system of partial differential equations. The solution wavefunctions then give the spatial extension of the electronic cloud and its density. Figure 2.2 shows an example of such density map for a pair of bases on the DNA molecule [80]. Another commonly used method is the **Density Functional Theory (DFT)**, which transforms the wave equation into a differential equation in electronic density (called Kohn-Sham equations). Regardless of the method,

averaged correcting potential terms must be introduced to account for electronic correlation effects. The DFT method was used in calculating the energy of pairing of different bases in DNA [81] , as well as the interaction with synthetic Peptide Nucleic Acids (PNA) [82] .

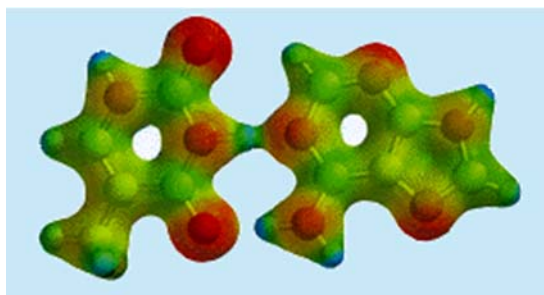


Figure 2.2 Electron density map for a DNA base pair (Adenine-Thymine) [80]

Ab-initio techniques of solving the electronic structure of the DNA can help in determining the effective dipole moment of the molecule, or to give fine details about its chemical affinities or charge distribution. However, they remain time and computation intensive. Furthermore, in large macromolecules, it is generally the case that the wave equation is effectively decoupled over far regions in the molecule, i.e. orbitals that retain their atomic extension and do not morph into molecular bonding orbitals. For example, the Hamiltonian of the entire molecule can be thought of as consisting of a Hamiltonian of the backbone alone, in addition to another Hamiltonian of the bases. This, of course, is an approximation. The key here is to find the proper problem simplification without sacrificing the loss of valuable chemical and electrical information about the molecule. For example, a Hamiltonian-splitting technique which couples the electronic states in the bases of the DNA to those in the backbone, sometimes called a fishbone Hamiltonian, was used to model electronic transport between Guanine states in a DNA molecule [83] . Ab-initio techniques are generally the most time-consuming, but give the most accurate electronic structure and energy information. They can, therefore, be used to estimate the energy of particular reactions by calculating the difference in the electrostatic energy before and after the reaction takes place. Coupled with molecular dynamics, quantum

simulation can also be used to estimate the dielectric constant of a macromolecule, by statistically averaging calculated dipole moments [84] .

Ab-initio techniques are often solved for small portions of the DNA molecule under ideal conditions, and without explicit consideration of the solvent molecules or the counter-ions. This is done to allow convergence within reasonable time and avoid seemingly needless complexity. However, when trying to simulate dynamic processes such as DNA hybridization, or quantify the chemical properties of the DNA, quantum simulations become out of reach for such complex systems. Molecular dynamics simulations can be used to predict some physicochemical properties of the molecule. Due to the high complexity of the DNA, coarse-grained models can be used to approximate the electrical and chemical interactions. An example of this was carried out in [85] , where the bases of the DNA were modeled as rigid ellipsoids, shown in Figure 2.3. The interaction potentials (electrostatic, Van der Waals, dispersion, bonding interactions) will have to be empirically introduced, based on best-fitting to experiments or ab-initio models. These models are generally derived for point-shaped atomic interactions. They would have to be modified for coarse-grained models, such as that in [85] . Another example for functional coarse-graining is the MARTINI force field method [86] , which replaces groups of molecules by equivalent force fields. This method was used to characterize bi-lipid layer formation (as in the exterior of cells). Coarse-graining could also be used to simplify the treatment of solvent and ionic species. Such simplifications allow the simulations to run for significantly longer times, which enable the capture of long-time phenomena such as DNA hybridization and coiling [87] .

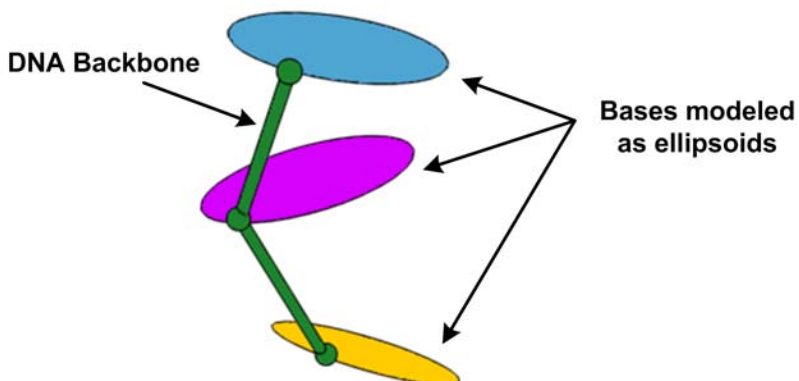


Figure 2.3 Coarse-grained model of DNA for molecular dynamics calculations [85]

2.2.2 The Electrolyte

In all DNA biosensor experiments, the biochemical hybridization reaction occurs in an electrolytic aqueous medium. The biological recognition will only proceed under specific conditions of ionic strength, solution's pH, and temperature. It is imperative, therefore, to include a mathematical description for the electrolyte when modeling the response of the BioFET. The concentration of the electrolyte can severely inhibit the sensitivity of the BioFET, due to counter-ion condensation[4] , [25] . Moreover, the aqueous environment is significantly distorted in the vicinity of polyelectrolytes, which then modulates its dielectric constant. In label-free biosensors, this is expected to affect the sensitivity.

The most important phenomena to include when treating the electrolyte are the following:

1. The response of water molecules, as well as ions, to electric fields.
2. The chemical association of water and ions to surfaces, as well as to the DNA molecule.
3. The electrophoretic mobility of ions in an electric field.
4. The equilibrium reaction kinetics for the buffering agent.
5. Other effects, such as solvation energies and steric hindrance.

When molecular dynamics simulations are used with explicit solvent and counter-ion models, the empirical interaction energies will suffice to capture all of these phenomena.

However, such simulations require large computational power and are generally only implemented for a few picoseconds to a few nanoseconds. Such time scales are not compatible with the slower electrical and mechanical time scales when dealing with fluid flow or electrophoretic or electroosmotic transport. Additionally, at room temperature, the motion of ions is very rapid, and only the statistical average distribution is of significance. Statistically averaged mean-field theories are most appropriate for treating the solvent in such case. A basic result from equilibrium statistical mechanics is that the configuration of an ensemble of particles for a given total system energy at equilibrium can be given as a probability distribution of the respective particle energies. Thus, the probability of a particle being at a state n_i , which has energy E_i , is given by:

$$P[n_i] = \frac{e^{-\frac{E_i}{kT}}}{\sum_j e^{-\frac{E_j}{kT}}}, \quad (2.2)$$

where kT is the thermal energy with k being Boltzmann's constant, and T the absolute temperature. The summation extends over all microstates of the particle. The summation in the denominator is called the partition function "Z", and the corresponding distribution is known as the discrete Maxwell-Boltzmann distribution. The state n_i is a general term encompassing position, momentum, and internal conformation/chemical association of the particle. For example, a solvated ion is at a lower energy than that of an ion which is free of its solvation shell, even though both ions might have the same position and momentum. If thermal equilibrium is assumed, and no alteration of chemical composition is undergone by the particles, then Equation (2.2) can result in the following formula for the volumetric density of the species c as a function of the bulk concentration c_0 and the energy E at position \vec{r} :

$$c(\vec{r}) = c_0 e^{-\frac{E(\vec{r})}{kT}}. \quad (2.3)$$

Equation (2.3) is the Boltzmann equation that is often used in mean-field analysis of species in a solution. The energy term encompasses the electrical and chemical energy changes, and is often written as the electrochemical potential energy $\tilde{\mu}$:

$$E = \tilde{\mu} = \mu + zqV \quad , \quad (2.4)$$

where μ is the chemical potential of the species under consideration, z is its electrical valence, and V is the electrostatic potential at a particular point in space. The convention for using Equation (2.4) in (2.3) is that the chemical potential and electrostatic potential are both assumed to be zero in the bulk of the material (where there is no electric field). Therefore, care must be taken when using Equations (2.3) and (2.4) across heterogeneous phases. A basic condition for equilibrium in statistical thermodynamics is that the gradient of the electrochemical potential has to be zero for every reacting species:

$$\nabla \tilde{\mu} = 0 \quad . \quad (2.5)$$

Figure 2.4 illustrates the difference between the chemical and electrical potentials for a solvated ion. The electrical potential on the ion results from the ion being in the presence of a net electric field that is caused by the aggregation of other ions (possibly due to an externally applied electric field). On the other hand, the chemical potential consists of the potential energy due to surrounding the ion with solvent molecules, in addition to all other forces of interaction (electrostatic, chemical bonds, and others) between the ion and all the surrounding ions. There is some ambiguity in distinguishing the chemical and electrical components of the total potential energy, since the chemical potential also arises from interactions that can eventually be traced to electrostatic energies. In electrochemistry, as long as the non-electrostatic attractions remain intact (i.e. all chemical bonds, dispersion forces, and solvation shells), then the chemical potential can only change with the change in the interaction of the ion with other ions of the same species. The chemical potential is therefore a function of the aggregation (volumetric density) of the species. For infinitesimally small species that could be treated as an ideal gas, or for a very dilute solution, Equation (2.3) can be used to show that the change in the chemical potential is related to the change in volumetric concentration of the species by the following expression:

$$\tilde{\mu}_2 = \tilde{\mu}_1 - kT \ln\left(\frac{c_2}{c_1}\right). \quad (2.6)$$

When the concentration of the ions is high, one cannot neglect their occupied volume or their solvation shell. In such cases, the concentration ratio is often replaced by an empirical quantity called the activity a , defined in the following equation:

$$\tilde{\mu}_2 = \tilde{\mu}_1 - kT \ln(a). \quad (2.7)$$

The activity is linearly related to the ratio of concentrations in Equation (2.6), and the linear constant is called the activity coefficient. Knowledge of the activity will keep Equation (2.7) valid over higher electrolyte concentrations. However, when the solution is close to saturation, the activity coefficient becomes a function of the concentration. This nonlinearity results due to several ion-ion interactions (e.g. the formation of ion pairs), solvation shell sharing, steric hindrance to aggregation, and ion-solvent interaction (i.e. fewer number of free water molecules) [88]. Rigorous analysis of ion-solvent and ion-ion effects would require complete molecular dynamics simulations. However, several mean-field models have been proposed to address at least some of these nonidealities, such as steric effects [89] -[91].

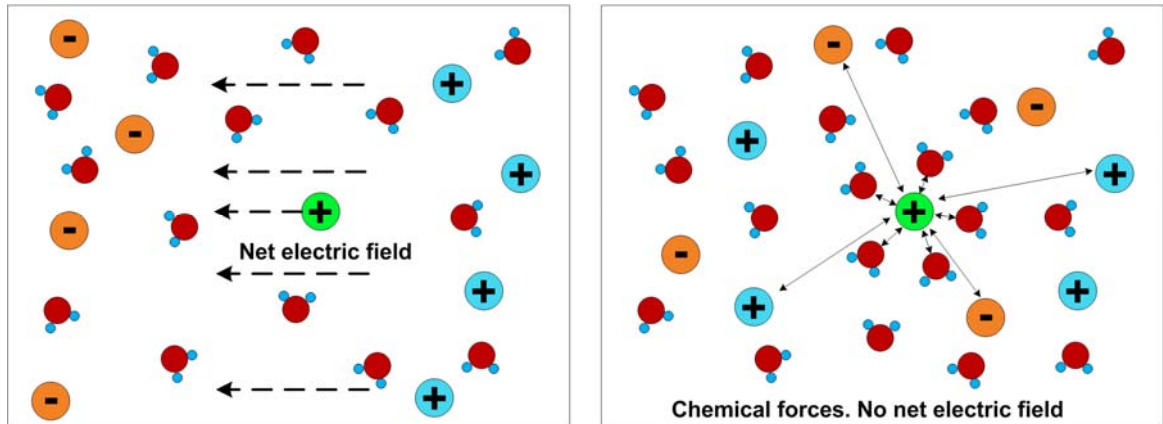


Figure 2.4 Electrical potential (left) occurs due to the presence of a net electric field due to the organization of ions. Chemical potential (right) is the reduction of the ion's energy due to surrounding by other ions and molecules, and the presence of chemical bonding and nonbonding forces between them.

Another technique of capturing the non-ideal equilibrium effects of ions and electrolytes is to try and deduce models from thermodynamic data, rather than from microscopic information. An example is the estimation of the solubility and activity coefficients of ions and polyelectrolytes (such as DNA) using osmotic pressure. Osmotic pressure is defined as the hydrodynamic pressure that needs to be applied to a solution to prevent an influx of water molecules across a semi-permeable membrane. Figure 2.5 illustrates this concept. For two water reservoirs at the same temperature and pressure, no net water molecules are expected to flow from either side to the other. When a high enough concentration of electrolytes is dissolved, they trap a portion of the water, reducing the bulk water concentration in this reservoir. The semi-permeable membrane prevents migration of the ions, but allows water molecules to flow so that the balance of the water chemical potential is restored. Thus, the osmotic pressure is useful in determining the rate of solubility of an ion, and subsequently its activity coefficient. This osmotic pressure test can be used to extract the virial coefficients (v_i) of a solute in water, which provide detailed characterization of the non-ideal equation of state. This is given by the virial expansion [88] :

$$\frac{P}{kT} = n + v_2(T)n^2 + v_3(T)n^3 + \dots \quad (2.8)$$

The virial coefficients $v_2(T)$ and $v_3(T)$ relate the osmotic pressure P to the volumetric concentration n and are generally functions of the temperature. From the virial coefficients, it is possible to calculate the activity coefficients using Pitzer's theorem [92] . This and similar purely thermodynamic treatments are used extensively in the literature, and have even been used to provide simple models for water [93] .

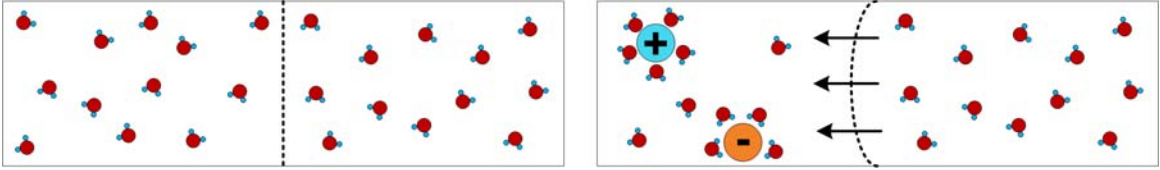


Figure 2.5 Illustration of osmotic pressure. Before any ions are dissolved, no net water molecules move across the semi-permeable membrane (left). As ions are dissolved, they trap a portion of the water molecules, which lowers the chemical potential of free water molecules, causing an influx of water through the membrane.

In addition to the thermodynamic and energetic treatments of the electrolyte, kinetic treatments are needed for describing nonequilibrium processes. For example, motion of the electrolyte under a uniform electric field or a temperature or pressure gradient. In this case, the behavior of the molecules of the solvent, as well as the solute, significantly differs from that at equilibrium. Once again, classical and quantum molecular dynamics simulations provide the highest degree of accuracy and have the potential to capture all of the physical processes that give rise to macroscopic observables. Indeed, there has been a lot of work on simulating fluid flow using molecular dynamics [94] ,[95] . However, given the computational cost required, scientists often resort to simpler, mean-field theories to describe the kinetics of the nonequilibrium process. Macroscopically, all molecules (whether those of the solvent or the solute) will move under the influence of a chemical potential gradient, an applied force, or by means of interaction with other species that are moving. These three methods give rise to the transport methods of diffusion, drift, and convection, respectively. In its simplest formulation, the diffusive flux (\vec{J}) of a species is given by Fick's law:

$$\vec{J} = -K_{\mu} \nabla \mu, \quad (2.9)$$

where K_{μ} is the conductivity coefficient which, in general, can be a function of the chemical potential μ . In absence of chemical interactions or alterations of the diffused species, and in the limit of ideal solutions, Fick's law relates the flux to the volumetric concentration c of a species:

$$\vec{J} = -D\nabla c, \quad (2.10)$$

where D is the diffusion coefficient. In general, the diffusion coefficient is not constant, but varies in a complicated way with the chemical potential of the species. Fick's law is, therefore, a linearized approximation of a more complicated flow. In fact, similar phenomena in physics have analogous formulation to Fick's law, and have their own range of validity. Table 2.1 summarizes such phenomena. When the diffusion coefficient's nonlinearity is important, the diffusion is called non-Fickian.

Table 2.1 Physical phenomena showing Fickian behavior

<i>Phenomenon</i>	<i>Law</i>	<i>Formula</i>
Heat conduction	Fourier's Law	$\vec{q} = -\lambda\nabla T$
Electrical conductance	Ohm's Law	$\vec{J} = -\sigma\nabla V$
Porous fluid flow	Darcy's Law	$\vec{q} = -K\nabla P$
Photon diffusion	Photon Diffusion Equation	$\vec{f} = -D\nabla\phi$

\vec{q} : Thermal flux (Fourier's Law), fluid flux (Darcy's Law), \vec{J} : Electrical current density, \vec{f} : photon flux, λ : thermal conductivity, σ : electrical conductivity, K : Darcy's coefficient (permeability/viscosity), D : photon diffusion constant

Drift motion of ions characterizes the steady-state interaction of species with external forces, such as gravity or electromagnetic fields. Whereas Newton's laws of motion are still valid, retarding viscous forces often result in species rapidly acquiring a terminal constant velocity. The mobility model relates the flux \vec{J} due to this terminal velocity to the applied force. In case of an electrical force field \vec{E} , the mobility μ_c relates the flux to the electric field by:

$$\vec{J} = c\mu_c\vec{E}, \quad (2.11)$$

where c is the species volumetric density. For smaller ions, the mobility results from the viscous forces of interaction between the solvated ion and the surrounding solution. For larger polyelectrolytes and uncharged particles, the mobility results from the surrounding cloud of equalizing counter-ions, their interaction with the polyelectrolyte, and their interaction with the bulk of the solution. In this case, the mobility of the species depends on its zeta-potential, in what is called Smoluchowski's equation:

$$\mu_c = \frac{k \varepsilon_0 \varepsilon_r \zeta}{\eta}, \quad (2.12)$$

where ζ is the zeta potential of the macromolecule, η is the viscosity, and k is a constant that depends on the shape of the molecule and the thickness of the counter-ion shell surrounding the macromolecule.

Ions and polyelectrolytes can be transported by means of convective mixing or pumping as well, in a manner similar to that with which blood transports nutrients. A mean-field theory of fluid flow is given by the Navier-Stokes equations of momentum and mass continuity:

$$\begin{aligned} \rho \left(\frac{\partial \vec{v}}{\partial t} + \vec{v} \cdot \nabla \vec{v} \right) &= \nabla \cdot \mathbf{T} + f \\ \frac{\partial \rho}{\partial t} + \nabla \cdot (\rho \vec{v}) &= 0 \end{aligned}, \quad (2.13)$$

where ρ is the fluid density, \vec{v} is the velocity field, \mathbf{T} is the stress tensor, which includes the applied pressure, and f is the body forces, such as electromagnetic forces. Navier-Stokes equations are nonlinear coupled partial differential equations and are generally extremely hard to solve. Several simpler equations are generally used under limiting conditions. For example, for fluids where viscous forces dominate over inertial forces (low Reynolds number fluids), one could use the simpler Stokes equation. On the other hand, for high Reynolds number fluids, Burger's equation of fluid flow is valid.

2.2.3 The Insulator's Surface

The insulator is the site where the biological recognition occurs, and where most of the interesting chemistry in the BioFET takes place. Ionic species and spurious molecules in the sample electrolyte can condense onto the surface, some of which could severely compromise the operation of the BioFET. The nature of the condensation depends on the phenomenon that causes it. Covalent bonding of ions with dangling bonds can cause surface complexation and the removal of the hydration shell of solvated ions. Additionally, non-covalent adsorption (physisorption) can occur due to long range electrostatic or dispersive forces or hydrophobic aggregation near the surface. Depending

on the ion being adsorbed to the surface, this can have a positive or negative impact on the biosensor. For example, adsorbed ions can inhibit or change the energetics of target capture. On the other hand, efficient adsorption of linker molecules is necessary to ensure high-density immobilization of probe oligonucleotides, and also to prevent cross-adsorption by taking up the insulator's entire surface. Additionally, the chemistry of the probe immobilization must be fully understood. The immobilized probes must have complete freedom to pair up with the target; otherwise the incubation time might be prohibitively long.

Understanding the adsorption process requires intimate familiarity with the thermodynamics and the kinetics of aggregation on a surface. General mean-field models for adsorption treat the adsorbates as point particles. The degree of adsorption is measured as the percentage of coverage of the active adsorption sites on the insulator's surface. Different models predict different "adsorption isotherms" that give the equilibrium coverage of the surface as a function of the temperature, energy of the adsorption, and other geometrical and surface parameters. The simplest isotherm is known as the Langmuir isotherm. For equilibrium coverage θ and free energy of adsorption ΔE , the isotherm is given by [96] :

$$\theta = \frac{ce^{\frac{-\Delta E}{kT}}}{1 + ce^{\frac{-\Delta E}{kT}}}, \quad (2.14)$$

where c is the concentration of the bulk adsorbate in the solution. Langmuir isotherm follows from a first-order reaction where the energy of reaction is constant and independent on the proximity of free sites to occupied ones. In general, the energy of interaction can be a function of the coverage, and the simplest isotherm that captures a linearized dependence of the energy on the coverage is given by the Frumkin isotherm:

$$\theta = \frac{ce^{-\left(\frac{\Delta E}{kT} + \gamma\theta\right)}}{1 + ce^{-\left(\frac{\Delta E}{kT} + \gamma\theta\right)}}, \quad (2.15)$$

where γ is the linear coefficient in the Taylor's expansion of the Energy-coverage relationship, usually determined by experiment. In many cases, the adsorption energy

depends on imperfections on the surface and the adsorption energies can vary. When the adsorption energy has an exponential distribution, and assuming normal Langmuir-type adsorption, then we arrive at Freundlich's isotherm with empirical constants n and A [97] :

$$\theta = A c^n . \quad 2.16$$

The choice of a specific adsorption isotherm depends on the energy and energy distribution of adsorption, whether the adsorption occurs in aqueous or gaseous environment, the possibility of creating multi-layers, the complexity and molecular structure of the adsorbent, and whether the adsorption is a single component or multi-component adsorption process. Typical isotherms include the **Brunauer–Emmer–Teller** (BET) isotherm, Temkin isotherm, and the Gaussian isotherm. Table 2.2 gives a summary of some of the most famous isotherms, and Figure 2.6 shows sample plots of several isotherms, as a function of the bulk concentration.

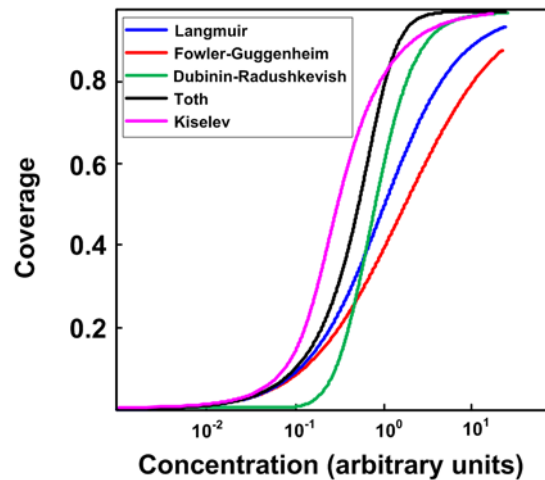


Figure 2.6 Concentration vs. coverage plots of some isotherms

Table 2.2 Several common isotherms and their uses

<i>Isotherm</i>	<i>Uses</i>	<i>Formula</i>	<i>Reference</i>
Generalized Langmuir	Monolayer adsorption with heterogeneous energy surfaces	$\theta = \left(\frac{(Kc)^n}{1 + (Kc)^n} \right)^{m/n}$	[98]
Fowler-Guggenheim	Monolayer adsorption with lateral first-order interactions between adsorbates	$Kc = \frac{\theta}{1 - \theta} e^{\frac{2\alpha\theta}{kT}}$	[99]
Kiselev	Localized monolayer adsorption with associative lateral interaction on homogeneous surface	$Kc = \frac{\theta}{(1 - \theta)(1 + k_n \theta)}$	[99]
Jovanovic	Monolayer adsorption with vertical interactions (surface-bulk)	$\theta = 1 - e^{-Kc}$	[100]
Tóth	Monolayer adsorption with asymmetric Gaussian distribution of adsorption energies	$\theta = \frac{Kc}{\left(1 + (Kc)^n\right)^{1/n}}$	[100]
Misra	Monolayer adsorption with heterogeneous surface	$\theta = 1 - \left(1 + (k - 1)Kc\right)^{1/(k-1)}$	[101]
Dubinin-Radushkevich	Monolayer adsorption with microporous sites	$\theta = e^{-B \left(kT \ln \left(1 + \frac{\alpha}{c} \right) \right)^2}$	[102]
Hill-de-Boer	Mobile monolayer adsorption with lateral interactions	$K_1 c = \frac{\theta}{1 - \theta} e^{\left(\frac{\theta}{1 - \theta} \frac{K_2 \theta}{kT} \right)}$	[103]
BET	Multilayer adsorption (often overestimates thickness. Other theorems exist such as n-layer BET)	$\theta = \frac{1}{1 - c} \left(\frac{Kc / (1 - c)}{1 + (Kc / (1 - c))} \right)$	[104]
Hüttig	Two-layer adsorption	$\theta = (1 + c) \frac{Kc}{1 + Kc}$	[99]
Temkin	Multilayer gas adsorption	$\theta = \frac{kT}{\Delta E} \ln(Kc)$	[105]

A suitable adsorption isotherm is needed on the insulator's surface for many different phenomena. Active adsorption sites on the insulators can be easy traps for ions or protons in the aqueous solution. These ions can contribute to screening the charge of the DNA or otherwise jeopardizing the operation of the BioFET. During the SAM layer deposition, it is necessary to have a fully packed layer and the adsorption of this layer on different surfaces (such as nanowires) must be carefully characterized. Additionally, the immobilization and hybridization of DNA can both be seen as mean-field adsorption processes. It is important to properly characterize these adsorption processes to ensure fast biosensor response, high sensitivity, and high reliability. A good review on the

different techniques of monitoring the adsorption process is given in [106]. What is most interesting is the fact that most SAM adsorption experimental data seemed to fit nicely to a Langmuir model, even though it is known that hydrophobic forces are responsible for keeping the SAM molecules together, and therefore the lateral forces should have an influence on the adsorption thermodynamics and kinetics. It was shown via simulations [107] that longer molecules tend to have higher coverage. This can be explained by the stronger lateral interactions between them. On the other hand, if the longer SAM molecules are not very rigid, then steric hindrance can cause a reduction in the coverage. It is therefore very complicated to arrive at a general theory that characterizes all adsorbed SAM molecules on all surfaces.

As for DNA hybridization, Langmuir's model fails to account for the reported reduction of equilibrium coverage density with the density of probes [60]. An attempt to account for this reduction of sensitivity was given by [108], in which the mutual repulsion between DNA probes was seen as a major influence on the continued hybridization. Accordingly, the isotherm for DNA hybridization was suggested as:

$$c = \frac{\theta}{1-\theta} e^{\frac{\Delta G_0}{kT}} e^{\frac{V_s Z N_p (1+\theta)}{kT}}, \quad (2.17)$$

where c is the adsorbate's volumetric concentration at the surface, ΔG_0 is the hybridization free energy with no lateral forces present, Z is the number of bases in the DNA molecule, N_p is the probe surface density, and V_s is a constant that relates to the salt concentration, the Debye length, and the geometry of the adsorbates [108]. This model was later refined by Halperin, *et al* [109] to include effects such as competitive surface hybridization and competitive bulk hybridization, which are important when the solution can contain more than one target type. Despite the abundance of attempts to characterize the hybridization kinetics, experimental attempts to verify the models seem to be contradictory, with some claiming poor correlations with the models [110], others assuring that simple Langmuir isotherms will suffice [111], and yet another group blames the inconsistency on washing of the microarray cells, which is claimed to cause some

dissociation of targets [112] . Clearly, a model is still lacking for a complete understanding of the hybridization of macromolecules onto surfaces.

2.2.4 The Reference Electrode

Modeling of the reference electrode can include similar arguments to those of the insulator, namely, energetics of adsorption, isotherms, and kinetics. However, for electrodes, the most important reaction is the electron transfer reaction that allows the reference electrode to set the potential of the solution. In electrochemical terms, there are three types of electrodes: ideally polarizable, non-polarizable, and partially polarizable. This classification distinguishes electrode interfaces in terms of their ability to conduct current. A non-polarizable electrode is one which can freely allow electron transfer reactions without any hindrance. This is shown in Figure 2.7 and compared to the other two types. A reference electrode is expected to be non-polarizable; otherwise it could undermine the sensitivity of the biosensor [9] . The reference electrode sets the potential of the solution by achieving electrochemical equilibrium with the solution via electron transfer reactions. These reactions are either oxidation (removing electrons from the solution), or reduction (adding electrons) reactions. Collectively, they are called “redox” reactions.

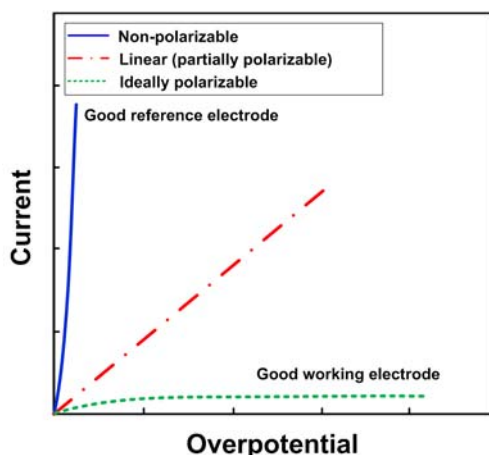


Figure 2.7 Typical current-voltage characteristics of the three electrode types

The kinetics of the redox reactions are important in characterizing the operation of the reference electrode. They allow estimates of the current-voltage characteristics, help determine the time needed to reach equilibrium, and give insight into the effects of contaminants and cross-reactions on the electrode potential. The potential of the electrode-electrolyte interface has to be maintained constant and stable for a long period of time. This is satisfied by ensuring that the kinetics of the redox reactions are very fast, and that the solid-liquid interface is stable. Many redox reactions result in precipitation, gas evolution, or dissolution of the electrode. These processes occur because the ions have to be adsorbed onto the surface of the metal first, followed by electron discharge, which results in formation of a chemical with the surface (precipitation), or in two discharged ions forming a gas molecule (evolution), or ionization of an atom in the electrode (dissolution). On the other hand, some redox reactions occur by electrons directly hopping from the donor to the acceptor via quantum mechanical tunneling, without any intermediate steps. These are known as outer-sphere reactions. Figure 2.8 illustrates these reaction types.

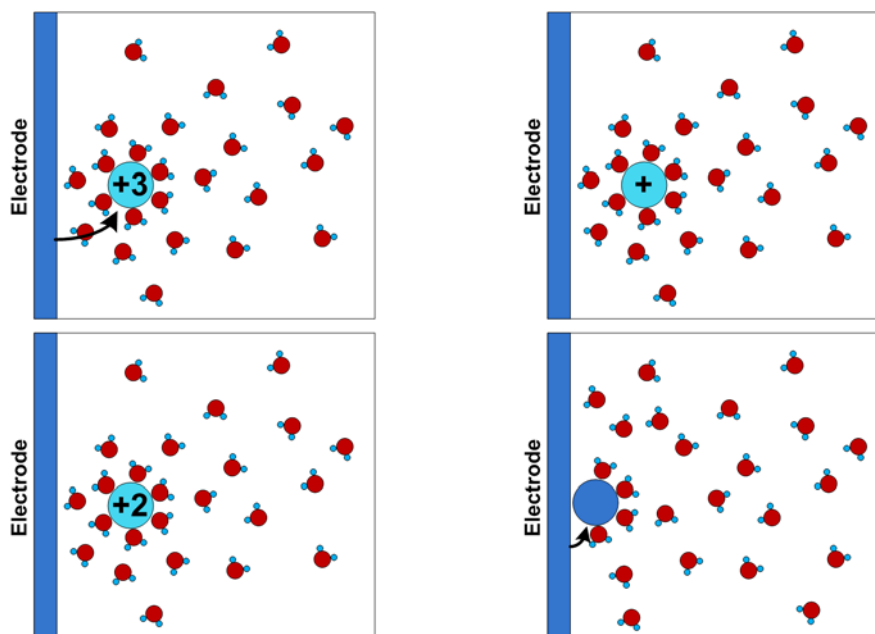


Figure 2.8 In an outer-sphere reaction, electrons directly tunnel to/from the ions (left), whereas inner sphere reactions require an adsorption intermediate step (right).

The reference model for outer-sphere reaction is the Butler-Volmer relationship. It is derived using first order reaction rate theory. In its simplest form, the current-voltage equation is given by [113] :

$$i = i_0 \left(e^{\beta(1-\alpha)\eta} - e^{-\alpha\beta\eta} \right), \quad (2.18)$$

where i_0 is known as the exchange current density, η is the overpotential, and α is a symmetry factor that relates to the energetics of the outer-sphere reaction. For high bias, the equation predicts an exponential behavior. However, in practical electrodes, the current is seldom limited by this exponential relationship. Current might be limited by the intermediate steps taken in a reaction, such as inner-sphere ionic adsorption, or multi-step reactions. Additionally, if the current is not limited by the kinetics of the reaction, then it will be limited by mass transfer, i.e. reactants will not be able to diffuse from the bulk to the surface fast enough to replenish the depleted surface. Such problems are usually handled in the mean-field diffusion-reaction equation. For a vector of species \mathbf{q} , diffusion coefficient matrix \mathbf{D} , and interaction function \mathbf{R} , the vector-equation is given by:

$$\frac{\partial \mathbf{q}}{\partial t} = \mathbf{D} \nabla^2 \mathbf{q} + \mathbf{R}(\mathbf{q}). \quad (2.19)$$

The diffusion-reaction system of equation might be defined in different dimensions. For example, the reaction equation might only be defined on a surface of the electrode, whereas the diffusion can be defined in the bulk of the electrolyte solution. In general, the most important parameter of Equation (2.19) is the function \mathbf{R} , which determines how the reaction depends on the abundance of reactants and their energetics.

2.2.5 The Semiconductor

The semiconductor is perhaps the most widely researched part of the entire BioFET. Its structure is identical to the structure of mainstream field-effect transistors. Proper modeling of the semiconductor generally requires two self-consistent equations: an energy balance equation and a material balance equation. The energy balance equation gives the potential distribution as a function of the profile of charges within it, whereas

the material balance equation uses the kinetic equations of motion for the charges, in addition to the potential profile, to determine the distribution of charges.

The modeling equations used depend on the size scales of the semiconductor. The energy equation is given by Poisson's equation which is valid for all length scales:

$$\varepsilon \nabla^2 V = -\rho, \quad (2.20)$$

where V is the electrostatic potential, ε is the permittivity, and ρ is the charge density. For sizes that are large in comparison with the de Broglie wavelength of the electrons, classical equations of carrier continuity apply. In general, the kinetics of carriers are described by three processes: diffusion, drift, and recombination of both semiconductor carriers: electrons and holes. The diffusion term is assumed to follow Fick's diffusion law, whereas the drift is assumed to follow the linear (Ohmic) mobility expression. The models for recombination are various, and depend on the type of recombination. In the simplest model, the recombination is modeled as a first-order reaction, and characterized by a single time decay constant called the lifetime τ . The carrier continuity equation for a carrier with density n , equilibrium density n_0 , diffusion coefficient D , and mobility μ is:

$$\nabla \cdot (-D \nabla n + \mu n \nabla V) + \frac{\partial n}{\partial t} = -\frac{(n - n_0)}{\tau}. \quad (2.21)$$

The diffusion coefficient and mobility are dependent on the crystal and electronic structure of the semiconductor. They can significantly change from their bulk value if the carriers are confined to the surface of the semiconductor, as in the case of FET devices. Additionally, interaction of the carriers with surface states can give rise to peculiar noise and spatio-temporal variations in the carrier dynamics [71].

When the semiconductor's dimensions are small, the classical transport equations do not adequately represent the motion of carriers. As the size of the semiconductor shrinks, the scattering phenomena, that give rise to the Ohmic behavior, start to diminish. The device goes into the ballistic regime, and the treatment of scattering events becomes more cumbersome. The kinetics of the device are now given by Boltzmann's transport

equation which operates on the probability density function of carriers f in position-momentum space [114] :

$$\frac{\partial f}{\partial t} + \vec{v} \cdot \nabla_r f + \vec{F} \cdot \nabla_p f = \left. \frac{\partial f}{\partial t} \right|_{coll} + s, \quad 2.22$$

where the subscripts r and p denote position and momentum derivatives, respectively, the first term on the right hand side is the collision integral, and s is the carrier generation source (if any). Equation (2.22) is very difficult to handle and approximate expressions for the collision integral and the source term must be used for tractable solutions. Nevertheless, the equation provides a more detailed account of the kinetics of carrier transport in small-scale semiconductors.

When the dimensions of the semiconductor become really small, in the range of nanometers, then Newtonian mechanics start to fail to describe the motion of carriers, and the carriers cannot be seen as rigid point particles anymore. Effects such as barrier tunneling, interference, and Coulomb blockade are commonly observed and cannot be described by classical mechanics. The semiconductor and the carriers will now have to be modeled with a complete quantum mechanical model. This consists of solving Schrödinger's wave equation, coupled with a suitable transport model, self-consistently. Several models for nanoscale transport are available, including Landauer's model, and the more general non-equilibrium Green's function method [115] -[118] .

2.3 Modeling Strategies

From the above discussions, it is clear that there are several heterogeneous areas of simulation, each providing its own insight and view on the underlying physical processes.

In general, the models for a BioFET involve one or more of the following:

1. Mean-field systems of coupled partial differential equations.
2. Individual equations of motion that operate on particles and molecules.
3. Models of the system's energy as a function of coordinates and motion.

When the problems are not amenable to analytical solution, which is the case for most engineering problems, numerical techniques are needed. In this section, some of the various numerical techniques that are used to deal with these problems are given.

2.3.1 Ab-initio Methods

Ab-initio methods are a subset of a wider variety of methods that are used to solve partial differential equations. These methods involve expressing the solution as a linear combination of a “basis set”. The basis set should ideally be complete, meaning that any function can potentially be constructed using a linear combination of the basis set. Mathematically, the basis is the set of components of the function in a finite (or infinite) dimensional Hilbert space. To facilitate tractable numerical computation, however, the basis set is always chosen incomplete. Using a basis set converts the differential equation to an algebraic system of equations, which can be solved on a computer. Schrodinger’s single particle time independent equation for a Hamiltonian operator \mathbf{H} and wavefunction Ψ is given by:

$$\mathbf{H}\psi = E\psi . \quad (2.23)$$

When the wavefunction is expanded in a basis set ϕ_i with coefficients c_i , the equation becomes:

$$\sum_i c_i \mathbf{H} \phi_i = E \sum_i c_i \phi_i . \quad (2.24)$$

Now, if Equation (2.24) is multiplied by ϕ_j and integrated over the entire space (the variational or weak formulation, discussed later in this chapter, when the finite-element method is described), we get a matrix equation in the unknown coefficients vector \mathbf{c} :

$$\mathbf{H}'\mathbf{c} = E\mathbf{S}\mathbf{c} , \quad (2.25)$$

where the matrix \mathbf{H}' is the Hamiltonian matrix in the chosen basis with elements $H_{ji} = \langle \phi_j | \mathbf{H} | \phi_i \rangle$, and \mathbf{S} is the overlap matrix with elements $S_{ji} = \langle \phi_j | \phi_i \rangle$, using Dirac’s

notation. Equation (2.25) is a generalized eigenvalue equation and can be solved on a computer. If the basis set is chosen to be orthonormal, then the overlap matrix reduces to an identity matrix, and Equation (2.25) becomes a regular eigenvalue problem. The biggest computation demand is in evaluating the matrix elements through integration.

The best choice of a basis set for a particular problem is one which will minimize the number of basis functions required to describe a solution, while at the same time maintaining an accurate answer. Ab-initio methods are best suited for resolving the geometry and electronic structure of molecules, since the basis set chosen by most solvers are localized in space and are thus suitable to describe bound electron wavefunctions. Several basis sets are possible. Some of these basis sets are suitable for determination of the molecule's geometry, whereas others are more suitable for band-gap and energy calculations in crystals. The choice of the basis set depends on the required simulation result, required accuracy, and ease of computing. Several basis sets exist, and Table 2.3 summarizes some of them. On the topmost level, chemistry basis sets are classified as Slater-Type Orbitals (STO), or Gaussian-Type Orbitals (GTO). STO provides more accurate description of actual atomic eigenstates, but GTO are more often used, due to their ease of integration [79].

Table 2.3 Some common basis sets used in computational chemistry

<i>Name</i>	<i>Type</i>	<i>Examples</i>	<i>Uses</i>
Split-valence	GTO	Double-zeta (DZ), Triple-zeta (TZ), Quad zeta (QZ), Double zeta with polarization (DZP)	<ul style="list-style-type: none"> • Uses several GTO functions with different decays (zeta) • Useful for properly characterizing long bonds • Better description of chemical bonds than standard GTO or STO • Can add polarization data to better model polarization
Diffuse functions	GTO	Contracted GTO (CGTO)	<ul style="list-style-type: none"> • Can better extract polarization information for electrons far from nucleus • Better basis for valence of heavier atoms and lone pairs
Pople-style	STO	6-31G, 6-311G	<ul style="list-style-type: none"> • Combines several GTOs to make one STO • Useful for some specific molecular structures
Plane wave	-	-	<ul style="list-style-type: none"> • Useful for crystal structure calculations • Useful for periodic systems

In addition to the suitable choice of basis, compensation must be made for reducing the multi-electron problem into a single electron problem. This consists of the problems of interaction between the electrons. This further categorizes the problem into simple **Hartree-Fock (HF)** problems, where the interaction between the electrons is taken on average and correlation effects are neglected, and **Post-Hartree-Fock (PHF)** methods. The PHF methods treat electron correlations in several different ways, giving many different flavors such as:

- Configuration interaction method
- Coupled cluster method
- Møller-Plesset perturbation theory

2.3.2 Molecular Dynamics

In many cases, chemical interactions that cause significant change in chemical composition are rare, and the bonds and molecules retain their normal structures and bond energies to some extent. Additionally, some processes might take time scales that are far too large with respect to the time scales of quantum transitions. In such cases, it would be computationally exhaustive to simulate the entire problem from first principles. Instead, the different interactions are characterized by empirical equations that are fitted to the data from quantum calculations or experiments. When all interactions are modeled, Newton's laws of motion are applied to the entire ensemble of atoms. This is the basic idea of **Molecular Dynamics (MD)** simulations. In some cases, such as when dealing with large proteins, certain segments of the molecule that are known to be stable and not chemically active might be modeled as rigid objects, perhaps with effective potentials. This process is known as coarse-graining [85].

In a complete MD simulation, one would have to account for all possible intermolecular interactions. This includes chemical bond stretching and twisting, electrostatic forces, and van-der-Waals type dispersion interactions. As shown in Figure 2.9, these forces must be calculated for each pair of atoms or rigid entities. As the number of entities increases, however, the number of calculations increases exponentially.

Therefore, in practice, it is desirable to limit the interactions of entities to a certain radius that is decided by the extension of the interaction force field. This requires a continuous log or adjacency information between the entities as time is integrated and the simulation continues. The additional complexity of bookkeeping is more than compensated for by the drastic reduction in the required calculations.

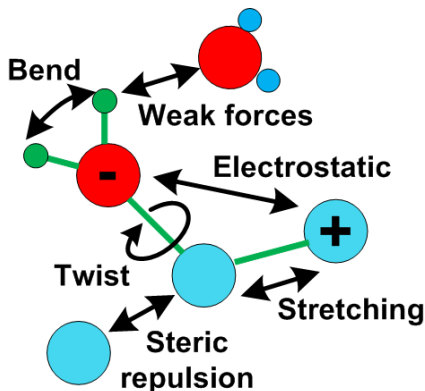


Figure 2.9 Forces in molecular dynamics simulation

Molecular dynamics simulations are classified based on the level of detail that is included in molecules, the type of force field used to model the different interactions, the type of numerical integration that is used, and the model for the aqueous solution surrounding the molecule of interest in biological simulations. Since there is an abundance of water molecules even within a small simulation box size, it can be prohibitive to include the water molecules in their finest detail. Some MD simulations treat the effects of water implicitly, via changes in the dielectric constant. The implicit water might work for many simulations, but information is lost when hydrogen bonds with water are important, or when the water molecules dipole moments are aligned, such as at metallurgical surfaces. In such cases, the most accurate representation would require explicit treatment of water molecules. Several simplified explicit water models are extensively used in MD simulations. Examples include 3-site models such as TIPS [118], TIP3P [119], and SPC/E [120], 4-site models such as TIPS2 [121], TIP4P [119], TIP4P/Ice [122], and 5-site models such as BNS [123] and TIP5P [124].

2.3.3 Monte-Carlo Model

Monte-Carlo (MC) simulations are a class of simulations that rely on random numbers to simulate a phenomenon. Sometimes, the phenomenon itself has inherent randomness. In other cases, the deterministic calculation is too complicated to be rigorously attempted. The Monte-Carlo approach is to perform a calculation on a finite set of samples that are chosen randomly. As the results are aggregated, the approximate solution approaches the rigorous solution. There is no absolute method on how to perform MC computations. Rather, it is derived for the problem at hand. For example, to calculate the area of a complicated two-dimensional closed surface, such as that shown in Figure 2.10, the direct method would be to discretize the area into very small fixed areas and sum them up. The MC approach would be to enclose the shape into a bigger shape of known area, like a square. Then, the MC algorithm sequentially chooses a random two-coordinate point within the square and determines whether or not this point is inside the shape. As the number of samples increases, and assuming uniform sampling, the ratio of points inside the shape to those outside will be equal to the ratio of the two areas, and an estimate of the area of the shape can be produced. Clearly, MC simulations will depend on the quality of the random number generator, the number of samples taken, and any possible statistical bias.

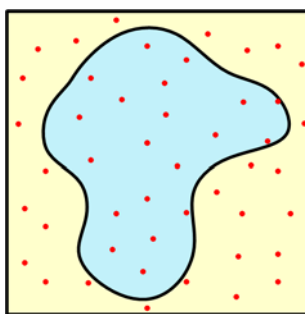


Figure 2.10 Using a Monte-Carlo simulation to estimate the area of the inner complex curve (see text)

When used instead of molecular dynamics, MC simulation cannot produce the kinetics of molecular motion, and is therefore incapable of providing information about reaction kinetics, diffusion coefficients, and mobility of molecules. However, it can still be used to predict average conformation of molecules, radius of gyration, and other mean

distributions. The MC method can be used with statistical mechanical arguments to provide information about lowest energy molecular configurations. This technique, called the Metropolis algorithm, is used in this thesis and will be explained in Chapter 5.

2.4 The Finite-Element Method

The rest of this chapter is dedicated to describe the **Finite-Element-Method** (FEM). This method was used for all simulations in this thesis. It is one of the most widely used methods for solving systems of partial differential equations in Engineering. Some of the advantages of FEM are the following:

1. It is very flexible and scalable. It can be used for problems with very large scale, as well as nanoscale problems.
2. It can handle complex geometries and heterogeneous media well.
3. It discretizes the solution, but not the problem. This makes it superior to the finite-difference method.
4. It is not limited to a single type of basis function.

Of course, these advantages come at the cost of harder implementation of the finite element method, and complicated algorithms for discretizing the solution domain.

2.4.1 The Variational Principle

The mathematics of the finite element analysis is rooted in variational calculus [125] - [127]. One would like to convert a partial differential equation into a system of algebraic equations that can be solved on a computer. If a differential operator L acts on a function $u(\mathbf{r})$, where \mathbf{r} is the position vector, then the partial differential equation:

$$Lu(\mathbf{r})=f \text{ ,} \tag{2.26}$$

defined over a domain Ω , where f is the inhomogeneous term, might have a unique solution for a suitable boundary condition over the boundary of the domain $\partial\Omega$. The concept of existence and uniqueness for a general partial differential equation is not fully

established. However, for all physical models, a unique solution is ensured, provided sufficient boundary conditions exist.

To get the variational (weak) formulation of Equation (2.26), we set an arbitrary function $\mathbf{v}(\mathbf{r})$ defined over the domain Ω . Then, from calculus of variations, Equation (2.26) is equivalent to:

$$\int \mathbf{v}(\mathbf{r}) \mathbf{L}u(\mathbf{r}) d\mathbf{r} = \int f \mathbf{v}(\mathbf{r}) d\mathbf{r} , \quad (2.27)$$

for any continuous function $\mathbf{v}(\mathbf{r})$ in Ω . This function is called a test vector (or function). Now, for a suitable choice of basis set ϕ_i , if we find a solution vector such that Equation (2.27) is satisfied for each member of this basis set, then the equation will be satisfied for any linear combination of this basis set as well, owing to the linearity of the integral. To find the solution vector, it will have to be expressed in the same basis set. Since the basis set is not complete, the solution vector is only the closest vector from the span of the basis ϕ_i to the actual solution. This is the source of approximation in the finite-element method. The challenge is to choose a basis set that can potentially give a good approximation to the solution vector within the simulation domain Ω , without knowing the solution vector itself. One must have a “sense” of the dynamics of the solution vector, where it tends to have a sharper and more detailed profile, and where it would be more flat and with little detail. The basis set must then be chosen to allow more detail at the more interesting part of the domain, while giving little detail in the regions where the solution curve is expected not to show rapid dynamics.

With the solution vector replaced by its expression in the basis set with coefficients u_j , the problem reduces to finding the expansion coefficients of the solution vector. For each basis set used in place of the test vector, we get an equation:

$$\sum_j u_j \int \phi_i(\mathbf{r}) \mathbf{L} \phi_j(\mathbf{r}) d\mathbf{r} = \int f \phi_i(\mathbf{r}) d\mathbf{r} . \quad (2.28)$$

For each ϕ_i , there is a separate equation. Grouping them together results in a matrix equation:

$$\mathbf{K} \mathbf{u} = \mathbf{L} , \quad (2.29)$$

where the matrices are defined as follows:

$$\mathbf{K} = \begin{pmatrix} \int_{\Omega} \phi_1 \mathbf{L} \phi_1 d\mathbf{r} & \int_{\Omega} \phi_1 \mathbf{L} \phi_2 d\mathbf{r} & \dots & \int_{\Omega} \phi_1 \mathbf{L} \phi_n d\mathbf{r} \\ \int_{\Omega} \phi_2 \mathbf{L} \phi_1 d\mathbf{r} & \dots & \dots & \dots \\ \dots & \dots & \dots & \dots \\ \int_{\Omega} \phi_n \mathbf{L} \phi_1 d\mathbf{r} & \dots & \dots & \int_{\Omega} \phi_n \mathbf{L} \phi_n d\mathbf{r} \end{pmatrix}, \mathbf{u} = \begin{pmatrix} u_1 \\ u_2 \\ \dots \\ u_n \end{pmatrix}, \mathbf{L} = \begin{pmatrix} \int_{\Omega} f \phi_1 d\mathbf{r} \\ \int_{\Omega} f \phi_2 d\mathbf{r} \\ \dots \\ \int_{\Omega} f \phi_n d\mathbf{r} \end{pmatrix}. \quad (2.30)$$

For most problems, the matrix \mathbf{K} (called the stiffness matrix) will be rank deficient, meaning that a unique solution does not exist. The boundary conditions are what will allow the solution to be unique. Boundary conditions are defined over manifolds that are one dimension smaller than that of the problem. For a 3-D problem, the boundary is a 2D surface or set of surfaces. For a 2-D problem, the boundary is a line or a set of lines. Typical boundary conditions are defined as Dirichlet, Neumann, Robin, or mixed boundary conditions. These are collectively defined using the following equation, defined on $\partial\Omega$:

$$\mathbf{n} \cdot (c \nabla u + d \mathbf{u}) + q u = g , \quad (2.31)$$

where c, d, q , and g are coefficients related to physical stimuli at the boundaries, and \mathbf{n} is the unit normal vector to the boundary. Equation (2.31) can be seen as yet another differential operator \mathbf{Q} acting on the solution vector:

$$\mathbf{Q} u(\mathbf{r}) = g , \quad (2.32)$$

defined on $\partial\Omega$. Using a similar variational procedure, Equation (2.32) can be converted into an algebraic system of differential equations. In this case, we would need to use boundary basis functions ζ_i , instead of the domain basis functions ϕ_i . The boundary basis functions are always one dimension smaller than the domain basis functions. Additionally, the boundary basis is chosen to coincide with the values of the domain basis functions on the boundary. This way, the expansion coefficients for the solution vector in

the space of boundary basis is the same as the expansion coefficients in the adjacent domain basis functions. With this in mind, Equation (2.32) becomes:

$$\sum_j u_j \int \zeta_i(\mathbf{r}) \mathbf{Q} \zeta_j(\mathbf{r}) d\mathbf{r} = \int g \zeta_i(\mathbf{r}) d\mathbf{r}, \quad (2.33)$$

which ultimately yields the matrix formulation:

$$\mathbf{N}\mathbf{u} = \mathbf{M}, \quad (2.34)$$

where the matrices \mathbf{N} and \mathbf{M} are defined as follows:

$$\mathbf{N} = \begin{pmatrix} \int_{\partial\Omega} \zeta_1 \mathbf{Q} \zeta_1 d\mathbf{r} & \int_{\partial\Omega} \zeta_1 \mathbf{Q} \zeta_2 d\mathbf{r} & \dots & \int_{\partial\Omega} \zeta_1 \mathbf{Q} \zeta_n d\mathbf{r} \\ \int_{\partial\Omega} \zeta_2 \mathbf{Q} \zeta_1 d\mathbf{r} & \cdot & \cdot & \cdot \\ \cdot & \cdot & \cdot & \cdot \\ \int_{\partial\Omega} \zeta_n \mathbf{Q} \zeta_1 d\mathbf{r} & \cdot & \cdot & \int_{\partial\Omega} \zeta_n \mathbf{Q} \zeta_n d\mathbf{r} \end{pmatrix}, \mathbf{M} = \begin{pmatrix} \int_{\partial\Omega} g \zeta_1 d\mathbf{r} \\ \int_{\partial\Omega} g \zeta_2 d\mathbf{r} \\ \cdot \\ \int_{\partial\Omega} g \zeta_n d\mathbf{r} \end{pmatrix}. \quad (2.35)$$

Since Equation (2.34) is not defined on the entire domain, several columns of the matrix \mathbf{N} are expected to be filled with zeros. Additionally, since the number of boundary elements is fewer than the number of domain elements, the matrix \mathbf{N} will not be square. Equation (2.34) is known as the constraint equation. When formulated properly, Equations (2.29) and (2.34) admit a unique solution vector, which is the optimum approximation of our solution within the span of the selected basis set.

If the constraints in Equation (2.34) are all simple Dirichlet conditions, then one may eliminate the boundary coefficients (solutions of Equation (2.34)) from Equation (2.29), which will then yield a system of algebraic equation in the internal nodes, which can easily be solved. The method of elimination can, in general, be used to solve Equations (2.29) and (2.34) for any type of boundary condition. However, one would have to deal with a rank-deficient problem:

$$\begin{pmatrix} \mathbf{K} \\ \mathbf{N} \end{pmatrix} \mathbf{u} = \begin{pmatrix} \mathbf{L} \\ \mathbf{M} \end{pmatrix}. \quad (2.36)$$

This problem can be solved for the vector \mathbf{u} , leaving some redundant zero rows during the Gaussian elimination phase. However, small numerical errors can result in

inaccurate solutions in this case. An alternative method is using Lagrange multipliers to solve the constrained problem. This method, first introduced by Babuška [128], involves extending the solution vector to include new boundary variables \mathbf{p} (the Lagrange multipliers). The system to be solved is then [129]:

$$\begin{pmatrix} \mathbf{K} & \mathbf{N}^T \\ \mathbf{N} & \mathbf{0} \end{pmatrix} \begin{pmatrix} \mathbf{u} \\ \mathbf{p} \end{pmatrix} = \begin{pmatrix} \mathbf{L} \\ \mathbf{M} \end{pmatrix}. \quad (2.37)$$

The vector \mathbf{p} is the outward normal flux of the solution $\partial\mathbf{u}/\partial\mathbf{n}$. The implementation of Equation (2.37) is more memory intensive and requires many more degrees of freedom over the elimination method. However, it is known to provide better estimates of the flux than elimination.

2.4.2 The Finite Element Discretization and Meshing

The difference between the finite element method and other discrete-basis methods (such as ab-initio methods, spectral method, and others), is that the basis functions in the finite-element method are only piece-wise smooth, with a finite extension in space, hence the name finite element. Having a finite extension makes the matrix \mathbf{K} sparse, since most integrals within this matrix will be annihilated. This allows the finite-element algorithm to be more memory-efficient than if using bases with large spatial extension.

Since the basis functions are spatially limited in their extension, the solution domain must be discretized before a suitable basis function set is chosen. Discretization of the space is known as meshing. Figure 2.11 shows an example of a triangular mesh on a domain. A 1-D mesh consists of points (nodes) along the single dimension, and the elements are line segments of differing sizes. In 2-D, elements are often triangular, although quadrilateral elements are common in structural mechanics problems. In 3-D, tetrahedral elements are most commonly used, but brick-shaped elements are also popular.

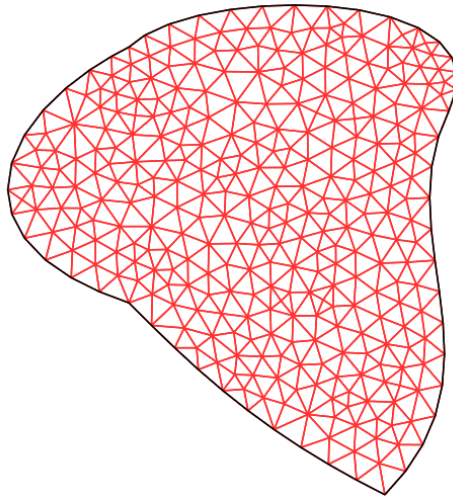


Figure 2.11 Example of a triangular 2D mesh on a subdomain

Meshing can be a complicated task, and care must be taken not to have extremely thin elements that would cause numerical difficulties. In addition, if adjacent mesh elements do not share full edges (called nonconforming mesh), then the assembly of the matrices and integral evaluations can lead to some problems. Figure 2.12 shows an example of a conforming and a non-conforming two-dimensional mesh. In all simulations in this thesis, conforming triangular (and tetrahedral) mesh elements were used.

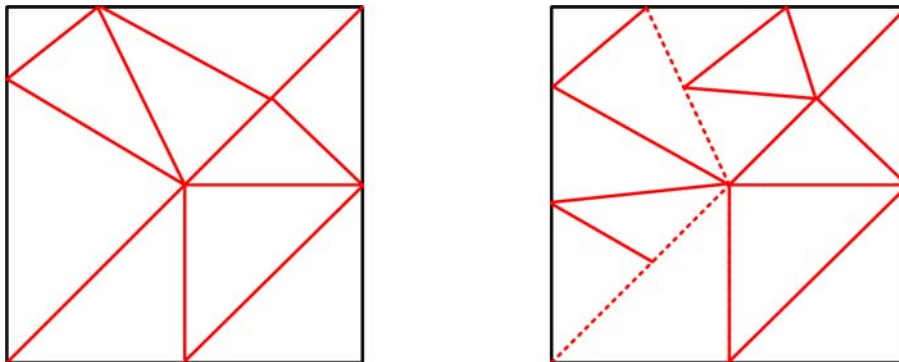


Figure 2.12 Conforming mesh (left) and a non-conforming mesh (right), with the non-conforming edges dashed

Several meshing schemes are available, and an excellent review is given in [130]. The most common meshing technique starts by defining the nodes first, followed by a triangulation. The nodes are chosen with a uniform distribution around the domain, but

they are made denser at certain parts where the solution is expected to have steeper profiles. Once the nodes are in place, a Voronoi diagram is generated. The Voronoi diagram, shown in Figure 2.13, consists of a set of polygons, each including only one node, and the set of all points in the domain that are closer to this node than to any other node. This diagram is achieved by joining the bisector lines of each pair of closest nodes. Once the Voronoi diagram is complete, the Delaunay mesh can be generated by connecting the nodes of every 3 mutually adjacent Voronoi cells.

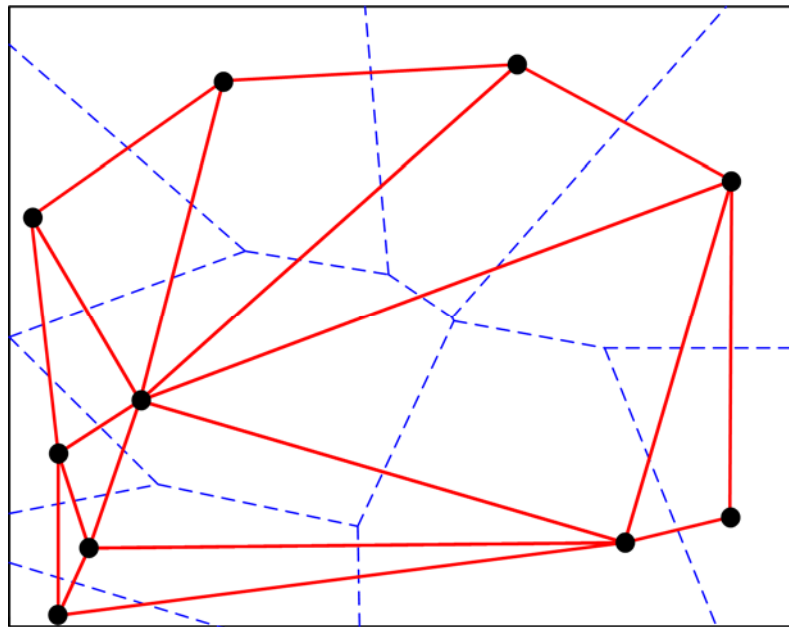


Figure 2.13 Voronoi diagram (dashed), and Delaunay triangulation (solid) of the mesh nodes

After the Delaunay triangulation is complete, the basis functions have to be chosen. In the finite-element method, the number of basis functions needed is the same as the number of nodes, with each basis function having a value of unity at that node and decaying to zero at all adjacent nodes. When constructed this way, only adjacent elements will have possible overlaps. This way, the stiffness matrix is ensured to be sparse and the mathematical computation is simplified. This is in stark contrast with ab-initio methods, wherein the matrix is dense, but the number of elements is small. In one-dimension, the simplest possible element shape function is the linear “hat” functions, shown in Figure 2.14, along with the equivalent 2-D “tent” function.

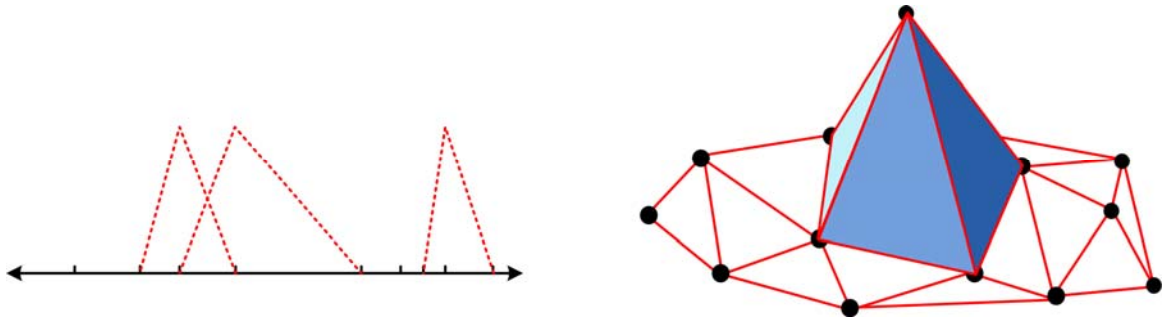


Figure 2.14 Linear 1-D hat functions (left) and 2-D tent function (right)

Several basis functions (also called shape functions) are available, with some being more suited to solve specific problems than others. The basis functions must be selected such that continuity is maintained within each element, as well as across elements. Additionally, they should be easy to integrate. This will help speed up the calculation of the matrices of Equations (2.29) and (2.34), which is the most time-consuming process in the entire finite-element analysis. The most famous element type is the Lagrange element of order k . These elements are polynomials of order k that satisfy continuity between mesh edges. Depending on the order of the Lagrange element used, a different number of points might be needed to fully specify the shape function. For example, in a two-dimensional triangle, a first-order Lagrange element would require three nodes, namely, the nodes on the three vertices of the triangular elements. These are the three mesh nodes that were used to create the mesh. However, if an order 2 Lagrange element is used, six nodes are required: the three mesh nodes, and three other “internal” nodes. Using higher order elements will result in a larger solution vector and many more degrees of freedom. Thus, there is a trade-off between accuracy and computational overhead. In many cases, linear first-order elements suffice, for a mesh that is dense enough.

Since the mesh elements are not of the same size, the required shape function for each element tends to be unique, even when the same shape function class is used (e.g. first-order Lagrange element) and the elements are of the same shape (e.g. triangular in 2-D). However, it is inefficient to keep track of all these functions and perform customized integrations on each element. What is generally done in this case is that the element is

mapped to a master template, with orthogonal coordinates (called the local coordinates). Figure 2.15 shows this mapping for a two-dimensional triangle. The orthogonal coordinates ζ and η are mapped from the real-world x and y coordinates, and they extend through the interval $[0,1]$. Integrations on single elements are often better performed on local coordinates with simple extensions. This allows formulas such as Gauss's quadrature to be used. The geometry transformation is a combination of a rotation and a scaling. The general expression for the relationship between the two frames is given by:

$$\begin{pmatrix} j_{11}^T & j_{12}^T \\ j_{21}^T & j_{22}^T \end{pmatrix} \begin{pmatrix} \zeta \\ \eta \end{pmatrix} = \begin{pmatrix} x \\ y \end{pmatrix}. \quad (2.38)$$

where the coefficients j^T constitute the transformation matrix \mathbf{J}^T . If this matrix is invertible, we can get the real world coordinates (x,y) from the local coordinates:

$$\begin{pmatrix} j_{11}^* & j_{12}^* \\ j_{21}^* & j_{22}^* \end{pmatrix} \begin{pmatrix} x \\ y \end{pmatrix} = \begin{pmatrix} \zeta \\ \eta \end{pmatrix}. \quad (2.39)$$

where the coefficients j^* are for the inverse transformation matrix $\mathbf{J}^* = (\mathbf{J}^T)^{-1}$. When the transformation only involves scaling and rotation, and no warping or bending, then the transformation matrix \mathbf{J}^T is a constant. In this case, it can be seen that the transformation matrix is the transpose of the Jacobian:

$$\mathbf{J} = \begin{pmatrix} \frac{\partial x}{\partial \zeta} & \frac{\partial x}{\partial \eta} \\ \frac{\partial y}{\partial \zeta} & \frac{\partial y}{\partial \eta} \end{pmatrix}. \quad (2.40)$$

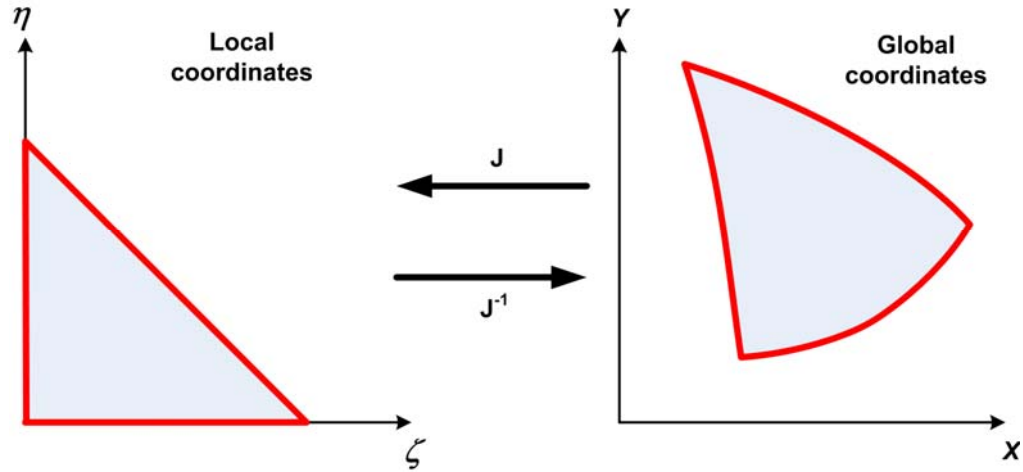


Figure 2.15 Transformation of a triangular element from global coordinates to local coordinates using the Jacobian matrix

When warping exist, the Jacobian is not a constant, but depends on the space coordinates. In the simulations in this thesis, all elements were made non-warping to simplify the calculations. The Jacobian matrix allows derivatives in the global coordinates to be related to the local coordinates:

$$\begin{pmatrix} \frac{\partial f}{\partial \zeta} \\ \frac{\partial f}{\partial \eta} \end{pmatrix} = \mathbf{J} \begin{pmatrix} \frac{\partial f}{\partial x} \\ \frac{\partial f}{\partial y} \end{pmatrix}. \quad (2.41)$$

It also allows the area integration in the global element's domain Ω to be transformed to the local domain $\hat{\Omega}$:

$$\int_{\Omega} f(x, y) dx dy = \int_{\hat{\Omega}} f(j_{11}^T \zeta + j_{12}^T \eta, j_{21}^T \zeta + j_{22}^T \eta) |\mathbf{J}| d\zeta d\eta. \quad (2.42)$$

The process of converting the elements to the local domain and performing the integration to get the different matrices is called assembling. This is the most time consuming process of the entire finite-element method.

2.4.3 Solving the System

Once the matrix assembly is completed, and all the boundary conditions are incorporated, a single matrix equation needs to be solved: $\mathbf{Ax}=\mathbf{b}$. In nonlinear problems, \mathbf{A} and \mathbf{b} can be functions of the solution vector \mathbf{x} . Non-linear problems can be solved by a Newton-Raphson technique that involves linearizing the matrices around a “test” solution vector, and then solving the linearized system. Thus, whether a system is linear or nonlinear, a linear system solver must be used. The most straightforward linear system solver is direct inversion of matrix \mathbf{A} , such that $\mathbf{x}=\mathbf{A}^{-1}\mathbf{b}$. However, this method is very impractical for large matrices and wastes both memory space and computation time. Several other methods to solve matrix equations are available, both commercially and as freeware. One multi-purpose solver that relies on L-U factorization of the \mathbf{A} matrix is the unsymmetric multifrontal method (software implementation is known as UMFPACK) [131]. Although UMFPACK might not be the most memory efficient, it is nonetheless used in this thesis for its simplicity and availability of many implementations of the algorithm. Other less memory-intensive solvers are iterative solvers such as the conjugate gradients solver or multigrid solvers. However, they generally require direct solvers as preconditioners, and have limited range of applicability and convergence.

When memory is not available, an alternative technique to the iterative solvers is an iterative domain decomposition method. There are several advanced methods of domain decomposition. In this thesis, to simplify the programming, the simplest such method was used: the Schwarz alternating method. A domain Ω is split into two or more overlapping domains, as shown in Figure 2.16. First, subdomain Ω_1 is solved with an arbitrary boundary condition on the fictitious boundary $\partial\Omega_1$. This will result in values of the dependent variables for the domain Ω_1 , which includes the fictitious boundary $\partial\Omega_2$. Next, we solve the differential equation in subdomain Ω_2 , using the solution on boundary $\partial\Omega_2$ as Dirichlet boundary conditions. This iteration is repeated until convergence is achieved. Generally, the number of iterations increases as the range of overlap decreases. This method is best suited for parallel processing on multiple computers. However, in the

simulations in this thesis, the method was used on the same computer, to compensate for lack of memory. This, of course, was implemented at the expense of severely increased simulation time.

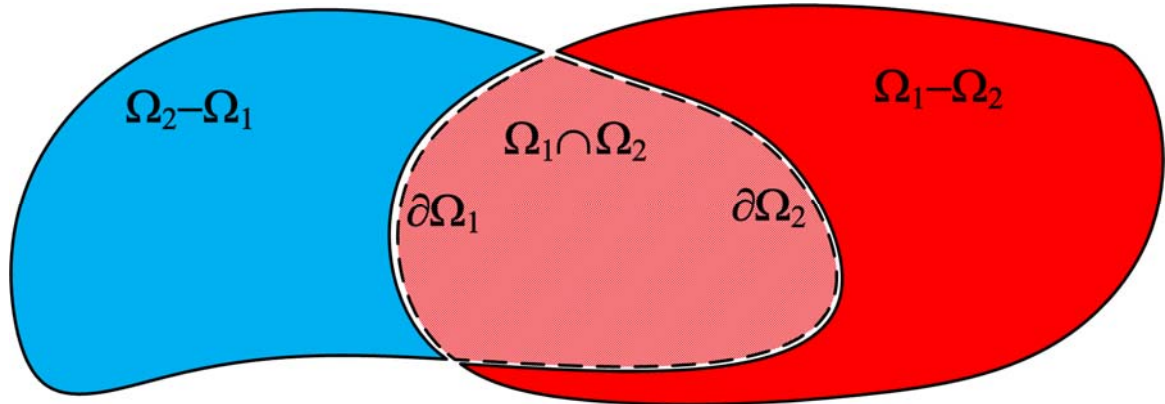


Figure 2.16 Illustration of a domain decomposition method using two overlapping domains.

2.5 Summary

This chapter was intended to introduce the reader to the classes of mathematical problems that are generally encountered when modeling bioelectronic devices and systems. Mean-field partial differential equations, in addition to Monte Carlo methods and classical molecular dynamic simulations, are required to analyze and characterize different aspects of biological sensors. The finite-element method is a versatile technique that is used to solve mean-field systems of partial differential equations in 3 dimensions. A proper FEM implementation requires algorithms for geometry construction, meshing, integration, matrix assembly, and solving. The basics of the finite-element analysis that were detailed in this chapter were used to perform all of the simulations in the chapters to come.

Chapter 3

HIGHER DIMENSION MODELS OF DNA BIOSENSORS

3.1 Introduction

This chapter introduces the two- and three- dimensional mean-free models of the BioFET using the finite-element method. Higher dimensional models are needed to extract information that is not captured by empirical modeling or one-dimensional (1-D) physical modeling. Furthermore, higher-dimensional effects can have significant impact on the sensitivity and reliability of the BioFET. The finite-element model developed in this chapter is used in all subsequent chapters to investigate these effects and assess their importance and the impact on the sensor's performance.

3.2 Goals of Higher Dimensional Modeling

Previous work [71] , [133] modeled a simplified 1-D BioFET structure. These models capture the essentials of the operation of the BioFET: charge attraction or repulsion in the channel by the field-effect, screening of the DNA molecules by the counter-ions, and the chemical activity of the adsorption of protons on the amphoteric insulator layer. However, one-dimensional modeling tends to overestimate the expected response of the BioFET. This is due to assuming that the DNA molecules form a uniform ion-permeable membrane, rather than discrete charged molecules. The neglect of the geometry of the DNA underestimates the amount of screening charge from the solution, which in turn overestimates the amount of charge in the semiconductor. Additionally, the nonlinearities in the response of the solution, as well as the nonlinearities in the response of the

semiconductor, have to be coupled and solved self-consistently. This can only be done when the entire geometry of the sensor and the fine structure of the molecules are incorporated into the same model, which is the aim of higher-dimensional modeling.

Several design and geometry parameters in the BioFET that can affect the output signal are not present in the one-dimensional model. For example, the capacitance from the solution to the source and drain terminals can influence the operation of impedance-based biosensors. With a one-dimensional impedance model, this effect will not be captured. On the other hand, a 2-D or 3-D model of the BioFET will give accurate estimates of these fringing capacitances. These simulations can help a designer optimize the performance of the BioFET with respect to the CMOS post-processing materials and microfluidic structures.

The non-homogeneous distribution of DNA probes, as well as the non-homogeneous adsorption of ions onto the surface of the insulator, both cause variation in the sensed signal. Only a 2-D or 3-D model is capable of capturing this non-homogeneity. Furthermore, a 1-D model cannot distinguish between a hybridized DNA and a single-stranded DNA that was nonspecifically adsorbed to an empty region of the bio-sensitive surface. Finally, the conformation of tethered probes, which are expected to be flailing, rather than rigid molecules, can have a significant impact on the performance, as well as the noise characteristics of the BioFET. Again, higher-dimensional modeling is needed to capture many of these effects.

3.3 Basic Geometry and Equations

3.3.1 Two-Dimensional Case

We start with a two-dimensional BioFET, shown in Figure 3.1. The 2-D model is more memory efficient than the 3-D model, and can successfully capture many higher-dimensional effects. The simulated BioFET was 800nm in length. The length was chosen to be small due to lack of computational resources. The depth of the body or wafer slice is generally a couple hundreds of micrometers in present-day processed wafers. However,

depending on the doping, the potential and charge profiles only vary within the first micrometer or so. The insulator's material was chosen to be SiO_2 with an insulator thickness of 18nm, consistent with the insulator thickness of a conventional CMOS 0.8 μm process. The Debye length in the electrolyte extends only to a few nanometers at electrolyte concentrations in the range of 1mM. Thus, the electrolyte was made to have a depth of around 100nm. The electrolyte was chosen to be KCl, which is very common in hybridization buffer solutions. As a first approximation, the effect of the hybridization buffer was neglected, except in that it would maintain the pH of the solution at neutral 7.0. The change in the pH concentration can influence the DNA hybridization efficiency [25] , but it also causes a change in the amount of adsorbed charges at any surface sites. The semiconductor's body is chosen to be N-type with doping $3 \times 10^{16} \text{ cm}^{-3}$. All dopants are assumed to be ionized at the operating temperature (300K). Surface states are neglected in this model.

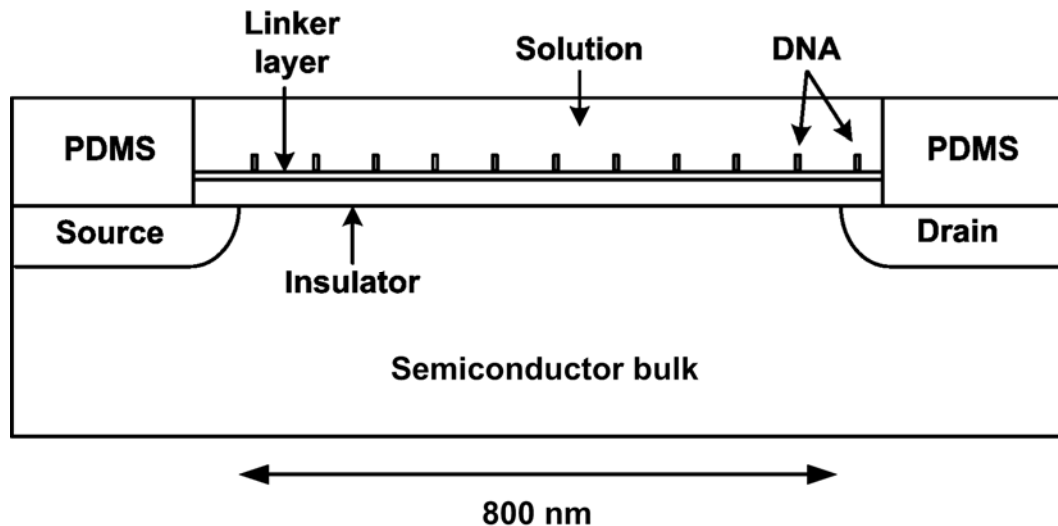


Figure 3.1 2-D model of the BioFET with the DNA probes modeled as rectangles. Depth of the bulk was truncated to save page space.

The DNA molecules are modeled as rigid rectangular shapes with a base width of 2nm and height of 10nm, which corresponds to a height of 30 base-pair DNA. The rectangular model of the DNA allows sidewall screening to be captured in 2-D. The DNA

molecules are placed at equal distances from each other along the channel's length. The phosphate's negative charge on the DNA molecule is assumed to be diffuse within the rectangular structure. The only interactions considered in this model are the electrostatic interactions, since the principle of operation of the BioFET is the field-effect. Higher-order structure and electron density map of the DNA are needed only when chemical interactions are considered. This would be the case, for example, in amperometric electrode-based DNA biosensors, where the transduction is achieved by electrochemical reactions involving the DNA molecule.

The constitutive equations of the model consist of:

1. Equilibrium model of the ionic response to electric fields
2. Model for the surface charging by protons
3. The semiconductor's transport equations

These equations have been used to solve the 1-D BioFET structure [74, 133]. The electrolyte's model is given by the nonlinear **Poisson-Boltzmann (PB)** Equation for a symmetric electrolyte with valence z :

$$-\nabla \cdot (\epsilon \nabla V) = 2zqc_0 \sinh(z\beta V). \quad (3.1)$$

In Equation (3.1), V is the electrostatic potential referenced to a point in the bulk where the equilibrium concentration of ions is c_0 . Equation (3.1) results from a statistical mechanical treatment of the ensemble of ions. The PB distribution of ions ensures maximum entropy of ions while minimizing the total energy of the system. The details are omitted here but can be found in many textbooks on statistical mechanics [134], [135]. The PB equation is valid for systems in thermal equilibrium, where only electrostatic forces influence the ions. In general, this might not be the case, as steric forces can inhibit the aggregation of the finite-sized solvated ions. Additionally, specific adsorption and other chemical reactions which involve removing of the solvation shell will render the PB equation inaccurate. These possible side-reactions are often treated separately in a perturbative manner to the original PB equation. Some of these issues will be discussed later in this chapter.

The PB equation is often linearized to yield a more tractable solution. However, in this work, it is recognized that the high charge of DNA molecules result in a very high zeta potential (in the order of 100mV), which invalidates the linearization of the PB equation, necessitating a fully non-linear solution. This situation is particularly more pronounced when the double layers of adjacent DNA molecules begin to overlap. Linearizing the PB equation can lead to severe errors in the estimate of the amount of inversion charge in the underlying semiconductor.

Close to the insulator's surface, the PB equation often breaks down due to the inability of the ions to approach the surface without losing the hydration shells. One simple treatment (Stern approximation) is to avoid using the PB equation at a fixed distance from the surface (called the **Outer Helmholtz Plane OHP**), and instead use the homogeneous Laplace equation instead. Ions will not be able to pass through the OHP closer to the surface without losing their hydration shell. This can be treated using reaction rate laws of surface chemistry, or using the previously discussed adsorption isotherms. It is assumed that no electron transfer reactions occur at the surface of the insulator (thick enough insulator). Thus, there is no need for an electron transfer reaction treatment at the surface of the insulator.

The kinetics of adsorption of charged molecules in the surface of the SiO₂ insulator can be complicated. On the one hand, a properly deposited SAM with hydrophobic alkane chain should limit the diffusion of hydrated ions to the surface of the insulator. However, due to the high reactivity of the surface sites, even a small number of ions that succeed in diffusing will be able to react at the surface. It has been shown [134] that for a 1-1 solution, the adsorption reactions are given by the following equations of association for the dangling SiOH site:



The first two equations characterize the adsorption of protons in the electrolyte. These equations are the reason for the pH sensitivity of the ion-sensitive FET [137]. The second two equations are for the specific electrostatic adsorption of the charged sites to the cations and anions in the solution. These equations are characterized by first-order equilibrium constants K_a , K_b , K_+ , and K_- . The ion concentrations in these equations refer to their values at the surface (shown in Figure 3.2). The surface concentration, in general, is different from that of the bulk due to the presence of a double layer around the surface. For a dilute electrolyte, the relationship of surface concentrations to the bulk concentration is given by:

$$\begin{aligned} [H_s^+] &= [H_b^+] e^{-\beta(V + \delta H)} \\ [Cl_s^-] &= c_0 e^{\beta(V - \delta Cl)} \\ [Na_s^+] &= c_0 e^{-\beta(V + \delta Na)} \end{aligned} \quad , \quad (3.3)$$

where the voltage V is measured with respect to the bulk of the electrolyte. The values δH , δCl , and δNa are additional partition energies that are related to the required desolvation, as well as the energy needed for penetrating the SAM layer. These energies are often neglected in the literature, but their values can be extremely important in determining the amount of adsorption and the effect on the sensitivity of the biosensor.

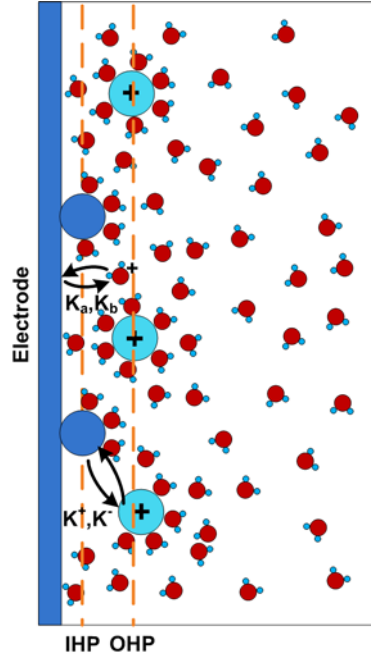


Figure 3.2 Chemical reactions at the OHP and the IHP between the electrode's surface states and the solutions components

The model of the surface adsorption involves a balance between the amount of adsorbents and reaction sites. To accomplish this, a first-order reaction kinetic model is assumed. According to this model, the equilibrium coefficients are given as:

$$\begin{aligned}
 K_a &= \frac{[SiOH][H_s^+]}{[SiOH_2^+]}, & K_b &= \frac{[SiO^-][H_s^+]}{[SiOH]} \\
 K_+ &= \frac{[SiOH_2^+ - Cl^-]}{[SiOH_2^+][Cl_s^-]}, & K_- &= \frac{[SiO^- - Na^+]}{[SiO^-][Na_s^+]}.
 \end{aligned} \tag{3.4}$$

The balance equation for the reactive sites on the surface is given by:

$$[SiOH] + [SiOH_2^+] + [SiO^-] + [SiO^- - Na^+] + [SiOH_2^+ - Cl^-] = N_s, \tag{3.5}$$

where N_s is the total surface site density. The components SiO^- and $SiOH_2^+$ are treated as surface charges, whereas the adsorbed Na^+ and Cl^- are treated as fixed charges in the **Inner Helmholtz Plane (IHP)** (Figure 3.2). The total surface charge density on the surface of the insulator, as well as on the Inner Helmholtz Plane, can be derived from Equations

(3.4) and (3.5). After some tedious algebra, the charge on the insulator's surface σ_0 is given by:

$$\begin{aligned}\sigma_0 &= q \left[[SiOH_2^+] + [SiOH_2^+ - Cl^-] - [SiO^-] - [SiO^- - Na^+] \right] \\ &= qN_s \left(\frac{[H_s^+]^2 (1 + K_+ [Cl_s^-]) - K_a K_b (1 + K_- [Na_s^+])}{[H_s^+]^2 (1 + K_+ [Cl_s^-]) + K_a K_b (1 + K_- [Na_s^+]) + [H_s^+] K_a} \right),\end{aligned}\quad (3.6)$$

and the charge on the IHP σ_{IHP} is:

$$\begin{aligned}\sigma_{IHP} &= q \left[[SiO^- - Na^+] - [SiOH_2^+ - Cl^-] \right] \\ &= qN_s \left(\frac{K_a K_b K_- [Na_s^+] - [H_s^+]^2 K_+ [Cl_s^-]}{[H_s^+]^2 (1 + K_+ [Cl_s^-]) + K_a K_b (1 + K_- [Na_s^+]) + [H_s^+] K_a} \right).\end{aligned}\quad (3.7)$$

Equations (3.6) and (3.7), along with Equation (3.3), allow for the determination of the surface charge as a function of the surface electrostatic potential. This surface charge appears in the electrostatic boundary condition at the insulator's surface, as well as at the IHP:

$$\begin{aligned}\mathbf{n} \cdot (\nabla \mathcal{E}V)_{SiO_2/solution} &= -\sigma_0 \\ \mathbf{n} \cdot (\nabla \mathcal{E}V)_{iIHP} &= -\sigma_{IHP}\end{aligned}\quad (3.8)$$

Within the semiconductor, Poisson's equation needs to be coupled to a suitable transport equation. Since the FET size is well above the ballistic limit, normal diffusive equations apply for both electrons and holes. Thus, the charge density/potential profile in the semiconductor is described by the following system of equations (from Equations (2.20) and (2.21)):

$$\begin{aligned}\nabla \cdot (\epsilon \nabla V) &= -q(p - n \pm N) \\ \nabla \cdot (\vec{J}_p) &= -q \nabla \cdot (D_p \nabla p + \mu_p p \nabla V) = 0 \\ \nabla \cdot (\vec{J}_n) &= q \nabla \cdot (D_n \nabla n - \mu_n n \nabla V) = 0\end{aligned}\quad (3.9)$$

In Equation (3.9), N is the ionized doping density of the semiconductor's channel, and p and n are the volumetric charge densities of the holes and electrons, respectively. The plus sign in the first equation is for p-type semiconductor. Assuming low bias, the recombination current component was eliminated from Equation (2.21), and the time

dependent term was also eliminated. Thus, Equation (3.9) is a steady-state, low-bias transport model for the FET.

At the insulator/semiconductor interface, the boundary conditions of the electrostatic potential require continuity of the electrical displacement, unless there are surface charges at the interface [4] . Generally, for properly annealed Si/SiO₂ heterostructures, annealing reduced the trap density to around 10¹⁰ cm⁻² [138] , whose charging then has minimal effect on the threshold voltage variation. These surface charges are generally assumed to be fully charged, irrespective of the applied gate bias. This accumulated surface charge σ_s interferes with the electrostatic boundary conditions at this interface:

$$\mathbf{n} \cdot (\nabla \epsilon V)_{Si/SiO_2} = -\sigma_s . \quad (3.10)$$

Equations (3.1), (3.3), (3.6), (3.7), and (3.9), as well as boundary conditions (3.8) and (3.10), constitute the model needed to solve for the potential and charge distribution in all regions of the BioFET. Of course, the potential references for Equation (3.1) and that of Equation (3.9) are not compatible, as the former is referenced to the bulk of the solution, whereas the latter is referenced to the bulk of the semiconductor. In order to unify the definition of potentials in the model, both potentials are re-referenced to the vacuum level of a zero-biased metallic contact. Thus, the potentials (V) in Equations (3.1) and (3.3) are replaced by the value:

$$V - (V_G + \chi_M - \chi_{sol} - E_{ref}) , \quad (3.11)$$

where χ_M and χ_{sol} are the electron affinities of the metal contact and the solution, respectively, E_{ref} is the electrode potential, and V_G is the voltage applied to the reference electrode. Similarly, the potential (V) in Equation (3.9) is replaced by:

$$V - (V_B + \chi_M - \chi_{Si} - E_g / 2 - \phi_F) , \quad (3.12)$$

where χ_{Si} is the semiconductor's electron affinity, E_g is the energy band gap, V_B is the voltage applied to the body contact, and ϕ_F is the Fermi level of the semiconductor, given by:

$$\phi_F = \mp \beta^{-1} \ln \left(\frac{N}{n_i} \right), \quad (3.13)$$

where the minus sign is for a p-type semiconductor. For all mobile charge-free regions of space such as the gate insulator, or the sidewall PDMS structures, Laplace's equation is valid without any transformation done on the potential.

With the voltage reference homogenized over the entire BioFET structure, it remains a task to specify the outer boundary conditions. All boundaries that are not in immediate contact with a lead will have Neumann reflecting boundary conditions. Of course, this will only be accurate if the geometry of the device is made large enough to allow the electric fields to subside. This is a big source of redundancy and needless computation, since several thousand degrees of freedom are calculated for a more accurate total current calculation.

At the reference electrode boundary, as well as the boundaries in contact with the source, drain, and body terminals, Dirichlet conditions are needed. Close to these boundaries, there exist sharp potential and charge profiles similar to the double layer. If the contacts are assumed to be Ohmic, there is no real need to model these regions as they require many degrees of freedom in the finite-element mesh, and generally do not change the voltage-current characteristics if the junction is made properly Ohmic. The analysis is completely different in the case of nanowire sensors, as the junctions cannot be neglected. The Dirichlet conditions for the Reference electrode, body, source, and drain junctions are given by:

$$\begin{aligned} V_{\partial REF} &= V_G + (\chi_M - \chi_{sol} - E_{ref}) \\ V_{\partial B} &= V_B + (\chi_M - \chi_{Si} - E_g / 2 - \phi_F) \\ V_{\partial S} &= V_S + (\chi_M - \chi_{Si} - E_g / 2 - \phi_F) \\ V_{\partial D} &= V_D + (\chi_M - \chi_{Si} - E_g / 2 - \phi_F) \end{aligned} \quad (3.14)$$

where the voltages V_S and V_D are the voltages applied to the leads of the source and drain terminals, respectively.

Additionally, boundary conditions for the electron and hole densities are needed at all semiconductor boundaries. Since no out-flux of carriers occurs at the

insulator/semiconductor interface, Neumann boundary conditions are applied for both carriers. For the contact boundaries, the condition on the carriers depends on the kinetics of carrier injection between the metal and the semiconductor. If a perfect contact is assumed with infinite recombination velocity, then the carrier concentration at the surface will be the value at thermal equilibrium, given by:

$$\begin{aligned}n &= n_i e^{\beta(V - (\chi_M - \chi_{Si} - E_g/2 - \phi_F))} \\p &= n_i e^{-\beta(V - (\chi_M - \chi_{Si} - E_g/2 - \phi_F))}\end{aligned}\tag{3.15}$$

where n_i is the intrinsic thermally generated carrier density, and the voltage V is replaced by the applied value at the source, drain, or body terminals.

A sample mesh for the 2-D problem is shown in Figure 3.3. The mesh is made to exponentially coarsen with the distance from the DNA molecule edges, accommodating the double layer formation. A similar exponential decaying mesh is applied along the depth of the channel, accommodating the fast dynamics of the potential and charge profiles. The mesh is finest within the insulator layer. This is where the 2-D effects are most important. It is important that the discreteness of the DNA charge is communicated properly to the semiconductor, and this will only be accomplished with a fine mesh within the insulator. The size of the mesh elements within the electrolyte are made smaller than those in the semiconductor. This is because the PB equation of the electrolyte is extremely nonlinear and results in a very steep profile, whereas the semiconductor's equations are better behaved.

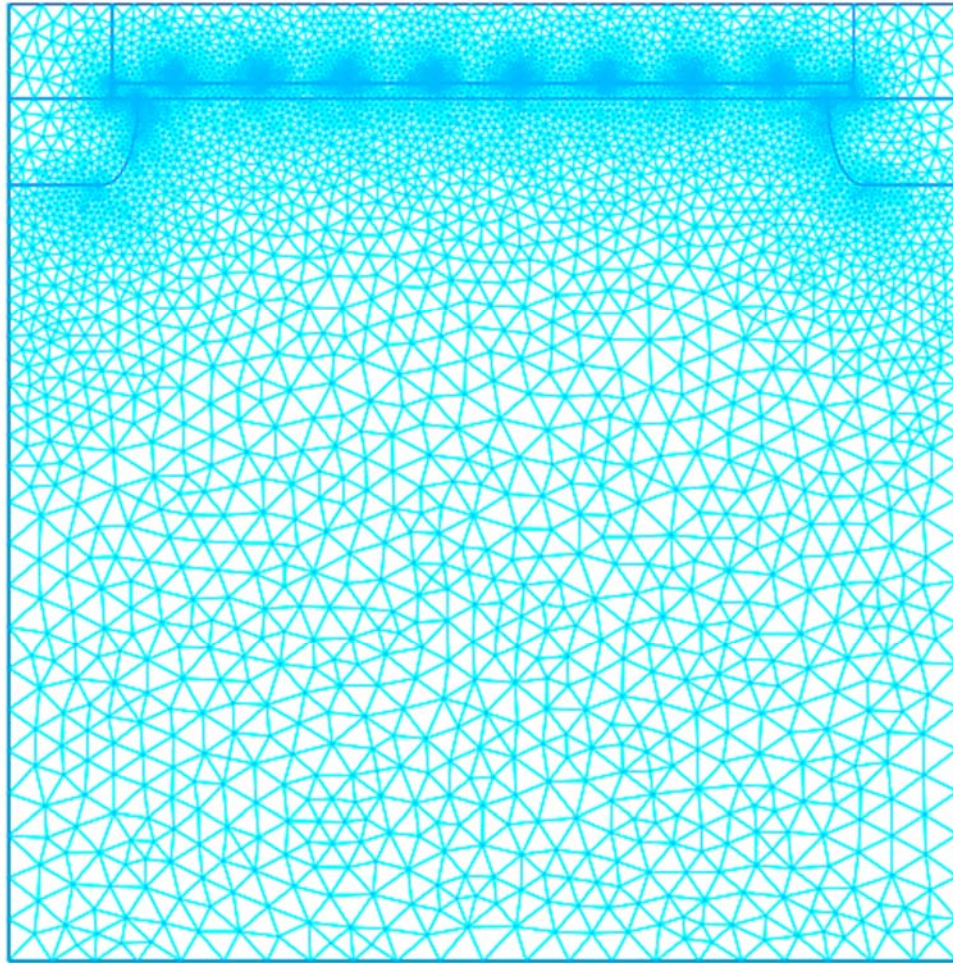


Figure 3.3 Sample 2-D mesh for the BioFET. The mesh is made finer around the DNA molecules (not visible in this figure due to surrounding mesh) for added accuracy at the critical locations

3.3.2 Three-Dimensional Case

The 3-D model of the BioFET follows the exact same equations of the 2-D model given above. The advantage of the 3-D model is that it allows for the complete cylindrical screening of the DNA charges, as compared with the 2-D model. It will also be useful when conducting Monte-Carlo simulations on the positions of the DNA molecules (Chapter 5). However, the added value that comes with 3-D modeling is at the expense of

significantly higher computation time, which prohibits its use for parametric calculations when using a modest computer.

To make the 3-D simulation possible, the simulation is conducted on a “slice” of the BioFET, shown in Figure 3.4. The slice is taken along the length of the device, and is made thin enough to yield manageable degrees of freedom, but wide enough to accommodate the cylindrical charge screening profile around the DNA. The additional boundaries in the 3-D geometry (those along the slicing planes of the BioFET), cannot be given Neumann conditions, since these are artificial boundaries that do not impose Neumann conditions. In an attempt to emulate the bulk behavior of the BioFET, the opposite boundaries in line with the slicing planes are given periodic boundary conditions. This allows for the treatment of “spill-over” of the ionic and potential profile. This is illustrated with the aid of Figure 3.5. As DNA molecules are placed closer to the hypothetical border, the double layer would have to cross the boundary. Periodic boundary conditions will allow this boundary to reflect the remainder of the profile to the opposite boundary. Thus, a bulk effect is established.

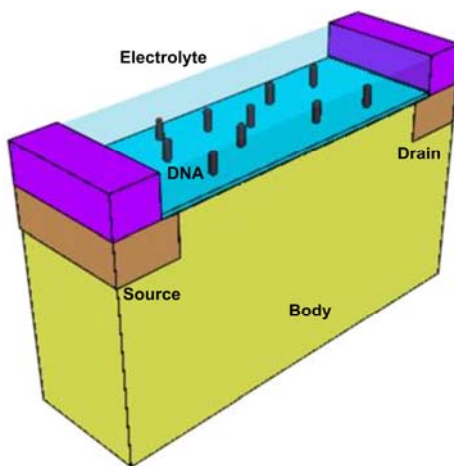


Figure 3.4 Cartoon illustration of the 3-D slice of a BioFET with cylindrical DNA molecules placed randomly on the SAM surface. A tetrahedral mesh is applied to the entire domain for solving.

Periodic boundary conditions also reduce the degrees of freedom of the 3-D problem, as the elements on the opposite periodic boundaries are made to have the same values, and the same normal derivatives (i.e. the same degrees of freedom). This helps

with faster convergence of the 3-D problem. However, for easy implementation of the periodic boundary condition, the boundary meshes on the periodic boundaries must be made identical. If the meshes do not match, a complicated interpolation step would have to be done to map the variables from one boundary to another. Therefore, the meshing of the 3-D geometry is done in steps: First, one boundary is meshed with a 2-D mesh, respecting the mesh density requirements within different regions in the device. Then, this mesh is mirror-copied onto the opposite boundary. Finally, the subdomains are meshed, while respecting the mesh nodes and elements of these boundaries.

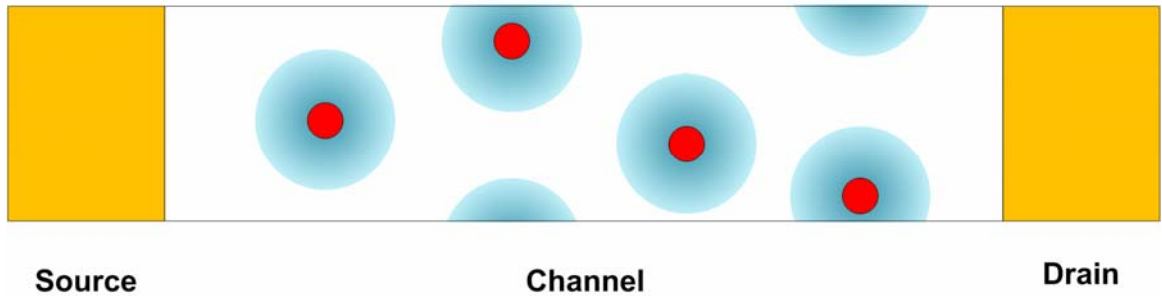


Figure 3.5 Top view of the 3-D BioFET channel. Periodic boundary conditions applied to the top and bottom boundaries in the figure allow spillover charge profiles to be reflected to the opposite boundary, causing a bulk effect overall

3.4 Numerical Conditioning

In both 2-D and 3-D cases, the system of equations for the BioFET involve variables V , n , and p . The values of the carrier concentrations are several orders of magnitude larger than the values of the electrostatic potential. This makes the numerical calculation very stiff, resulting in severely erroneous estimates of the carrier densities [139]. For this reason, the carriers are scaled according to the following “quasi-Fermi” transformation:

$$\begin{aligned} n &= n_i e^{\beta(V - (V_{qfn} - \chi_{Si} - E_g/2 - \phi_F))} \\ p &= n_i e^{-\beta(V - (V_{qfp} - \chi_{Si} - E_g/2 - \phi_F))} \end{aligned} \quad (3.16)$$

where the new variables V_{qfn} and V_{qfp} are the quasi-Fermi potentials which have values in the same range as the electrostatic vacuum level potential. Utilizing these transformations, as well as Einstein's relation:

$$D_{n,p} = \beta^{-1} \mu_{n,p}, \quad (3.17)$$

the transport equations reduce to the following:

$$\begin{aligned} \nabla \cdot \left(-q \mu_n n_i e^{\beta(V - V_{qfn} + \chi_{Si} + E_g/2)} \right) &= 0 \\ \nabla \cdot \left(-q \mu_p p_i e^{-\beta(V - V_{qfp} + \chi_{Si} + E_g/2)} \right) &= 0 \end{aligned} \quad (3.18)$$

These equations are now coupled to Poisson's equation for a less-stiff problem that is easier to converge. With this transformation, the Dirichlet boundary conditions at the contacts become:

$$V_{qf} = V_X + \chi_M, \quad (3.19)$$

where V_X is the corresponding bias at the boundary, and Equation (3.19) applies to both quasi-Fermi levels.

3.5 Numerical Results and Design Implications

The 2-D and 3-D models discussed above are applied to a BioFET structure, using the finite-element method. The current is calculated by integrating the current density along the source (or drain) boundary, in absence of any DNA molecules:

$$I = \int_{\partial\Omega} \left(\vec{J}_p + \vec{J}_n \right) \cdot d\vec{s}. \quad (3.20)$$

Figure 3.6 shows a comparison of the 1-D, 2-D and 3-D simulations of the drain current as a function of the drain bias, for three different gate voltages. The 1-D simulation was done using a charge-sheet model that was developed earlier [4]. These simulations are conducted for a BioFET with the same geometry (the 3-D simulation is normalized to the device's width). From the figure, it can be seen that the simulations follow the expected curve for a FET. The 2-D and 3-D simulations both predict a channel-length modulation effect. This is expected since the channel-length modulation is

a 2-D effect. The 3-D model does not give any additional insight or detail in this case, since the entire FET is a two-dimensional structure with inherent symmetry of the potential and the electric field along the width of the device. The small discrepancy between the 2-D and 3-D simulations is most likely due to the higher resolution mesh, and higher order elements, used in the 2-D simulation. The 3-D simulation does not easily admit such high resolution without the need for excessive memory and computation power, or exceedingly longer simulation times through the use of overlapping domain decomposition.

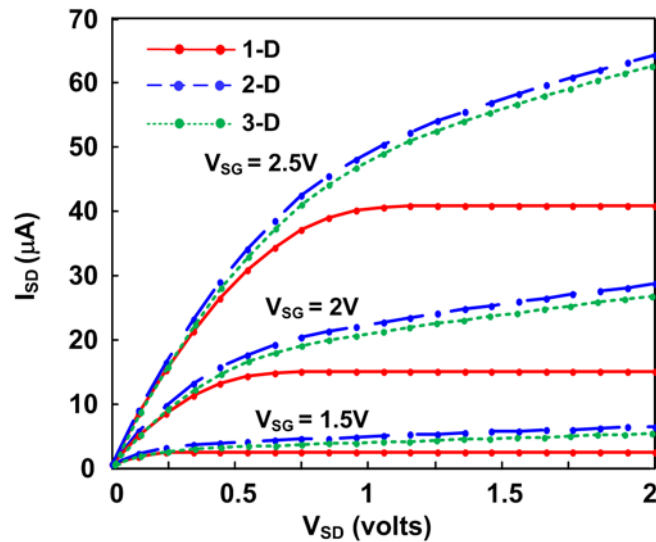


Figure 3.6 Comparison of the 1-D, 2-D, and 3-D simulation of the drain current in the BioFET with similar characteristics.

The hybridization signal in the BioFET is taken as the difference in the drain current before and after successful hybridization. Hybridization is modeled by doubling the charge density on the DNA cylinders. The single-stranded volumetric charge density of the DNA is taken as a homogeneous value of $1.49 \times 10^{-10} \text{ C}/\mu\text{m}^3$. Doubling this charge will cause additional inversion in the underlying semiconductor, which then increases the current (in the case of a P-type FET). Figure 3.7 shows the 1-D, 2-D, and 3-D modeled hybridization signals of a BioFET with the same size, and the same DNA layer density. The advantage of higher-dimension simulation is clear in this result. The 2-D and 3-D results predict lower sensitivity of the BioFET due to the better-resolved screening of the

molecule. It is clear, in this case, that 1-D results give only a rough estimate of the transduced signal and cannot be utilized to probe finer details of the BioFET. The relative error between the 2-D and 1-D hybridization signals (with respect to their absolute values) as a function of the drain bias is shown in Figure 3.8a. It is seen that the 2-D response can be as low as 50% of the 1-D response, in agreement with another attempt at 2-D modeling [140]. The 3-D/1-D relative signal shows values as low as 8% (Figure 3.8b), agreeing again with the worst-case results reported in [140]. This indicates the necessity to include the cylindrical DNA model and to properly model the entire screening effect of each molecule.

The results of Figure 3.8 show another interesting phenomenon. Whereas the 2-D model shows an increase of the sensitivity with respect to that of the 1-D problem with increased saturation operation, the 3-D/1-D plot shows that this relative sensitivity is decreasing. This apparent contrast can be resolved by noting that both the 2-D and 3-D models predict the channel-length modulation effect and the increase in transconductance with deeper saturation operation, whereas only the 3-D model accurately describes the three-dimensional image charge cloud underneath the DNA molecule in the semiconductor. Deeper saturation operation causes a stronger lateral field interaction with this cloud charge and strips the channel of a portion of this charge. This effect is more pronounced in 3-D than in 2-D simulation. It therefore seems that this reduction of sensitivity overcomes the increase in sensitivity when the BioFET is placed in deep saturation. This effect is absent in the 2-D simulation and indicates that the 2-D approximation is insufficient for precision calculations, and that the error can be significantly large when dealing with a simplified model.

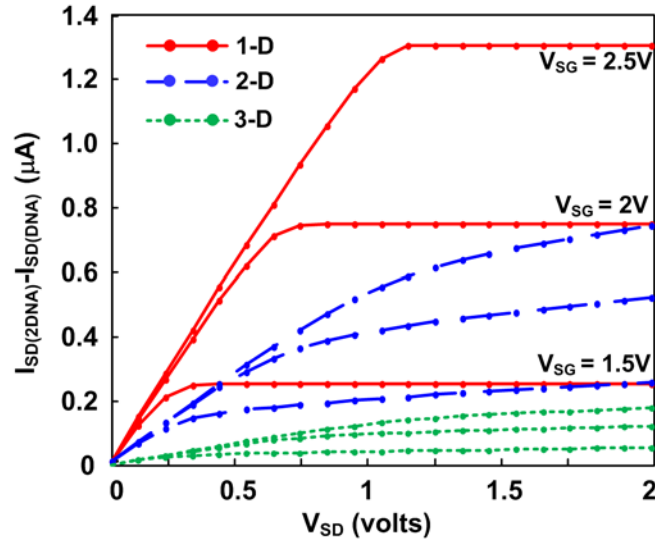


Figure 3.7 Comparison between the simulated hybridization current changes in 1-D, 2-D, and 3-D models, showing the drastic reduction in case of the 3-D model.

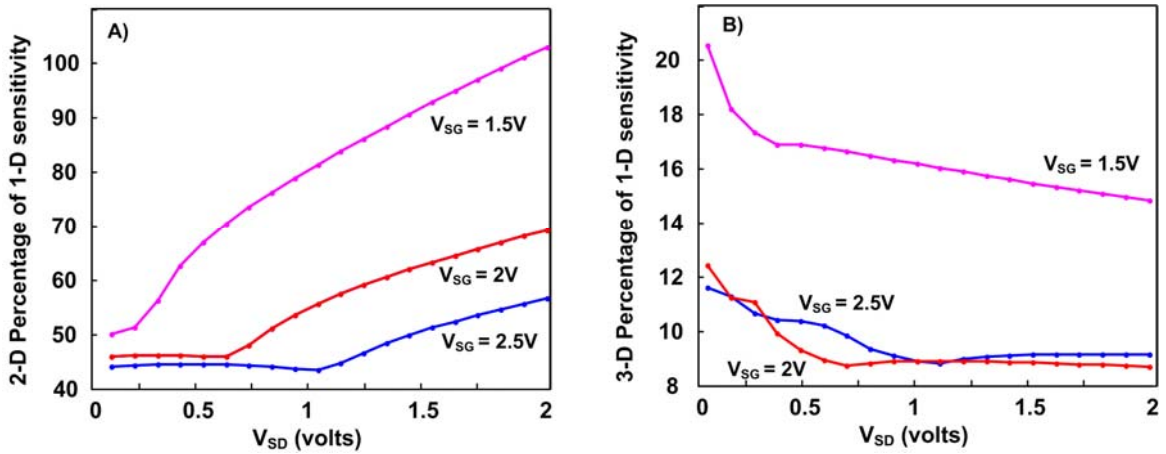


Figure 3.8 Relative sensitivity of the BioFET between: A) 2-D and 1-D models, B) 3-D and 1-D models

From Figure 3.7, it can be seen that the channel length modulation tends to help with the sensitivity of the BioFET, allowing devices in deeper saturation to be more sensitive to the hybridized DNA signal, as evidenced by the increased signal magnitude. However, it is important to see whether there are any side-effects to this apparent advantage. While in deep saturation, the pinch-off region close to the drain is almost depleted of inversion charges. This gives a hint that this would make that area of the FET insensitive to the DNA charges. The next FEM simulation was conducted to see if this is

in fact the case. By placing the same number of DNA molecules at different aggregations along the length of the BioFET, and running the simulations at threshold inversion, a sweep of the current versus the drain voltage is shown in Figure 3.9. The simulation was carried out four times with the DNA molecules scattered uniformly along the channel “sparse”, made closer to the center, source, and drain of the channel. The simulation results show that the evenly distributed positioning of the DNA molecules results in the most optimum sensitivity, and that DNA molecules that form aggregates can have sensitivities reduced by more than 50% (see figure). This result explains the difficulty in achieving repeatable measurements, and indicates the need to have adequate control over the DNA film growth.

It is noticed from Figure 3.9 that the error between the optimum, sparsely placed probes, and that where the probes are placed at the center is maximum at the onset of saturation, while the error gets smaller in deep saturation or deep linear mode. The reason behind this is that in the saturated transistor, the drain region is desensitized to the probes close to it. Thus, in the sparse case, there are several DNA probes whose charge will not influence the output signal. The number of such DNA probes increases as the device goes deeper into saturation. When the DNA probes are aggregated closer to the drain, hybridization of targets to these probes will have minimal effect on the change in the current.

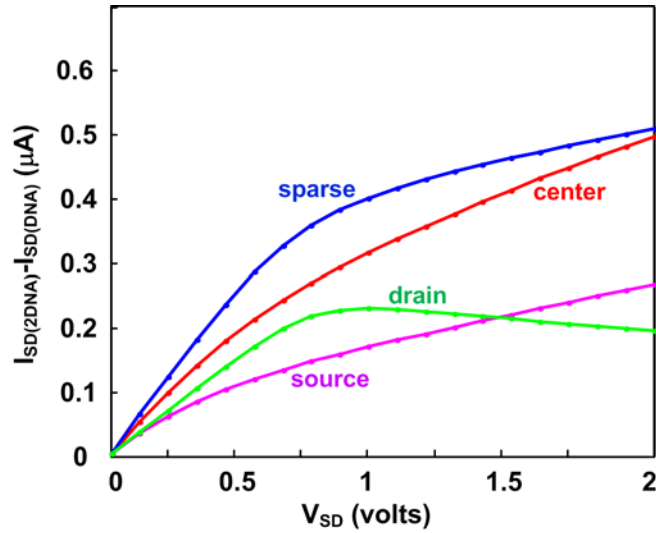


Figure 3.9 Variation in the hybridization current change with positioning of the DNA molecules along the channel's length

The asymmetry of the sensitivity of a saturated BioFET leads to some useful design guidelines. Firstly, it is important to try and direct the DNA hybridization to be as diffuse as possible. While diffusion control at such a small volume might not be achievable, the SAM layer that tethers the DNA will have to be dense, such that DNA molecules are equally likely to attach to any point at the surface. A uniform, completely dense SAM layer is essential to proper operation of the BioFET. This is needed for another reason as well. The SAM layer must not allow any permeation of ions. This is accomplished by establishing a highly hydrophobic layer, which is achieved when the SAM alkane backbones aggregate by hydrophobic forces and form a strong lipid-like membrane. Figure 3.10 shows simulated results of the shift in the surface potential due to hybridization (equivalent to the shift in the threshold voltage), as a function of the electrolyte's concentration, for the case of a permeable membrane and a non-permeable membrane [142]. Whereas it is expected that the increase in electrolytic strength will cause a reduction in the sensitivity due to increased DNA charge screening [4], it can clearly be seen that the ion-permeable SAM layer results in significantly reduced sensitivity over the case when the membrane is perfect and completely ion-impermeable. This reduction of sensitivity increases exponentially with the thickness of the SAM layer.

This is the reason why the SAM molecules generally used are propyl moieties which contain only three carbon atoms. As can be seen from the figure, the reduction in sensitivity can approach 80%, which is quite significant.

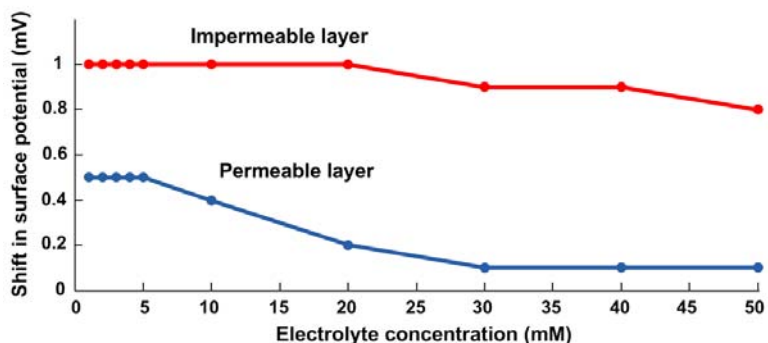


Figure 3.10 Shift in the average surface potential of the BioFET as a function of the electrolyte concentration, in the case of a perfect SAM monolayer and an ion-permeable layer

One way to desensitize the BioFET to the drain-source asymmetry is to make the device very long, thus keeping the insensitive area close to the drain relatively small. However, making the device long reduces the sensitivity of the BioFET, takes up more chip space, and requires more DNA probes and larger settling times for the sensor. For nanowires and short-channel BioFET sensors, the simulations above result in the proposal that the hybridization measurements be carried out twice, while interchanging the source and drain terminals. The averaged result will allow a better estimate of the density of hybridized sites than a single measurement. Figure 3.11 shows a simulation of the hybridization current with several randomly placed DNA molecules within the channel. The simulation is carried out at threshold voltage gate bias of the device and deeply saturated mode of operation of the FET for 60 random positions of the DNA molecules. The variation in the sensed current will be presented in more detail in Chapter 6. However, for this simulation, the variation in the current with one source-drain polarity is higher than if the current at the two different polarities is measured and then averaged out. The calculated standard deviation of the first curve (source terminal on the left) is 0.24nA, and 0.23nA for the second curve (source terminal on the right). The calculated standard deviation of the averaged current is 0.18nA, which represents around 24%

improvement in the accuracy of the measurement. This improvement in the accuracy is an indication that the variations in the first two curves are correlated with the positions of the DNA molecules within the channel. It can therefore be seen that there is potential for discrepancy in results if a fixed terminal is taken as the source. However, when the measurement is done in both directions and averaged out, the sensor gives a more stable result that is less dependent on the position of the DNA molecules within the channel. Such asymmetric measurement would be even more essential in small-geometry DNA biosensors, such as silicon nanowire biosensors.

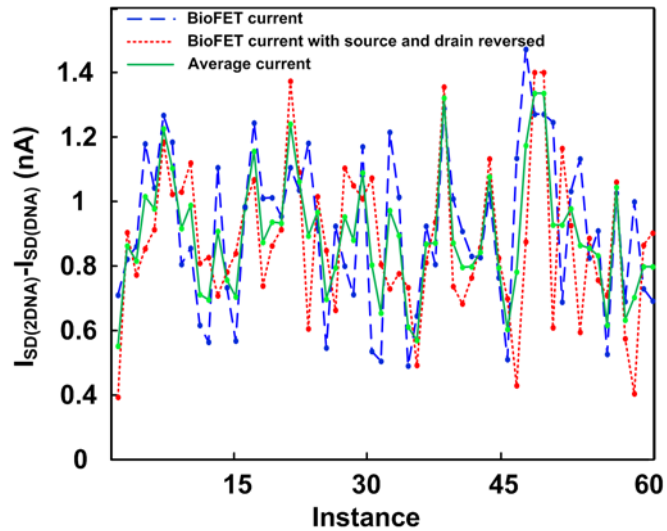


Figure 3.11 Simulated output current for three cases: 1) With one source-drain polarity, 2) with an inverted polarity, and 3) the averaged result of these two measurements

The final simulation in this section concerns the effect of nonspecific binding to the SAM layer. The sticky ends of the SAM layer that have not been used to capture probes can trap nonspecific DNA targets or other protein molecules in the solution. Generally, after incubation of the targets in the hybridization buffer, the sensor is washed to eliminate any non-specific adsorbates on the surface. However, washing might not suffice if the spurious molecules are covalently attached to the SAM layer or if the SAM layer is not very dense and could result in molecules getting entangled.

Due to the nonlinearity of the PB equations and the transport equations in the semiconductor, the local sensor response (aggregated charge in the semiconductor) at a

specific location is not linearly proportional to the amount of charge on top of the insulator. This is very disadvantageous for the BioFET, because the legitimate hybridization signal results when the probe's charge doubles. If the probe had no charge, then the hybridization signal would be much larger. This is exactly what happens when a non-specific adsorption occurs. The site of adsorption originally has no charge, and the sensitivity to the non-specific adsorbates is significantly high. This is shown in the simulation result of Figure 3.12. Here, the adsorption of nonspecific molecules was modeled as an addition of extra probe DNA molecules onto vacant sites in the BioFET. The simulation was run at threshold bias. The result of Figure 3.12 clearly shows that irrespective of the region of operation, the sensitivity to the nonspecifically adsorbed molecules is much larger (by a factor of around 6) than the legitimate hybridization signal.

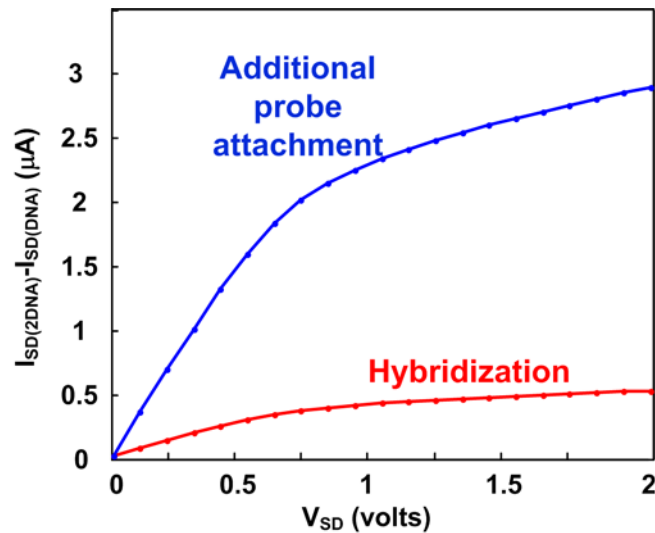


Figure 3.12 Simulated response of BioFET to hybridized charge, and to charge from spurious nonspecific molecules

3.6 Other Effects

The model developed in this chapter thus far is simplified in many ways. The DNA molecule is modeled as a cylinder block with diffuse charge. Additionally, the solution was assumed to be solely composed of water and the monovalent salt. Practically,

however, hybridization is done in a buffer solution that includes other molecules that are capable of maintaining the pH at a certain predetermined level. Finally, the PB model that is used neglects an important effect which is steric hindrance between the ions. This leads to the counter-ions being less capable of screening the DNA charge, which should allow the sensitivity of the BioFET to be higher than that in the basic model.

In this section, these simplifications are relaxed one at a time, and the effect of these simplifications on the sensitivity on the BioFET is determined by monitoring the effect of the simplification on the inversion charge underneath an isolated cylindrical DNA molecule, rather than simulating the entire BioFET. This is done because these effects require a finer mesh to be constructed around the DNA molecule, making simulation of the entire BioFET impractical for the available computers. The top-view dimensions of the simulation box were 80nm×80nm, enough to include several Debye lengths of the electrolyte. The semiconductor's depth was 500nm, and the depth of the electrolyte was 100nm. The insulator's thickness was 17.8nm, and 4nm for the cover layer.

The first effect to consider is the steric effect. The PB equation has the assumption of point-like particles with zero volume, allowing them to aggregate closely at a surface. As discussed in Chapter 2, this results in an overestimate of the adsorbed charge. The adsorbed charge is responsible for screening the DNA molecule's charge. Therefore, the volumetric exclusion of aggregated ions helps to relieve this screening ability and expose the DNA's charge to the semiconductor. Steric hindrance is a result of Pauli repulsion between close ions, and is not due to electrostatic forces. A mean-field model for the steric repulsion between ions is given by a modified PB equation [89] -[91] :

$$-\nabla \cdot (\epsilon \nabla V) = 2zqc_0 \frac{\sinh(z\beta V)}{1 + \phi_0 (1 + \cosh(z\beta V))}, \quad (3.21)$$

where the parameter $\phi_0 = 2c_0 a^3$, and a is the ionic radius. The ionic radii of Na⁺ ions and Cl⁻ ions are between 1-2 Å. However, a larger value is used in the following simulations to account for the attached surrounding water molecules. The modified PB equation admits a lower number of charges for the same potential as would the PB model. As the

radius of the ions tends to zero, the PB equation is restored. The modified PB equation offers a “natural” Stern layer at surfaces where ions aggregate, which includes the sidewalls of the DNA cylinder itself, but with a smoother and more realistic roll-off, rather than a brick-wall model. After the finite-element simulation is completed, the inversion charge (holes in a PMOS) is integrated within the semiconductor’s bulk, and the total charge density is taken as a measure of sensitivity:

$$Q = \int_{\Omega} p_0 e^{-\beta(V - V_B - \chi_M + \chi_{Si} + E_g/2 + \phi_F)} d\mathbf{r} . \quad (3.22)$$

Figure 3.13 shows the simulated inversion charge under a DNA molecule as a function of the electrolyte’s concentration, both with and without steric hindrance taken into consideration. The dashed lines correspond to the simulated charge with steric hindrance taken into account, whereas the solid lines ignore steric effects. The simulation was carried out for two bias points: weak inversion and deep inversion. It can be seen here that the steric exclusion indeed does cause the sensitivity of the BioFET to increase, as the dashed lines are always above the solid lines, irrespective of the applied bias or the electrolyte concentration.

The main trend of the curves in Figure 3.13 is the expected reduction of inversion charge with higher electrolyte concentration, whether steric effects are taken into consideration or not. However, what is important is the relative error in the inclusion of the steric exclusion. The inset of Figure 3.13 shows this relative error as a function of the electrolyte’s concentration. Firstly, the simulation shows that the relative error is independent of the applied bias. This is an unexpected result, since the bias can change the characteristics of the double layer within the DNA layer. Yet, it seems that if the device is maintained in inversion, the position of the inversion bias plays no role in the sensitivity change caused by steric exclusion. The second, and more important result, is that the relative increase in sensitivity by steric exclusion increases with higher electrolyte concentration. Around electrolyte saturation, steric exclusion contributes an equal amount of sensitivity as does the field-effect (as demonstrated by the 100% point in the inset). The absolute sensitivity, however, will be small at such high concentrations. Generally,

the electrochemical characterization of hybridized DNA is carried out after washing with a buffer salt of 1mM-10mM concentration [142]. Figure 3.13 shows that within this range, steric exclusion contributes around 20-25% of the total inversion charge. Thus, even at such low concentrations, ionic crowding does indeed cause a sensitivity increase and must be included in the model.

The simulation of Figure 3.13 was carried out for a single molecule that is far away from any neighboring DNA molecules. When two probe molecules are placed in close proximity, their screening countercharge clouds overlap. Steric effects in this case are even more pronounced, and higher sensitivity is expected due to volume exclusion in this case. However, it is important to notice that having closely spaced probes limits the diffusivity and hybridization of target DNA molecules, for the same reason of steric exclusion. This makes the sensor's response extremely slow and impractical.

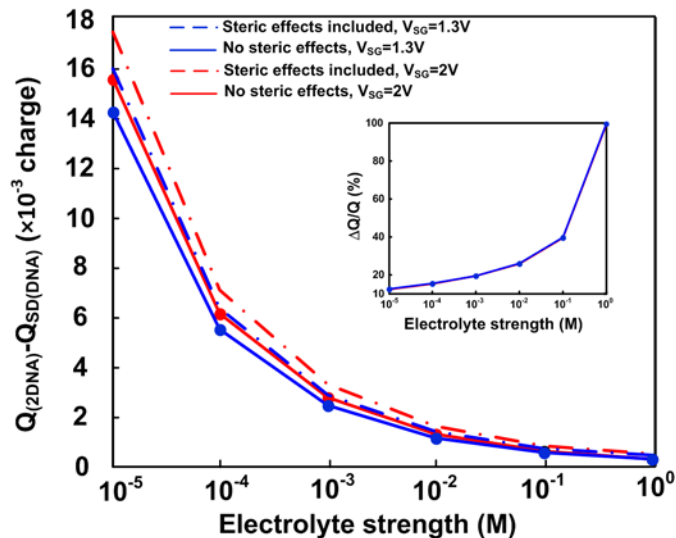


Figure 3.13 Simulated inversion charge under the DNA molecule at different electrolyte concentrations. (Inset: percentage relative error in simulation with and without steric effects, as a function of the electrolyte concentration)

In the previous models, the DNA was always assumed to be a charge-impermeable object. However, it might be noted that the doubling of the charge is not the only change that occurs when the DNA hybridizes. The conformation of the DNA

molecule changes (more in Chapter 5), and the charge distribution in its vicinity, also change. Even if the conformation were not to change, the single-stranded DNA is not impermeable to ions like the double stranded DNA. The next simulations attempt to examine the effect of ion exclusion during hybridization. This is done by making the DNA cylinder permeable to ions before hybridization. Thus, the PB equation is made valid inside the DNA cylinder as well. This, of course, is a simplified approach, since the bases can crowd the ions and make it less likely for the ions to diffuse as in a free PB solution. However, the model is still more realistic than that of the stiff DNA cylinder. After hybridization, the double-stranded DNA is considered impermeable to ions. This is due to the base stacking interactions of the base pairs, as well as the hydrogen bonding between complementary base pairs. The shared electrons create extended states often thought to conduct current [59]. These states create a Pauli repulsion field that excludes ions from the DNA molecule, although a finer detailed structure can show that ions might attach to the major and minor grooves of the DNA molecule.

Figure 3.14 shows the simulated inversion charge as a function of the electrolyte's concentration for a BioFET. The simulation is carried out once in weak inversion and once in deep inversion. It can be seen that there is a dramatic effect of increase in the sensitivity when the permeation effect is perfect (i.e. the DNA molecule is completely permeable to ions before hybridization and completely impermeable to ions after hybridization). This increase in sensitivity approaches 50% for electrolyte concentrations commonly used (around 1mM). This dramatic increase in sensitivity shows that the permeation effects of the DNA are extremely important and must be included in the model calculations. This effect is even more important than the steric exclusion of the counter-ions, and it provides incentive to further explore the effects of the geometry and characteristics of the DNA (Chapter 5).

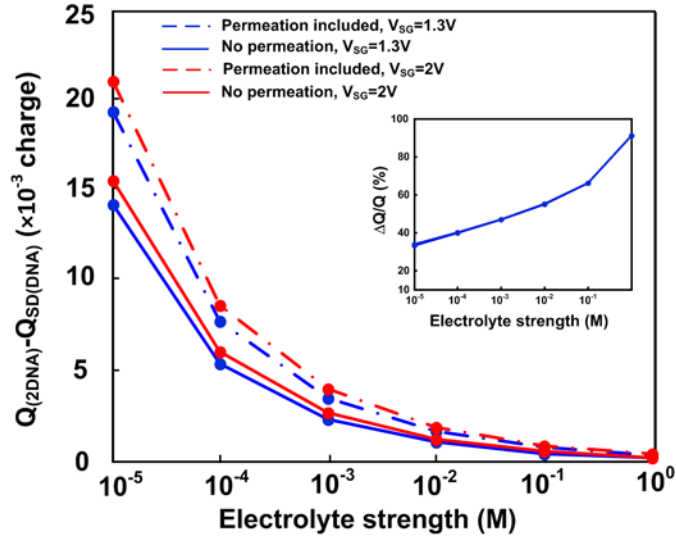
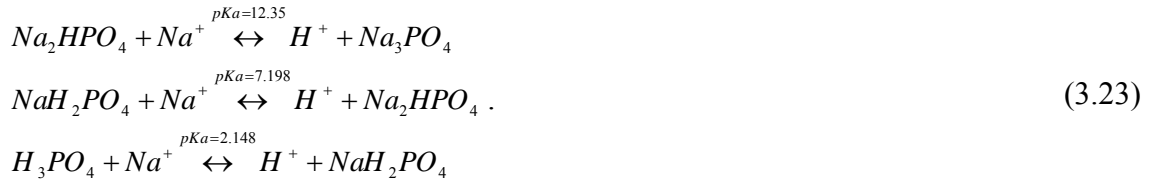


Figure 3.14 Inversion charge change upon hybridization as a function of the electrolyte concentration for two different biases. Each simulation is carried out twice, with and without a permeable DNA molecule. (Inset: percentage relative error in simulation with and without permeation, as a function of the electrolyte concentration)

One parameter that can have a dramatic effect on the performance of the biosensor, and which is often overlooked, is the buffer solution. Generally, an isotonic buffer is used such as **Phosphate Buffer Silane (PBS)**, to emulate cellular medium. The active ingredient for a NaCl buffer is sodium phosphate Na_3PO_4 . This compound can trap and release protons to regulate the pH of the solution. Each sodium ion can be exchanged with protons in the solution according to the following equations [143] :



The second equation is the relevant one since it maintains the solution's pH at around 7. Any excess protons would react with abundant Na_2HPO_4 molecules. If it is assumed that there exists an abundance of sodium cations, and if the dynamics of the chemical reaction are completely dictated by the proton reaction, then the pH of the solution is dependent on the pKa value (acid dissociation constant) of the reaction, the

initial pH of the solution before the buffer was added, and the initial buffer acid and base concentrations ($\text{NaH}_2\text{PO}_4/\text{Na}_2\text{HPO}_4$). One can now argue that the proton density at the insulator's surface is roughly unaffected by the local potential due to the double layer and DNA molecules, as the buffer will work to change that concentration to its equilibrium value. Since the buffer is uncharged, it is not affected by the double layer potential and charges either. Equation (3.3) must therefore be modified such that the proton density is no longer affected by the potential V , but instead the value is fixed by the chemistry of the buffer.

To calculate the pH of the buffer as a function of the pKa value of the buffer, we assume that the initial pH of the unbuffered solution is pH_0 , and that the initial concentration of the acid and the base are a_0 and b_0 , respectively. After equilibrium, the increase in the concentration of the protons is assumed to be x . Now, using the law of mass-action, we can write:

$$10^{-pKa} = \frac{[\text{Na}_2\text{HPO}_4][\text{H}^+]}{[\text{NaH}_2\text{PO}_4]} = \frac{(b_0 + x)(x + 10^{-pH_0})}{(a_0 - x)}. \quad (3.24)$$

After some algebra, the increase in the proton concentration is given by the solution of the following equation:

$$x^2 + (b_0 + 10^{-pH_0} + 10^{-pKa})x + (b_0 10^{-pH_0} - a_0 10^{-pKa}) = 0, \quad (3.25)$$

and the final pH of the solution is given by:

$$pH = -\log_{10}(x + 10^{-pH_0}). \quad (3.26)$$

Thus, not only is the sensitivity of the BioFET dependent on the nature of the electrolyte, but also on its composition (the concentrations of both acidic and basic components). Generally, when preparing buffers, only the acidic component is added to a high pH solution, and then HCl is used to calibrate the pH to the desired value. The following simulations use the mean value of pH achievable using different buffers [143].

Figure 3.15 shows simulation results of the inversion charge for different buffers in the pH range of 7. The results show significantly different sensitivities for buffers of

different pH values. However, when the buffering ability is switched on, a seemingly anomalous result is observed. The dashed lines in Figure 3.15 seem to show that the total inversion charge underneath the DNA molecule is *reduced* (although only slightly) after hybridization, rather than increased. Thus, it appears that the buffering function of the buffer solution has completely destroyed the ability of the BioFET to sense DNA hybridization.

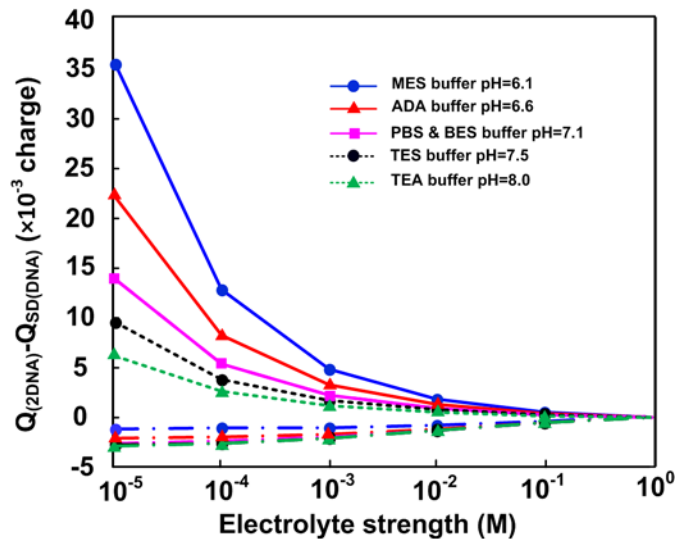


Figure 3.15 Hybridization inversion charge with several different buffers. Dashed lines are the results with ideal buffering capability, whereas solid lines neglect the buffer solution

To explain this destruction of sensitivity, we resort to Figure 3.16, showing the variation of the capacitance of the adsorption layer with the surface potential. It can be seen that at zero potential, higher pH values result in much more adsorbed negative charge. The surface potential of the p-type BioFET is negative. Hence, the proton concentration at the surface should be quite high (Equation (3.3)), controlling the negative charge density on the surface. However, with the buffering capability turned on, this excess proton concentration is immediately buffered to the equilibrium bulk value. Now, there is nothing that stops the insulator's surface from accumulating a large amount of negative charge. This negative charge is orders of magnitude higher than that of the DNA, and causes a "channel pinning" situation in the semiconductor. The negative charge in the insulator is so large that virtually all of the inversion charge in the channel is pinned at a

certain value and changes only slightly with the charge of the DNA, which is feeble in comparison with the adsorbed charge.

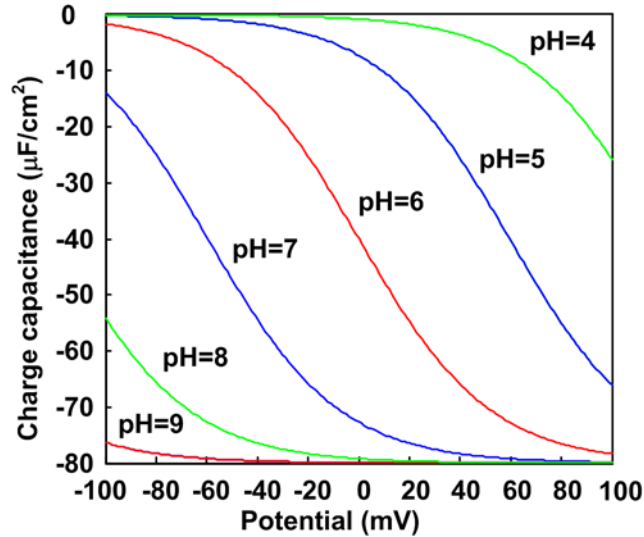


Figure 3.16 Charge-potential curves for proton adsorption on SiO_2 [4]









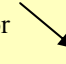








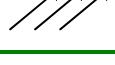
So far, experiments have not shown such severe changes of performance with different buffer solutions. An explanation for this is that with the availability of the hydrophobic SAM layer, the buffer's ability to diffuse and neutralize the protons adjacent to the surface might be limited, and the partition energy for the buffer might be a limiting factor in its potency in compromising the operation of the BioFET. With experimental data, this energy can be tweaked such that the dashed lines of Figure 3.15 are closer to the solid lines. Nevertheless, the purpose of this simulation was to assess the worst case effect of the buffering on the sensitivity of the BioFET, and it was shown that it does have the potential to kill the sensitivity of the BioFET with the right conditions.

3.7 Summary

This chapter introduced the 2-D and 3-D FEM models of the BioFET. The models were used to extract high-dimensional details that are critical to the proper design and operation of the BioFET, but that generally are not seen by simpler 1-D or primitive compact models commonly used in the literature. Table 3.1 shows how the 3-D model is superior to 1-D and 2-D modeling by showing the effects of different parameters on the

simulated sensitivity The model has also shown the importance of steric hindrance, pH and nature of the buffer solution used, and the permeability of the DNA molecule to ions. It is shown that some of these effects can severely enhance or compromise the sensitivity of the BioFET, and that all of these effects must be considered when fitting a physical model of the BioFET to experimental results.

Table 3.1 The change in simulated sensitivity as a function of different variables

<i>Variable</i>	<i>1-D</i>	<i>2-D</i>	<i>3-D</i>
Higher Electrolyte concentration			
pH increase	 or 	 or 	 or 
DNA density increase			
Bias closer to threshold			
Steric Effects included			

Chapter 4

IMPEDANCE MODEL FOR FET-BASED DNA SENSORS

4.1 Introduction

The previous chapter dealt with the static model of a BioFET while operating in amperometric mode. In this chapter, an impedimetric finite-element model for the BioFET is developed. This work is motivated in part by the history of electrochemical analysis techniques, which relied heavily on **Electrochemical Impedance Spectroscopy (EIS)** and **Cyclic Voltammetry (CV)**, and partly by the increasing number of publications that use impedance to detect successful hybridization of DNA molecules on several electrodes.

The chapter begins with a discussion of the sources of frequency response within the BioFET, and then moves onto the details of the small-signal model and the development of the constituent equations. Finally, the results of the simulations are presented.

4.2 Sources of Frequency Response

The DC behavior that was developed in the last chapter models a solution in equilibrium, and a semiconductor in steady-state current flow. That is, the charge density within the semiconductor and within the insulator is assumed independent of time. This, of course, is valid as time tends to infinity (settling time for the sensor), and given that all the bias potentials are constant DC values. Dynamic transient behavior is useful in characterizing the speed of the biosensor and its settling time. However, the dynamics of ion motion and

charging of the double layer are generally orders of magnitude faster than the hybridization kinetics, which eliminates the necessity to model them. On the other hand, the steady-state response of the sensor to a small sinusoidal input (after hybridization) has been extensively used [7] , [65] , [144] as a hybridization signal in many BioFET-like structures. To a first order, the steady-state response to an excitation frequency results in a sinusoidal output of the same frequency, but with a different amplitude and phase shift that are functions of the excitation frequency. This is generally written in the phasor representation:

$$V_{out}(\omega) = A(\omega)e^{j\phi(\omega)}, \quad (4.1)$$

for angular frequency ω , where $A(\omega)$ is the amplitude of the wave and $\phi(\omega)$ is the phase. For a BioFET, the impedance change is generally taken as a measure of hybridization. This is given by the ratio of the complex voltage and current:

$$Z(\omega) = \frac{V(\omega)}{I(\omega)} = A(\omega) + jB(\omega). \quad (4.2)$$

The real part of the impedance $A(\omega)$ is associated with resistive elements in the device, whereas the imaginary part $B(\omega)$ indicates the presence of reactive elements. The variation of the impedance with frequency (frequency response) is generally given by a Bode diagram of a Nyquist plot. The Nyquist plot is more common in electrochemistry and is the presentation used in EIS experiments. CV measurements can also be done but these are generally used to monitor large signal response for redox electrodes. In the case of the BioFET, no electron transfer reaction is expected due to the presence of the insulator, and the CV plot is of no added information when a small-signal bias is applied.

The general practice in electrochemistry is to fit the results of the EIS experiment with a circuit model that consists of discrete passive elements. These are generally resistors, capacitors, and Warburg (constant phase) elements. In a BioFET, the charge modulation due to hybridization happens within the double layer. In this layer, both resistive and reactive phenomena occur simultaneously in a distributed manner. This makes the discrete element approximation of electrochemistry not valid when probing the

effects of hybridization on the impedance behavior. A complete physical model is required to gain full insight into the dynamic operation of the sensor.

At first glance, the gate-body impedance of the BioFET might seem purely capacitive due to the presence of the insulator. However, the dynamics of the charges within the solution, as well as in the semiconductor, give a mixed reactive response that varies in a complicated manner with frequency. To properly model these effects, the dynamic equations of all the involved species must be included in the model. All charged species (cations, anions, electrons, and holes) respond in finite time, and a steady-state model is no longer applicable. Therefore, dynamic models of species transport must be employed. This is achieved using the matter continuity equations. Additionally, any chemical reactions that take place at surfaces or in the bulk of the solution have a time response and cannot be treated in the framework of equilibrium reaction constants, but rather require models from chemical kinetics. Moreover, the materials involved (semiconductor, insulator, and water) can be polarized either by electron cloud displacement, or molecular re-orientation. This has the effect of modulating the permittivity of the medium as a function of time. Finally, the time change of the electrical fields, brought on by the change in charge profiles, gives rise to interacting electromagnetic fields. Fortunately, some of these dynamics are faster than others, and some are of much lower significance that a rigorous treatment of all of these time responses is seldom necessary.

4.3 Model Details

A few assumptions are made to simplify the AC model. Firstly, almost all EIS measurements on DNA sensors are conducted in frequency ranges that do not exceed 1MHz [145] -[148] . At this frequency range, the complex permittivity of the different media can be neglected (Table 4.1 shows the complex permittivity of water at several frequencies). Additionally, at such low frequencies, electromagnetic radiation can also be neglected and the electric field is assumed to be irrotational. Convective flow and mixing are neglected as well in this AC model. Starting with the solution, the ions' kinetics are

generally modeled by the time-dependent Nernst-Planck (NP) equation [149] for cations with concentration c^+ and anions with concentration c^- :

$$\nabla \cdot \vec{J}_{c^\pm} = \mp q \nabla \cdot (D_{c^\pm} \nabla c^\pm \pm z_{c^\pm} \mu_{c^\pm} c^\pm \nabla V) = \mp q \frac{\partial c^\pm}{\partial t}, \quad (4.3)$$

where D_c is the diffusion coefficient of the ionic species, μ_c is the mobility, V is the potential, z is the ionic valence, and \vec{J} is the current flux. The drift term in Equation (4.3) is a source of nonlinearity in the model. Several approximations are made in the use of Equation (4.3). Firstly, steric effects on the mobilities of the ions are ignored. These have been shown to only apply at high applied voltages and under high current flow [150]. It is assumed that the dimensions of the FET are large with respect to the Debye length of the solution; since smaller channels have been shown to render the Nernst-Planck model inaccurate [151]. Equation (4.3) also neglects the possibility of ion generation or recombination since all electrolytes used are very strong and dissociate fully in water. Equation (4.3) relates the current's outward flux at any point due to both ions to the rate of change of that species at that point. It is generally solved self-consistently with Poisson's equation which takes care of ion-ion interactions.

In a manner very similar to the Poisson-Nernst-Planck equation, the dynamic equations for holes p and electrons n are also defined by continuity equations:

$$\nabla \cdot \vec{J}_{p,n} = \mp q \nabla \cdot (D_{p,n} \nabla (p,n) \pm \mu_{p,n} (p,n) \nabla V) = \mp q \frac{\partial (p,n)}{\partial t}. \quad (4.4)$$

In Equation (4.4), both the generation and recombination currents were neglected for simplification of the model. The insulator is assumed to have no mobile charge carriers and thus does not require any continuity equation modeling, and the dynamics of trapping and de-trapping of charges at interface states of the semiconductor/insulator surface are assumed to be very fast in comparison with the operating frequency of interest.

Table 4.1 Permittivity of water at various frequencies [143]

<i>Frequency</i>	<i>0°C</i>		<i>25°C</i>		<i>50°C</i>	
	ϵ'	ϵ''	ϵ'	ϵ''	ϵ'	ϵ''
0	87.90	0.00	78.36	0.00	69.88	0.00
1kHz	87.90	0.00	78.36	0.00	69.88	0.00
1MHz	87.90	0.01	78.36	0.00	69.88	0.00
10MHz	87.90	0.09	78.36	0.04	69.88	0.02
100MHz	87.89	0.91	78.36	0.38	69.88	0.20
200MHz	87.86	1.82	78.35	0.76	69.88	0.39
500MHz	87.65	4.55	78.31	1.90	69.87	0.98
1GHz	86.90	9.01	78.16	3.79	69.82	1.96
2GHz	84.04	17.39	77.58	7.52	69.65	3.92
3GHz	79.69	24.64	76.62	11.13	69.36	5.85
4GHz	74.36	30.49	75.33	14.58	68.95	7.75
5GHz	68.54	34.88	73.73	17.81	68.45	9.62
10GHz	42.52	40.88	62.81	29.93	64.49	18.05
20GHz	19.56	30.78	40.37	36.55	52.57	28.99
30GHz	12.50	22.64	26.53	33.25	40.57	32.74
40GHz	9.67	17.62	18.95	28.58	31.17	32.43
50GHz	8.28	14.34	14.64	24.53	24.42	30.47

The total current is expected to be continuous across all boundaries. Figure 4.1 shows the different current contributions in the different parts of the BioFET. In the electrolyte, both displacement and ionic currents exist. The displacement current occurs due to the change in the local electric field of the double layer as a function of time. The same situation applies in the semiconductor, with both displacement current and carrier current. Within the insulator, only displacement current exists due to the lack of any mobile charges. Across the interfaces, the total current has to be conserved. If the dynamics of the trap charging at the insulator/semiconductor interface are neglected, then the normal carrier conduction current has to vanish at this interface. At the electrolyte/insulator interface, the total current is continuous as well. However, the conduction current need not vanish at the interface, as the ions can get adsorbed onto the sites at the interface. The proper boundary condition for the flux of cations and anions

would require equating the ionic flux into the interface with the rate of change of the surface charge densities at the interface:

$$q \left(D_{c^\pm} \nabla c^\pm \pm z_{c^\pm} \mu_{c^\pm} c^\pm \nabla V \right) = \frac{-\partial \sigma^\pm}{\partial t}, \quad (4.5)$$

where the variables σ^+ and σ^- are the positively charged and negatively charged surface charge densities, respectively. If one of the ions is not amenable to adsorption, then reflecting boundary conditions must be applied to that species, which is achieved by annihilating the right hand side of Equation (4.5).

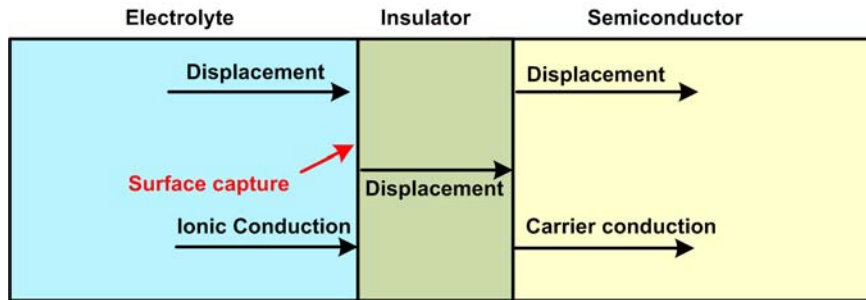


Figure 4.1 Different current components across the BioFET key interfaces [149]

At the electrolyte-insulator's surface, the chemical adsorptions discussed in Chapter 2 have a transient response which can coincide with the frequency of measurement. Hence, these transients must be included in the model.

Equation (4.5) depends on the charging rate of the insulator's surface, and these charges are no longer related to the potential by Equations (3.3), (3.6), and (3.7), since the interface now is in non-equilibrium. Thus, the surface charges become extra degrees of freedom that must be solved together with the potential and charge density variables in the electrolyte and semiconductor. This makes the impedance problem a hybrid 2-D/3-D problem.

The adsorbed charges on the insulator are generally not in equilibrium, and equilibrium constants cannot be used. Rather, a kinetic theory for the adsorption reaction must be used. If a first-order reaction is assumed, then the rates of cationic and anionic charging are given by Arrhenius's equation:

$$\begin{aligned}\frac{\partial \sigma^+}{\partial t} &= K_a^+ e^{-\frac{E_a^+}{kT}} a_{H^+} (\sigma_s - \sigma^+ - \sigma^-) - K_r^+ e^{-\frac{E_r^+}{kT}} \sigma^+ \\ \frac{\partial \sigma^-}{\partial t} &= K_a^- e^{-\frac{E_a^-}{kT}} (\sigma_s - \sigma^+ - \sigma^-) - K_r^- e^{-\frac{E_r^-}{kT}} a_{H^+} \sigma^-\end{aligned}\quad (4.6)$$

where K_a , K_r , E_a , and E_r are the activation pre-exponential factors and activation energies for the adsorption and desorption processes, respectively, and σ_s is the total surface site density. The surface activity of hydrogen ions a_{H^+} is given by Equation (3.3). It is noted here that the kinetics of proton diffusion is neglected, and protons in the solution are assumed to be in equilibrium. This is justifiable since the mobility of protons in water is much higher than that of other ions [152] ,[153] .

The activation energies are understood from the reaction diagram of Figure 4.2. According to Arrhenius's model, the reaction rate depends on the activation energy, which is the energy required for the reactants to reach the "activated" state, and be ready to roll onto the products. In the absence of catalysts, the activated complex is unstable and generally has a higher free energy than the reactants or the products, such that the reaction is not spontaneous. Furthermore, the energy levels of the reactants and the products are generally not constant but depend on the concentrations of the species, attaining equilibrium when the energy levels are at the same height in the reaction diagram. Thus, to properly describe the kinetic model, both forward and reverse reaction rates must be known. This requires knowledge of the pre-exponential factor, as well as the energy barrier. In this model, it is assumed that this data is available, or can be fitted with sufficient experimental data.

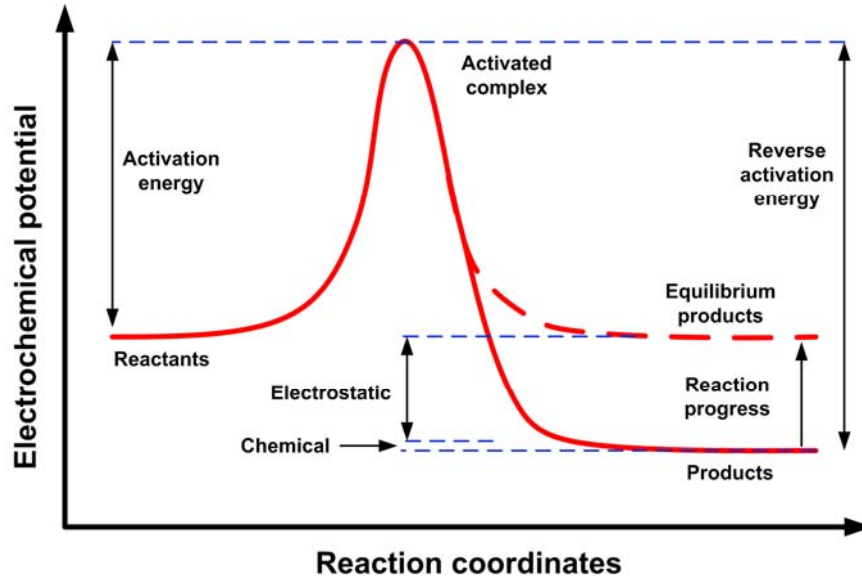


Figure 4.2 A sample reaction energy diagram. The forward and reverse reaction energies are only the same for a completely reversible reaction in equilibrium

The presence of the time-dependent surface charge on the insulator's surface has its effects on the boundary conditions of the electrostatic potential. The new boundary condition requires the discontinuity in the flux density across this interface to be equal to the total charge adsorbed onto the surface:

$$\epsilon_{ins} \nabla V_{ins} - \epsilon_{Si} \nabla V_{Si} = \sigma^+ - \sigma^- . \quad (4.7)$$

The complete, time dependent solution of the AC model requires solving Equations (4.3)-(4.7) self consistently to determine the electrostatic potential, cation and anion charge densities, electrons and holes concentrations, and adsorbed charge densities as functions of time and space. This requires a finite-element discretization of space, in addition to an Euler time-stepping mechanism for time integration. The starting point for integration would be the DC solution (obtained by solving the system and setting all time derivatives to zero, which reduces to the equations of Chapter 3).

To study the impedance characteristics, it is not necessary to solve the time-dependent system. Since the steady-state sinusoidal response contains all the information about the impedance, it is sufficient to perform a frequency response analysis on the

system of equations. This is accomplished by isolating the DC and AC responses, applying the Fourier transform on the AC set of equations, and annihilating nonlinear terms with the assumption of small-signal stimuli. This results in a FEM model in complex variables, representing the magnitudes and phases of the potential and charge densities as functions of frequency. To start, the total solution variables X are expressed as DC terms X_{DC} and AC terms \tilde{x} :

$$\begin{aligned}
 V &= V_{DC} + \tilde{v} \\
 p &= p_{DC} + \tilde{p}, V_{qfp} = V_{qfp,DC} + \tilde{v}_{qfp} \\
 n &= n_{DC} + \tilde{n}, V_{qfn} = V_{qfn,DC} + \tilde{v}_{qfn} \\
 c^\pm &= c_{DC}^\pm + \tilde{c}^\pm, V_{qfc^\pm} = V_{qfc^\pm,DC} + \tilde{v}_{qfc^\pm}
 \end{aligned} \tag{4.8}$$

where the ions of the solution now require to be expressed by their quasi-Fermi levels, since they are in nonequilibrium. The quasi-Fermi levels are related to the charge densities by the following equations:

$$\begin{aligned}
 (p, n) &= c_0 e^{\mp \beta (V - (V_{qfp, qfn}) + \chi_{st} + E_g / 2)} \\
 c^\pm &= c_0 e^{\mp z_{c^\pm} \beta (V - V_{qfc^\pm} + \chi_{sol} + E_{ref})}
 \end{aligned} \tag{4.9}$$

Inserting these expressions into the original, time dependent equations, cancelling the DC terms out, and applying the Fourier transform, the linearized impedance equations for the bulk electrolyte is given by:

$$\begin{aligned}
 -\varepsilon_{sol} \nabla^2 \tilde{v} &= q (z_{c^+} \tilde{c}^+ - z_{c^-} \tilde{c}^-) \\
 \nabla \cdot \left(q \mu_{c^+} (z_{c^+}^2 - z_{c^+}) (\tilde{c}^+ \nabla V_{DC} + c_{DC}^+ \nabla \tilde{v}) - q \mu_{c^+} z_{c^+}^2 (\tilde{c}^+ \nabla V_{qfc^+, DC} + c_{DC}^+ \nabla \tilde{v}_{qfc^+}) \right) + i \omega q z_{c^+} \tilde{c}^+ &= 0, \\
 \nabla \cdot \left(q \mu_{c^-} (z_{c^-}^2 - z_{c^-}) (\tilde{c}^- \nabla V_{DC} + c_{DC}^- \nabla \tilde{v}) - q \mu_{c^-} z_{c^-}^2 (\tilde{c}^- \nabla V_{qfc^-, DC} + c_{DC}^- \nabla \tilde{v}_{qfc^-}) \right) - i \omega q z_{c^-} \tilde{c}^- &= 0
 \end{aligned} \tag{4.10}$$

where the variable ω is the radial frequency of the stimulus signal. The first equation is the AC equation for Poisson's equation (neglecting radiating effects), whereas the second and third equations are the AC equations for the charge transport. It should be noted that the small-signal model does depend on the DC operating point and its gradient, even though the actual terms describing the DC solution were omitted. It is therefore assumed that this AC model is implemented on top of the DC model (Chapter 3), and using the exact same mesh and geometry that was used for the DC solution.

In a similar fashion, the AC model for the bulk semiconductor is given by the following complex-valued equations:

$$\begin{aligned} -\varepsilon_{si} \nabla^2 \tilde{v} &= q(\tilde{p} - \tilde{n}) \\ \nabla \cdot \left(-q \mu_{p,n} \left(\nabla \tilde{v}_{afp,afn} \pm \beta \nabla V_{afp,DC,afn,DC} (\tilde{v}_{afp,afn} - \tilde{v}) \right) \right) + i \omega q \beta (\tilde{v}_{afp,afn} - \tilde{v}) &= 0 \end{aligned} \quad (4.11)$$

Also, since the insulator's charge is time dependent, it would have to have a frequency response as well. By separating the DC and AC components of the surface charge density (as was done for all other degrees of freedom in Equation (4.8)), the impedance model for the site-binding theory is given by:

$$\begin{aligned} i \omega \tilde{\sigma}^+ &= K_a^+ e^{\frac{E_a^+}{kT}} \left(-\beta a_{H^+} \tilde{v} (\sigma_s - \sigma^+ - \sigma^-) - a_{H^+} (\tilde{\sigma}^+ + \tilde{\sigma}^-) \right) - K_r^+ e^{\frac{E_r^+}{kT}} \tilde{\sigma}^+ \\ i \omega \tilde{\sigma}^- &= -K_a^- e^{\frac{E_a^-}{kT}} (\tilde{\sigma}^+ + \tilde{\sigma}^-) - K_r^- e^{\frac{E_r^-}{kT}} \left(-\beta a_{H^+} \tilde{v} \sigma^- + a_{H^+} \tilde{\sigma}^- \right) \end{aligned} \quad (4.12)$$

and the corresponding boundary conditions for the ion charge densities and the electrostatic potential are given by:

$$q \left(\mu_{c^\pm} \nabla \tilde{c}^\pm \pm z_{c^\pm} \beta \mu_{c^\pm} (\tilde{c}^\pm \nabla V + c^\pm \nabla \tilde{v}) \right) = -i \omega \beta \tilde{\sigma}^\pm \quad (4.13)$$

and

$$\varepsilon_{ins} \nabla \tilde{v}_{ins} - \varepsilon_{Si} \nabla \tilde{v}_{Si} = \tilde{\sigma}^+ - \tilde{\sigma}^-, \quad (4.14)$$

respectively. Equations (4.9)-(4.14), together with the DC equations of Chapter 3, thus provide a complete AC impedance model for the BioFET. Using Dirichlet boundary conditions on the source, drain, reference electrode, or body contacts can allow determination of several different impedance responses. For example, it is generally desired in impedance studies to assess the solution/source or solution/drain capacitance through the covering PDMS layer. This is done to monitor the quality of the post-processing of the FET, as well as to determine parasitic impedances (the quantities referred to as C_{CLCS} and C_{CLD} in [154]). To use the AC model to determine this capacitance, the FET would have to operate in accumulation, so as not to include the channel gate capacitance. A deep-accumulation bias is applied to the reference electrode, superimposed on a small (around 10mV) AC sinusoidal signal. This appears as a Dirichlet

boundary condition for the electrostatic potential at the boundary of interest (reference electrode in this example). The AC current flow due to this applied potential is evaluated by integrating the current density along the boundary of interest (source terminal in this example). Leakage currents can also be evaluated by integrating the current density along the other terminals.

In this model, the reference electrode was not included. This is due to the fact that most BioFET sensors to date use macroscopic reference electrodes. As such, the impedance of these electrodes is very small with respect to the impedance of the BioFET across a large range of frequencies. In addition, modeling a large reference electrode would require a significant increase in the mesh size, and much higher computational bandwidth with a very small added value. However, as microfabricated reference electrodes start to be integrated with the BioFET, their impedances will have to be revisited from physical modeling. This is because the kinetics of the specific reaction can severely change with the micro-structure of the reference electrode. This is especially true for dissolving electrodes such as Ag/AgCl, which is the most commonly used electrode for these applications. The electrode modeling can be complicated by the need to model the reaction kinetics as well as the diffusion of ions for a complicated geometry.

4.4 Simulation Results

Since the most commonly used methods of impedance detection in published experiments are CV or EIS diagrams, these will be the focus of the simulation results in this section. The CV diagram of a BioFET is expected to be very similar to that of a conventional FET, since the essential charge-potential profile is not changed in the underlying FET. To plot the CV diagram, the applied AC voltage V and the resulting current I must be evaluated for a large range of reference electrode applied potentials with no DC currents between the source and drain. The capacitance of the FET structure is responsible for the reactive part of the impedance. Thus, the capacitance is calculated as:

$$C = \left(\frac{\tilde{v} \omega}{\text{imag}(\tilde{i})} \right)^{-1} . \quad 4.15$$

The BioFET is expected to maintain the CV diagram of a normal FET. This is shown in the simulation results of Figure 4.3. These simulations were carried out at frequency of 1 kHz, since extremely high frequencies result in inhibition of the reactive response due to inertial effects in the carriers. The depletion region's reduction of the capacitance is clearly seen. One could isolate the capacitance contributions from the body or from the contacts by integrating the current along the boundaries of interest. It can be seen that in accumulation (more positive reference electrode bias), the capacitance contribution from the body of the semiconductor is the largest, whereas the contacts only give residual capacitance due to small overlap with the solution. In inversion, the body capacitance diminishes since the channel is set up, and most of the current goes through the source and drain contacts. This AC simulation can therefore be used to predict the overlap and parasitic capacitances after post-processing and PDMS treatment. These parasitic capacitances can have detrimental effects on the functionality of impedance-based biosensors, since these conductive paths are parallel to the sensitive layer of the sensor as shown in Figure 4.4. Therefore, their values must be clear before fabrication, and this AC model can accurately calculate these capacitances for different geometries. The calculations becomes more important with smaller-sized sensors, such as nanowire sensors, since the overlap capacitances are now of the same orders of magnitudes as the active area capacitance of the biosensor.

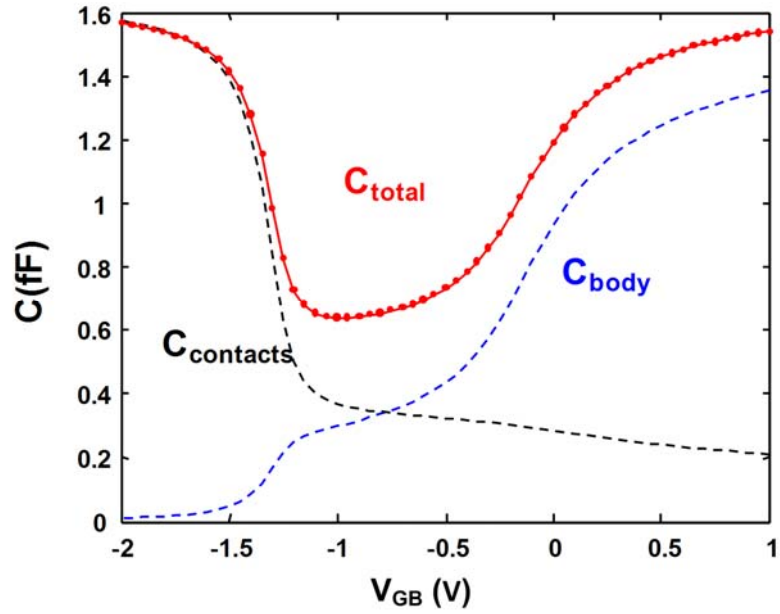


Figure 4.3 Simulated CV diagram of the FET, with the body and contacts capacitances separately shown

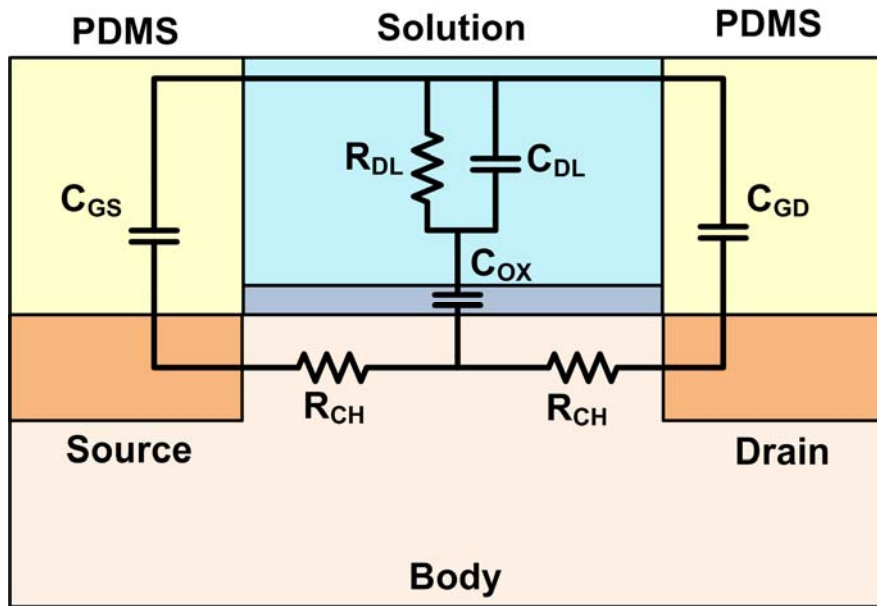


Figure 4.4 Capacitances in a FET structure

Upon introduction of the electrolyte and probe DNA immobilization, a shift in the threshold voltage is noticed. This is generally seen as a shift in the CV diagram of the FET. Figure 4.5 shows simulation results of the CV diagram of a BioFET, in comparison

with that of a regular FET with the same dimensions and composition. It can be seen that the BioFET's CV curve indeed has shifted to the right, lowering the amount of negative reference electrode bias needed to invert the channel. However, the minimum capacitance also seems larger than that of the FET in depletion, whereas in deep accumulation and inversion, the BioFET capacitance is smaller than the capacitance of the FET. This is expected since the double layer introduces a series capacitance that would reduce the overall capacitance of the structure. These fine details are necessary when characterizing the post-processing steps and monitoring the threshold shift. The threshold of the BioFET and its capacitance before hybridization must be known to a high precision; otherwise the measurements can be erroneous.

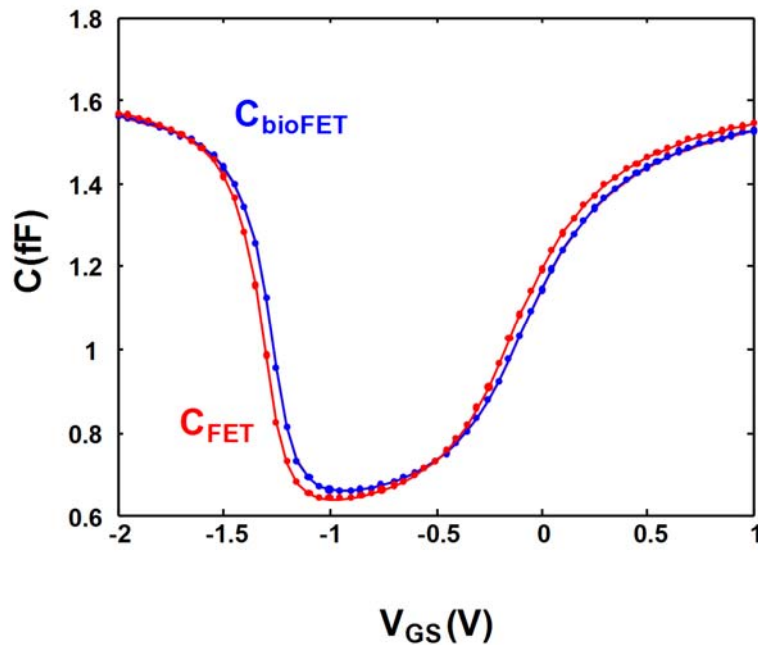


Figure 4.5 Comparison of the CV diagram of a regular FET and a BioFET, showing the shift due to the presence of DNA molecules and the electrolyte solution

The signal sought in impedance sensors is the change in the capacitance due to hybridization. Once again, it is assumed here that complete hybridization takes place, with doubling of the charge on the DNA cylinder. Figure 4.6 shows a diagram of the relative differential capacitance as a function of the applied voltage. It is seen that there exist two peaks of high sensitivity: the onset of accumulation and the onset of inversion,

with the change in inversion being the largest, at around 1%. It has been previously shown that this region is also the chosen bias point for optimum SNR [71]. Thus, whether operating as an amperometric sensor or an impedimetric sensor, one must operate the BioFET at threshold voltage for optimum SNR.

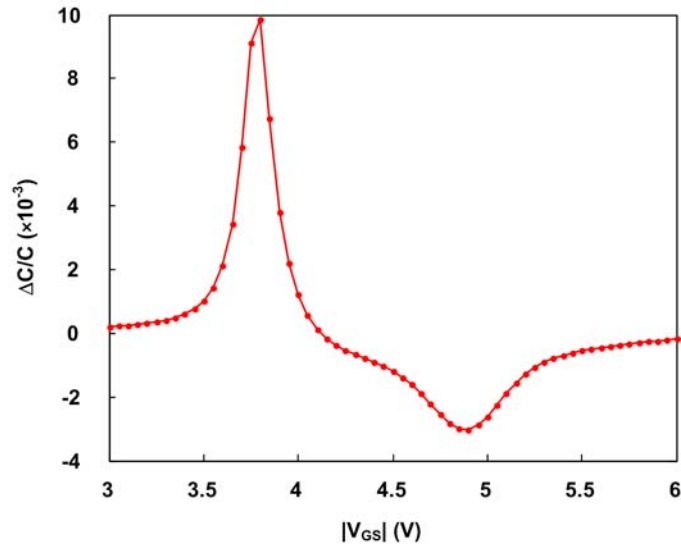


Figure 4.6 Differential capacitance change due to hybridization as a function of the gate bias, showing that the onset of inversion and accumulation result in the maximum sensitivity

In electrochemistry, the change in the entire impedance, and not just in the reactive part, is commonly presented. Nyquist diagrams (also known as EIS diagrams) are used to show the variation of the real and reactive parts of the impedance with frequency. Here, Nyquist diagrams are used to show the variation of the impedance with hybridization at different frequencies. In RC series-like circuits, instead of plotting the impedance diagram, the admittance is plotted. It is still known as an EIS diagram, but using the admittance allows for easier extraction of equivalent circuit parameters. Impedance Nyquist plots are generally used for RC parallel-like circuits. Figure 4.7 shows the simulated EIS diagrams for the admittance of the BioFET. The diagrams are drawn for a frequency sweep of 1Hz-1MHz for each curve, and with a sweep of reference electrode bias from deep accumulation to deep inversion. For any given frequency, the real admittance follows the reactive admittance in its change. The admittance is highest in deep accumulation and inversion, and has its lowest values in depletion. This was already

seen in the CV diagram. However, the Nyquist diagram goes further into giving details of the conductive change, and not just the reactive. This is important in the design of oscillator-based sensors, since the oscillation frequency is very dependent on the total impedance of the sensitive element, and not just on the reactive part.

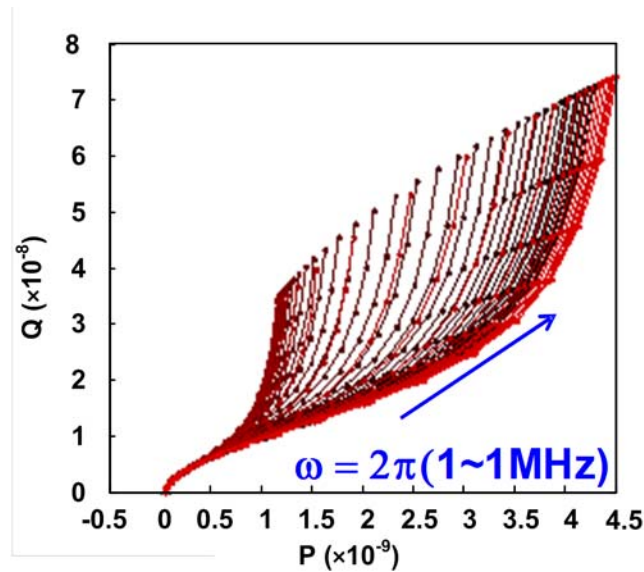


Figure 4.7 Electrochemical admittance diagram for the BioFET. The sweep is from deep accumulation to deep inversion

Figure 4.8 shows the Nyquist plot of the relative change in the admittance of the BioFET upon hybridization for a lightly packed DNA monolayer (around 15%). The simulation was carried out at threshold bias to optimize the sensitivity. The result shows the interesting result that the optimum relative change in the reactance is about an order of magnitude greater than that of the susceptance. Furthermore, these two extrema do not occur at the same frequency. For reactive AC sensing, lower frequencies ($\sim 100\text{Hz}$) are favored for mainstream CMOS, whereas for conductive sensing, the optimum frequency range is around 1-2MHz.

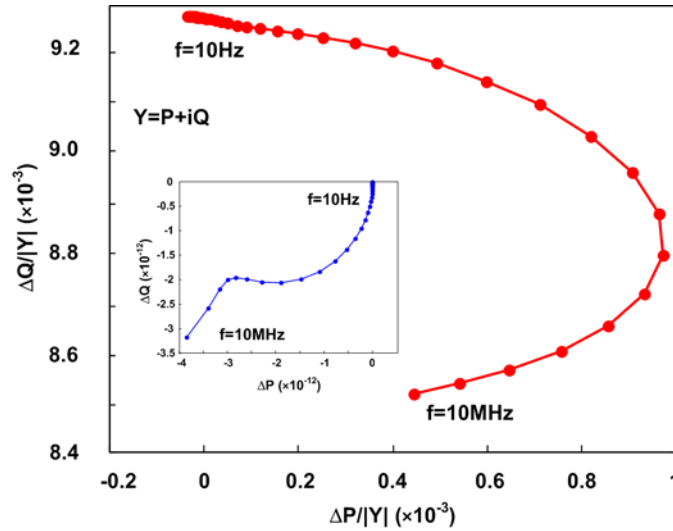


Figure 4.8 Nyquist plot for the relative change in the admittance of the BioFET upon hybridization in inversion. (Inset: absolute change in admittance in accumulation)

The AC model allows extraction of some interesting fine details about the charge distribution in the DNA layer and their influence on the total charge transport in the device. Figure 4.9 shows simulated Nyquist plots of the absolute change in the admittance of a BioFET for several bias voltages in inversion. It can be seen that the change in the real conductance at strong inversion is negative. This seems counter-intuitive since the simulations are done on a PMOS device and the DNA charge is negative, which means that successful hybridization should increase the hole charge in the channel by the Field-Effect. A closer examination of the structure, however, reveals that the distribution of charges between the DNA, the solution's ions, and the underlying semiconductor, is what dictates the sensitivity of the DNA. In moderate inversion, the Debye layer adjacent to the DNA walls is diffuse enough that hybridization of DNA molecules will not have a significant effect on the ionic density at that layer. However, in deep inversion, the hybridization can cause more counter-charge to be close to the DNA wall, limiting the number of vertical conductive paths through the solution. Therefore, even though there might be more holes in the semiconductor's channel due to hybridization, the total AC current is lower because of the redistribution of ionic charges in the DNA layer, which significantly increases the resistance of that layer and reduces the overall real admittance.

The result of Figure 4.9 also can be used to make a useful design guideline. As mentioned, in oscillator-based sensors, it is desired to solely change the reactive part of the admittance upon hybridization. Looking at Figure 4.9, it can be seen that the optimum bias point is not necessarily that which results in the maximum capacitive change, but that which would maintain a minimum read admittance change (keeps the Nyquist plot of the admittance change vertical). This would not give the best sensitivity but would ensure a reliable operation of the BioFET oscillator-sensor.

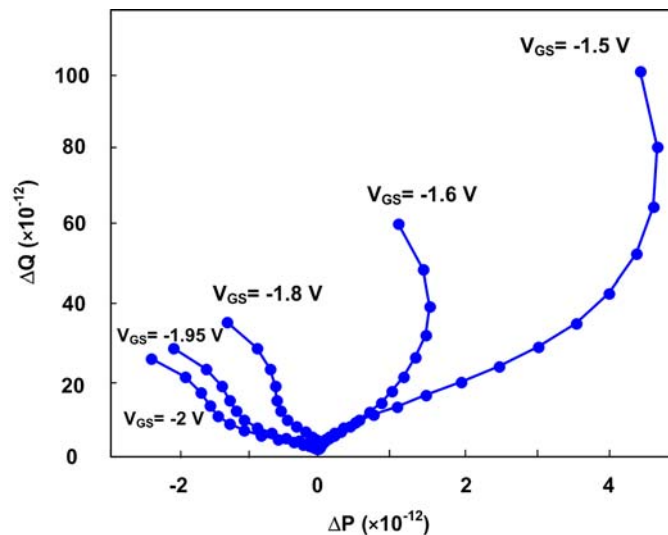


Figure 4.9 Absolute change in the admittance of the BioFET in inversion. The anomalous negative change in admittance in deep inversion are clearly seen

4.5 Other Effects

4.5.1 Electrolyte Concentration

In previous DC simulations [4], it was shown that the concentration of the solution significantly affects the sensitivity. Lower electrolyte concentrations were preferred over saturated solutions since dilute electrolytes were less capable of shielding the DNA's charge. However, when AC analysis is conducted, the situation can be more complicated. Higher electrolyte concentrations do indeed shield the DNA charges more efficiently. However, a higher electrolyte concentration also means lower solution impedance. This

has the potential to enhance the impedance change upon hybridization. Additionally, higher electrolyte concentrations imply a smaller Debye length and a larger capacitance. Thus, it is plausible that the high electrolyte concentration might allow higher sensitivity when performing AC detection. However, depending on the values of the different physical parameters, such speculations must be put to the test via simulations.

Figure 4.10 shows the Nyquist diagram of the sensitivity of the BioFET for different electrolyte concentrations. The simulations were carried out under threshold bias. As can be seen from the results, the trends of the EIS diagrams change dramatically with the electrolyte concentration, and different concentrations show different sensitivities at different frequencies. For the higher frequency range (100kHz-10MHz), it is seen from the figure that the lower concentrations (10 μ M-1mM) give a curve that is concave upwards, whereas the higher concentrations give a profile that is concave downwards. This indicates that at low concentrations, the ratio of the reactive sensitivity to the real sensitivity decreases with frequency increase, whereas the converse is true for higher electrolyte concentration. At any point on these curves, this ratio can be calculated from the slope of the curve. Larger slopes mean more reactive sensitivity, whereas smaller slopes indicate dominance of the real conductance.

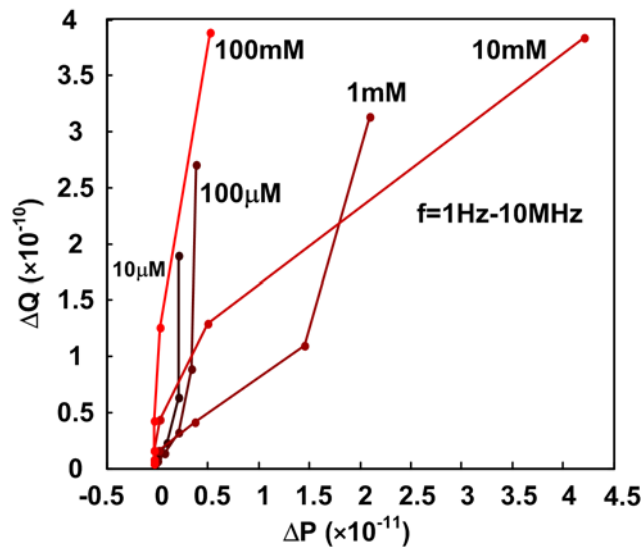


Figure 4.10 Nyquist diagram of the admittance change due to hybridization of DNA, for different electrolyte concentrations

Figure 4.10 also affirms our earlier expectation that the change of sensitivity with electrolyte concentration would not necessarily be monotonic. There are several crossings of the admittance curves that indicate changes in the real and reactive sensitivities. Looking at Figure 4.10, we can see that the reactive sensitivity is generally larger with higher electrolyte concentration, unlike DC sensors where the sensitivity is reduced with electrolyte concentration increase. It is also noticed that at moderate concentrations (1mM-10mM), the real change in impedance is large. This behavior can be traced back to the Debye length. At these moderate concentrations, the Debye length is of the same order as the length of the oligonucleotide, making the increase in the mobile counter-charge large when the DNA has hybridized. At higher electrolyte concentration, the Debye length is short enough that the DNA hybridization does not significantly change the resistive path. On the other hand, at low concentrations, the Debye length is too large, and the DNA hybridization has a small and local effect on the charge profile. This diminishes the real impedance change upon hybridization. From the previous discussion, it would seem that for oscillator-based DNA sensors, we should operate the device using high electrolyte concentration. This allows us to eliminate the flushing step to remove the saturated hybridization buffer and replace it with a low strength buffer. Using impedance detection, higher electrolyte concentrations lead to a larger reactive sensitivity and lower real sensitivity. This even holds at low frequencies, as shown in Figure 4.11.

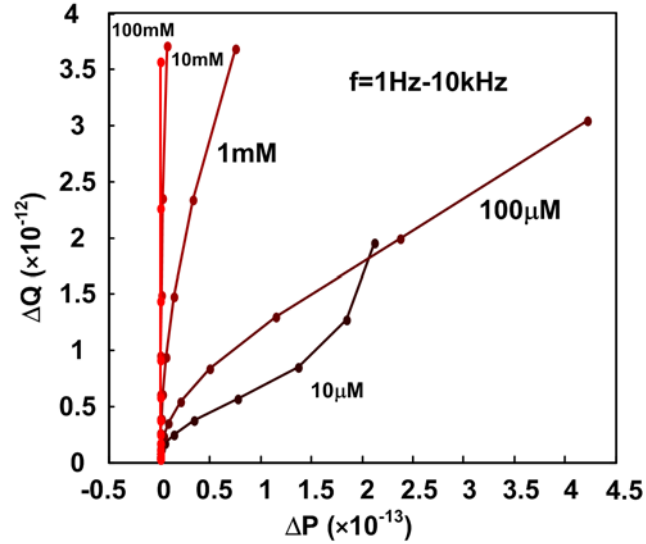


Figure 4.11 Nyquist diagram of the admittance change in a BioFET for low frequencies

4.5.2 Drain Bias

Often, the AC measurements are not done under zero DC drain current. This is done to utilize the intrinsic transconductance of the BioFET to try and enhance the sensitivity of the BioFET. In this case, the transistor's source, drain, and body are not connected together, and the device cannot be characterized by a single impedance. Instead, the relationships between different voltage biases and currents give rise to different equivalent circuit elements. Although we do not attempt or encourage the use of lumped elements since the complete physics of the device must be captured, we do use one lumped circuit parameter to measure the sensitivity. This is the transconductance g_m defined as:

$$g_m = \frac{\partial I_D}{\partial V_{GS}}. \quad (4.16)$$

In a lumped circuit element, this parameter is defined as a voltage-dependent current source, and generally has a real and positive value. Any phase relationships between the gate voltage and the drain currents are fitted using reactive and resistive elements within the current path. Since our model is physics-based, all of these reactive effects will automatically be calculated. Thus, the relationship between the real and

imaginary parts of the transconductance carries in it information about the equivalent circuit elements.

Figure 4.12 shows simulated Nyquist plots for the transconductance change of the BioFET upon DNA hybridization at different drain biases. As expected, hybridization will cause the channel to be more inverted, and the real part of the transconductance will be positive and will increase until it almost saturates at a maximum value (around 140nS in Figure 4.12). However, the AC model also shows how the reactive part of the transconductance changes. The frequency sweep in Figure 4.12 is from 1Hz-10MHz in logarithmic steps. For frequency ranges upto 1MHz, and irrespective of the drain bias, the real part of the transconductance does not seem to change, but the absolute value of the reactive change rapidly increases. There also appears to be a maximum reactive change at a frequency of around 3MHz, which is also independent on the drain bias. As the reactive change approaches a maximum, it is noticed that the real change starts to slightly degrade. This can be identified as the onset of resistive dominance in the electrolyte. The semiconductor's carriers can respond to much higher frequencies, but the ions in the solution are slower to respond. This causes a significant portion of the applied AC voltage to appear across the electrolyte's bulk. The degradation in real transconductance will then be dependent on the distance between the reference electrode and the sensitive surface of the electrolyte [155] . This leads to a penalty when using impedance measurements to detect DNA hybridization: the depth of the electrolyte and its composition is much more important due to kinetic effects of the solution, as compared with the equilibrium case in DC measurements.

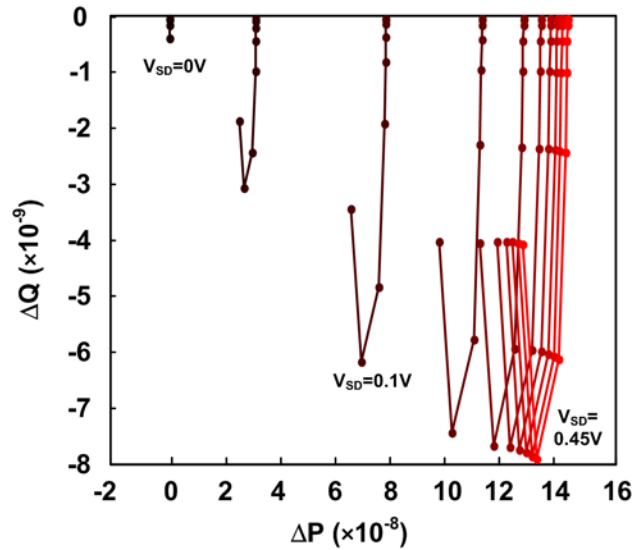


Figure 4.12 Nyquist plot of the change in the transconductance of the BioFET

Another result obtained from Figure 4.12 is that the real change in the transconductance is almost an order of magnitude larger than the reactive change. This is in contrast with the situation in the previous figures (with the BioFET used as a capacitor). This is traced to the inherent amplification capability of the saturated BioFET. The enhancement in both real and reactive sensitivities is a few orders of magnitude over the passive capacitive structure. Thus, a good impedance sensor will always utilize the BioFET in saturation and monitor the change in the transconductance (both real and reactive) as a measure of hybridization.

A final point to make about Figure 4.12 is that it appears that the sensitivity reaches a maximum as the drain bias is increased, and does not go beyond this point. This occurs despite the fact that the drain bias in a normal FET would enhance the transconductance (Figure 3.7, and neglecting higher order effects). In this case, the saturation of sensitivity is due to the desensitization of the drain region to the DNA charges. Here, the increased drain bias effect on sensitivity and the channel length modulation are in contention. This leads to saturation in the real and reactive sensitivity.

4.5.3 Steric Effects

In Chapter 3, it was shown how steric effects can significantly influence the sensitivity of the BioFET. Here, it is desired to see if a similar effect holds when sensing using the impedance change of the BioFET. Firstly, the steric model of Chapter 3 only applied in equilibrium. The solution in the case of AC measurements is not in equilibrium. Thus, a mean-field kinetic model is required that accounts for steric effects. One such model is derived by Kilic et al [90]. The derivation results in a modified Nernst-Planck Equation:

$$\nabla \cdot \vec{J}_{c^\pm} = \mp q \nabla \cdot \left(D_{c^\pm} \nabla c^\pm \pm z_{c^\pm} \mu_{c^\pm} c^\pm \nabla V + a^3 D_{c^\pm} \left(\frac{c^\pm \nabla (c^+ + c^-)}{1 - a^3 (c^+ + c^-)} \right) \right) = \mp q \frac{\partial c^\pm}{\partial t}, \quad (4.17)$$

where the last term in the brackets accounts for the repulsion flux density suffered by ion crowding, such that over-crowding of ions is not possible. This modification term can be intuitively reasoned out without resort to rigorous proof. The denominator represents the space in 1cm^3 of the solution that is unoccupied by ions. The higher the denominator, the more dilute the solution is and the less significant this modification term becomes. In the numerator, the steric repulsion of a species will depend on its own concentration, and the direction of this repulsion will be towards the more vacant locations, which is modeled by the gradient term. This last term adds an extra degree of coupling and results in a severely nonlinear system of equations. Applying the Fourier transform on Equation (4.17) and linearizing the result, we obtain:

$$\nabla \cdot \left(q \mu_{c^\pm} (z_{c^\pm}^2 - z_{c^\pm}) (\tilde{c}^\pm \nabla V_{DC} + c_{DC}^\pm \nabla \tilde{v}) - q \mu_{c^\pm} z_{c^\pm}^2 (\tilde{c}^\pm \nabla V_{qf c^\pm, DC} + c_{DC}^\pm \nabla \tilde{v}_{qf c^\pm}) + K^\pm \right) \pm i \omega q z_{c^\pm} \tilde{c}^\pm = 0, \quad (4.18)$$

where:

$$\begin{aligned}
K^\pm &= \mp q \frac{a^3 \mu_{C^\pm}}{\beta} \left(\frac{\left(1 - a^3 (c_{DC}^+ + c_{DC}^-)\right) \left(c_{DC}^\pm \nabla \tilde{c}^\pm + \tilde{c}^\pm \nabla (c_{DC}^+ + c_{DC}^-)\right) + a^3 \tilde{c}^\pm c_{DC}^\pm \nabla (c_{DC}^+ + c_{DC}^-)}{\left(1 - a^3 (c_{DC}^+ + c_{DC}^-)\right)^2} \right) \\
&= \mp q \frac{a^3 \mu_{C^\pm}}{\beta} \left(\frac{\left(1 - a^3 (c_{DC}^+ + c_{DC}^-)\right) c_{DC}^\pm \nabla \tilde{c}^\pm + \left(1 - a^3 c_{DC}^\mp\right) \nabla (c_{DC}^+ + c_{DC}^-) \tilde{c}^\pm}{\left(1 - a^3 (c_{DC}^+ + c_{DC}^-)\right)^2} \right) \quad (4.19) \\
&= \mp q \frac{a^3 \mu_{C^\pm}}{\beta} \left(\frac{\left(1 - a^3 c_{DC}^\mp\right) \nabla (c_{DC}^+ + c_{DC}^-)}{\left(1 - a^3 (c_{DC}^+ + c_{DC}^-)\right)^2} \tilde{c}^\pm + \frac{c_{DC}^\pm}{1 - a^3 (c_{DC}^+ + c_{DC}^-)} \nabla \tilde{c}^\pm \right)
\end{aligned}$$

The quantity K therefore represents the AC current flux due to steric repulsion. In the bulk of the solution, the contribution of K is small due to the diminishing values of the DC ion concentration gradients in Equation (4.19). However, as the concentration of any species goes higher, the value of this steric repulsion current increases. This is generally quite important at interfaces where double layers are present, as in the case of the active insulator's surface in the BioFET.

Although steric effects help with the DC sensing of the BioFET, this is not readily true for impedance measurements. Steric effects will indeed help with the inversion of the channel and allow for a higher transconductance. However, the steric effects will add impedance to the Debye layer closer to the DNA layer and the sensitive surface. If hybridization of DNA does not significantly alter this layer, the impedance of this layer can dominate the total impedance, thereby desensitizing the BioFET to the hybridization. In order to study this effect, a simulation was carried out with the steric effects (Equation (4.18)) included. To properly incorporate the steric effects and to allow convergence, the steric factor K must be re-written in terms of the quasi-Fermi levels, instead of the AC charge. Using the following definitions for the AC charge density and its gradient:

$$\begin{aligned}
\tilde{c}^\pm &= \mp z^\pm \beta c_{DC}^\pm \left(\tilde{v} - \tilde{v}_{qf c^\pm} \right) \\
\nabla \tilde{c}^\pm &= \mp z^\pm \beta \left(\nabla c_{DC}^\pm \left(\tilde{v} - \tilde{v}_{qf c^\pm} \right) + c_{DC}^\pm \left(\nabla \tilde{v} - \nabla \tilde{v}_{qf c^\pm} \right) \right) \quad (4.20)
\end{aligned}$$

we arrive at the following expression:

$$K^{\pm} = \frac{z^{\pm} q \mu_{c^{\pm}} c_{DC}^{\pm} a^3}{1 - a^3 (c_{DC}^{+} + c_{DC}^{-})} \left(\left(\frac{(1 - a^3 c_{DC}^{\mp}) \nabla (c_{DC}^{+} + c_{DC}^{-})}{1 - a^3 (c_{DC}^{+} + c_{DC}^{-})} + \nabla c_{DC}^{\pm} \right) (\tilde{v} - \tilde{v}_{q/c^{\pm}}) + c_{DC}^{\pm} (\nabla \tilde{v} - \nabla \tilde{v}_{q/c^{\pm}}) \right). \quad (4.21)$$

Figure 4.13 shows the results of the simulations as conducted with and without steric effects included in the AC formulation. Steric effects on the DC solution (which was discussed in Chapter 3) were not included here. This was done so that we could focus on the role of steric hindrance in perturbing the AC solution alone. For all ranges of frequencies, and all levels of inversion, the curves of Figure 4.13 almost overlap for the two cases with and without steric effects included. In reality, the AC admittance will change more, but only due to the effect of the steric hindrance on the DC solution. Thus, the only apparent effect of steric interactions is a small shift in the threshold voltage, and a change in the value of the transconductance.

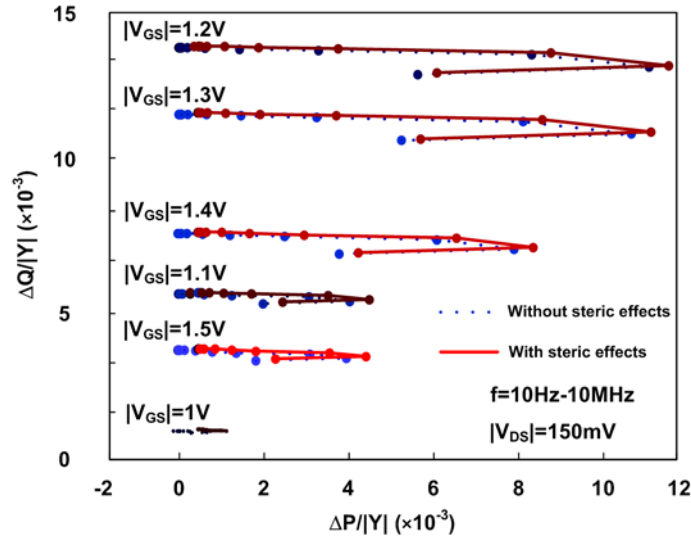


Figure 4.13 Relative change in the admittance of the BioFET due to hybridization, with and without steric effects included

A final note about steric interactions: although we have demonstrated that the modified Nernst-Planck equation (Equation (4.17)) is redundant in the case of small-signal AC analysis, this result does not hold true with large signals, such as those conducted in cyclic voltammetry. Small signals do not cause significant local current overcrowding, and the steric repulsion term is minute. However, if large signals are to be

modeled, then the steric interactions can be large. In this case, the linearized AC equations will also fail, and the complete time-dependent solution would have to be integrated by numerical means.

4.6 Summary

This chapter introduced the dynamic AC modeling of DNA BioFETs. It is based on the linearized frequency-domain partial differential equations of the transport equations in the semiconductor and the electrolyte, as well as linearized first-order kinetics of the reactions on the surface of the sensor. Using the AC model, EIS diagrams were generated. These diagrams allowed the identification of optimum operating frequency and electrolyte concentration. It is concluded that using impedance to measure the hybridization of the FET can be superior to regular DC measurements for the same environmental conditions. The AC model developed here can be extended to include several other side-effects and cross-reactions, as well as different reaction kinetics.

Chapter 5

MONTE-CARLO SIMULATIONS ON DNA BIOSENSORS

5.1 Introduction

DNA sensors and other biosensors are known to possess an inherent variance in the sensed signal. The source of this variance is yet unknown, but is generally attributed to poor microfabrication techniques and lack of control of the post-processing of these sensors [156]. While these are definitely important factors in the design of reliable biosensors, we study in this chapter some other, more fundamental causes of the variation. Firstly, we identify the motion of single-stranded tethered DNA as a source of temporal variation in the sensed signal. The motion of the DNA is studied using a simplified model and Monte-Carlo Metropolis analysis, coupled with the Finite-Element Method (MCM-FEM). Another source of variation in DNA biosensors, and especially nanowires, is the position of the DNA probes within the sensitive area. The asymmetry of the sensitivity of different regions within the BioFET (briefly introduced in Chapter 3) will cause variations in the sensed output. This variation is quantified using simulations, and useful conclusions are deduced.

5.2 MCM-FEM Model of DNA Conformation

As mentioned in Chapter 1, there are several proposed methods by which the BioFET operates, with enough evidence (simulation or experimental) to justify these methods. We have studied in Chapters 3 and 4 how some often simple and overlooked phenomena can considerably affect the sensitivity of the biosensor. It is therefore established that the

sensitivity of the BioFET is due to combined contribution from many processes, all of which have to be considered.

One method that has not received much attention, and which seems critical enough to warrant further research, is the conformational change of DNA upon hybridization. So far, most simulation works (including our own) have considered the tethered oligonucleotides as frozen cylinders whose charge merely doubles upon hybridization. One geometric aspect of the permeability of the DNA cylinder was considered in Chapter 3. Here, it is acknowledged that the single-stranded DNA does not possess the structural integrity of a helical DNA molecule. Several bonds within the DNA are free to rotate and bend with different energy penalties. In a double-stranded DNA, the hydrogen bonds of the paired bases and the base stacking dispersion forces add rigidity to the DNA molecule, such that the allowed degrees of freedom are only vibrational for a tethered double-stranded short DNA. All bonds and sub-molecular geometry of the DNA have been extensively studied, and such data is extensively used to tweak molecular dynamics force-field parameters to probe the fine kinetic details of DNA segments over short time periods [157].

It is proposed here that the conformational change of DNA, from a swollen ion-permeable irregular average shape to a rigid cylinder, is a main contributor to the sensitivity of the BioFET. Hybridization compacts the charges that were otherwise somewhat diffuse within a small extension into the bulk solution. Small changes in the distance between these charges and the insulator's surface can lead to large variations in the image charge in the semiconductor's channel. This is shown in the following sub-section.

5.2.1 Hemispherical Model

To assess whether including geometrical details is necessary or not, we use a simplified model for a single-stranded DNA molecule. A model for short oligonucleotides suspended in a solution [158] is to treat the molecule as an ion-permeable sphere, with radius of gyration in the order of $n^{3/5}$, where n is the number of bases on the DNA. We will assume that this approximation is valid for tethered single-stranded DNA molecules,

but with a hemispherical shape due to interaction with the substrate. As shown in Figure 5.1, the hybridization of the DNA converts the shape from a flailing chain to a rigid rod. In practical DNA experiments, the target is not of the same length as the probe, and a small section of the target might remain unhybridized. This residual DNA could help with the sensitivity, as it adds negative charge to the sensitive surface. However, the length of this unhybridized segment is unknown, and this adds uncertainty in the observed signal. On the other hand, if the electrolyte's concentration is made such that the Debye length only extends to the end of the hybridized segment, then the flailing end can be screened and will not be sensed. It is assumed in this chapter that this indeed is the case.

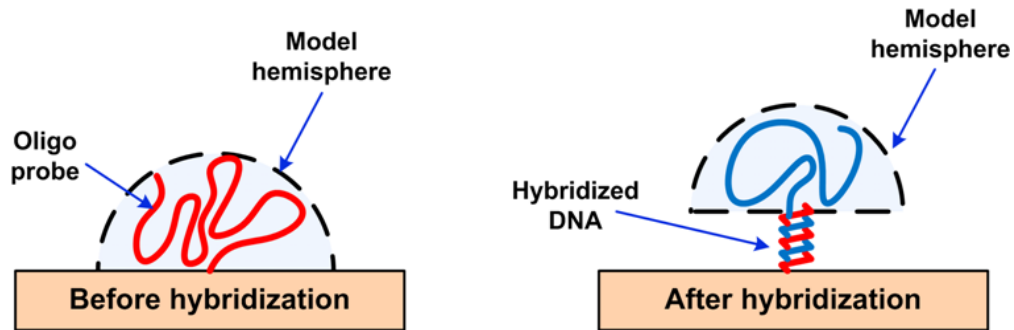


Figure 5.1 Conformation of single and double-stranded tethered DNA

The charge density inside the hemisphere is assumed to be uniformly distributed within the hemisphere, and given by:

$$\rho = \frac{-3qn}{2\pi r^3}, \quad (5.1)$$

where r is the radius of gyration of the tethered DNA oligonucleotide. Of course, this is a big approximation, since the charge distribution for a tethered probe is not uniform. In particular, the averaged charge is taken to account for the random thermal motion of the DNA and represent it by a mean-field. However, it is intuitive that the point of attachment does not randomly move, whereas the points close to the periphery of the hemisphere are the most parts that move. Thus, the charge density is expected to be less concentrated at the end of the DNA. A more accurate charge density would be a radial function. However, to simplify the calculations, the uniform model will be used.

The FEM model is the same as that described in Chapter 2. However, in this case, only the double-stranded DNA is modeled as an impermeable cylinder. The single-stranded DNA is modeled as a diffuse, ion permeable hemisphere of radius $(ln^{3/5})$, where l is the length of the monomer. This length can be roughly calculated by summing up all the bonds between two consecutive phosphate groups in the DNA. We use $l=7$ angstroms, and $n=25$ bases in our simulation. Successful hybridization is modeled by changing the conformation of the DNA hemisphere into a cylinder. It is expected that the packing of the charges closer to the insulator's surface will have an enhanced effect on sensitivity.

Figure 5.2 shows the simulation results of the change in the BioFET drain current for three different electrolyte concentrations. The curves with filled points correspond to the normal simulations (those conducted in Chapter 3) without any change in the DNA concentration. The hollowed curves, on the other hand, correspond to the anomalous *decrease* in the current due to hybridization, when the hemispherical conformation of the oligonucleotides is taken into consideration (hollowed curves have been mirrored about the x-axis to save space).

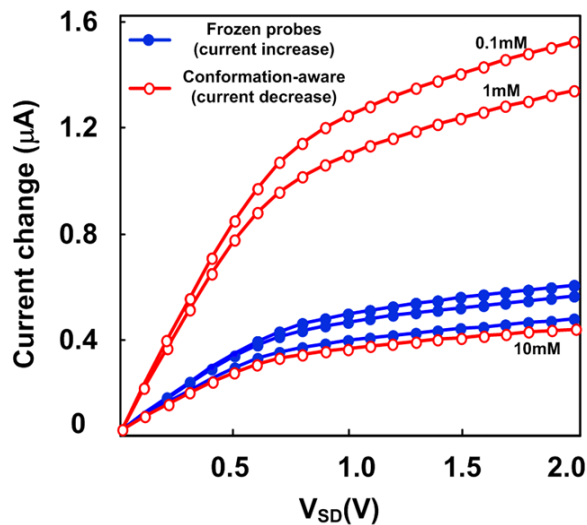


Figure 5.2 Comparison of the simulated BioFET signal with and without geometry considerations

At first, the anomalous result of current decrease seems to be inexplicable. There are no consistent reports of a positive threshold shift in a p-type BioFET due to DNA hybridization. However, since the model is based on physical phenomena, this effect must

have some physical roots. A deeper inspection of the geometry can shed some light into the issue. With the aid of Figure 5.3, the source of this negative signal can be seen. Although the charges have indeed been brought closer to the surface after hybridization, their lateral extent has also shrunk. The region directly beneath the DNA anchor point has an increased inversion charge, but the regions adjacent to it, which were under the hemisphere, are no longer under the influence of DNA charges, and their inversion charge is reduced. Since the current is passed laterally along the BioFET, the distribution of the inversion charge along the direction of current travel is the most important factor that determines the sensitivity, and not the total inversion charge. Therefore, even though the total inversion charge is larger when the conformational change is taken into account, the non-uniform distribution of this charge causes the total resistance of the channel to increase, and the total current is reduced.

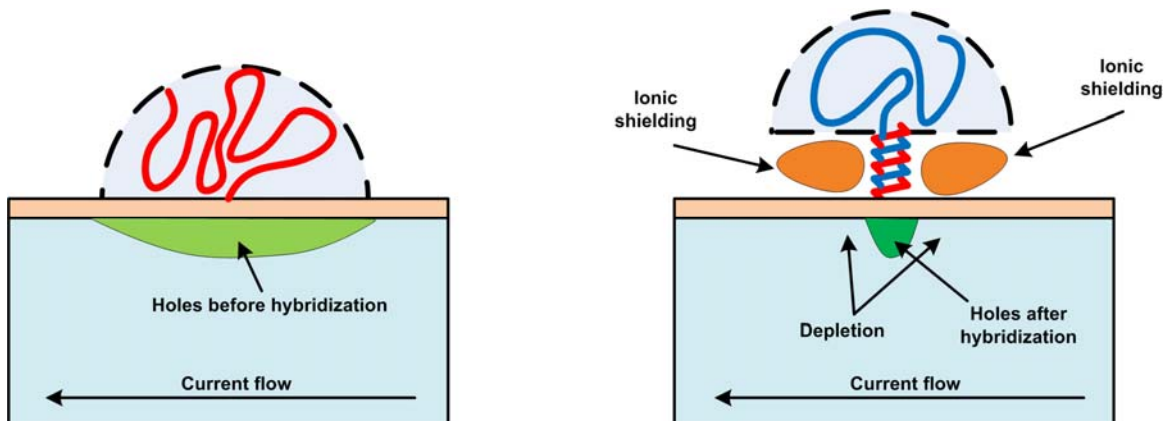


Figure 5.3 Illustration of charge distribution before and after hybridization of the hemispherical DNA, showing the regions of local depletion (see text)

5.2.2 Basic Statistical Model of DNA Polymers

The hemispherical model predicts incorrect results, indicating that this model is not appropriate for tethered oligonucleotides. Proper analysis of the conformational properties of the DNA requires elaborate molecular dynamics models, with sophisticated models for all the chemical interactions and potentials. Molecular dynamics simulations can give accurate time evolution of the motion of the DNA. However, they are computationally

exhaustive and cannot be used for conformational studies of the DNA since this would require large computational time. Several coarse-grained models for the DNA allow processes with longer times to be simulated, but can still not be used to adequately sample the conformational space of the DNA and produce reliable results.

The other method of modeling DNA molecules is macroscopic thermodynamics. Often, the thermodynamic properties are deduced from simple “toy” models of the molecule under consideration. Using these models, statistical expressions can be deduced for the energy and configurational entropy, which then allow the calculation of the most probable (stable) states of the molecule.

The model generally used for the DNA is the **Freely-Jointed Chain (FJC)** model. This model is used to extract thermodynamic information from polymers, and its use was first pioneered by P. Flory [159] -[161] . Using the FJC model, models for the osmotic pressure [162] , entropy [163] , and hydrodynamic properties [164] , and many others, have been estimated. The FJC model assumes that the polymer is made up of n discrete segments of length l each. The links are free to rotate without any energy penalty, and the chain is able to cross itself (i.e. the chain occupies zero volume in space). The FJC is depicted in Figure 5.4. If statistical derivation alone is used, it can be shown [165] that the end-to-end distance of the polymer has a distribution given by the spherical Gaussian distribution:

$$f(\mathbf{r})dV = \left(\frac{b}{\sqrt{\pi}}\right)^3 e^{-b^2 r^2} dV , \quad (5.2)$$

where:

$$b^2 = \frac{3}{2nl^2} . \quad (5.3)$$

This leads to an expected root-mean-square distance given by:

$$\sqrt{\langle r^2 \rangle} = l\sqrt{n} . \quad (5.4)$$

This result is valid for the ideal chain model. In general, a slightly different formula $n^{3/5}l$ is used, which gives a larger root mean radius of gyration. This increased radius is attributed to the effect of the solvent in spreading out the polymer chain by

means of hydrophilic interactions with the chain's wall. The exponent value of 3/5 is Flory's calculated value for good solvents.

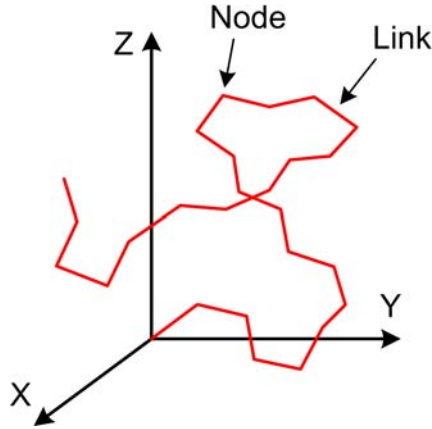


Figure 5.4 Freely-Jointed Chain model, showing the links and the nodes

For the BioFET, we are primarily interested in the average conformation and space occupancy of the single-stranded DNA, as well as the distribution of the charges throughout this volume. Since the chain's conformation is free of any energy penalties and does not suffer from volume exclusion, the Gaussian expression for the end of the chain can be applied to any subsection of the chain. This means that any joint of the chain can be considered as the end point of a smaller chain. If one charge unit is present in each joint, the total charge density profile is given by:

$$\rho(\mathbf{r})dV = \sum_n \left(\frac{3}{2nl^2\pi} \right)^{3/2} e^{-\frac{3r^2}{2nl^2}} dV, \quad (5.5)$$

with the normalization condition:

$$\int \rho(\mathbf{r})dV = n. \quad (5.6)$$

The fact that the tethered DNA molecule cannot span an entire sphere (due to the impermeable tethering surface) allows us to arbitrarily multiply Equation (5.5) by a factor of 2 to account for a hemispherical occupancy. Equation (5.5), although not Gaussian, still has the main characteristics of a Gaussian function (Figure 5.5), but with a higher standard deviation.

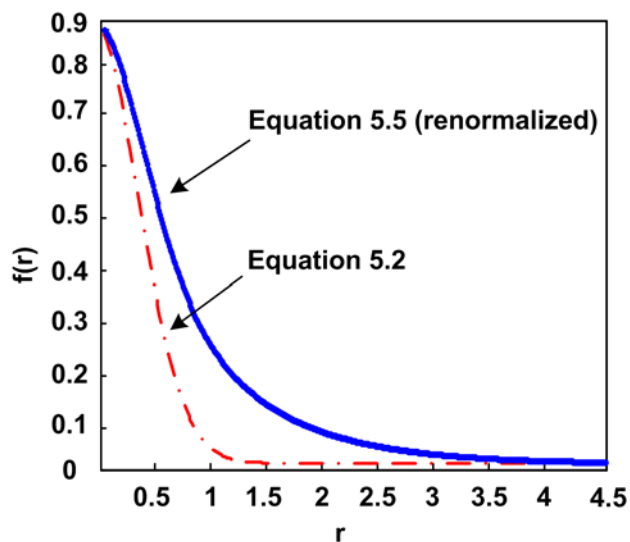


Figure 5.5 Comparison of the spherical Gaussian distribution (Equation 5.2) and the summed Gaussian (Equation 5.5)

Unfortunately, even when the distribution function of Equation (5.5) replaces our earlier assumed uniform distribution, the anomalous results of reduction in the drain current upon hybridization still persist, but to a lesser extent (results not shown). This indicates that there are still some problems with the conformation of the single stranded DNA. Some of the reasons why the FJC model might not suffice are given below:

1. The FJC model still seems to predict a spherical shaped average conformation of the DNA. We have reasoned earlier that this might be the one reason for getting a negative signal. It is expected that single-stranded DNA molecules would have a more “mushroom” like shape, as predicted in other works [158]. Furthermore, the effect of the sensor’s surface on prohibiting the motion of the DNA is ignored in the FJC model.
2. Most of the work in the literature that use the FJC to model DNA molecules consider very long strands of double-sided DNA molecules. The persistence length of a DNA molecule is in the range of 50nm [166], much longer than the extended length of our oligonucleotides. Thus, many of the approximations given in other works, and that give simple analytical results; do not apply in our case.

3. Allowing overlap of the chain molecules might be an appropriate approximation for short DNA segments, since the volume occupied by the bases and the backbone is of the same order of the total average volume occupied by the oligonucleotide. Thus, steric effects must be included. There has been some work that address steric effects [167] , [168] , but the models used are generally applicable to longer polymer molecules.
4. DNA is a charged polymer, and at the very least, electrostatic repulsion energy between the bases has to be considered. The FJC model does not consider the charged nature of the molecule [161] .
5. The interaction of the DNA with the shielding salt molecules must be considered. This has been partially addressed before [169] . However, a linear model for the shielding was used for each monomer. We have demonstrated that the linear model does not suffice for a highly charged polyelectrolyte. Furthermore, the overlap of the screening charges might have an energetic effect (often stabilizing, as will be seen later) on the entire molecule. This “sticky” behavior of the screening charge was not included in the work of [169] .

5.2.3 Simplified Model of DNA

The approach we use here is to combine the FEM model of the electrolyte and semiconductor with a chain model of the DNA. The chain model used is what is generally referred to as the “ball and stick” model. Shown in Figure 5.6, this model allows the DNA molecule to possess a volume, and to be susceptible to steric effects. The molecule is taken to have 25 segments, each containing a ball in the middle that represents the van-der-Waals steric radius of that unit. In reality, this is a very coarse approximation. The backbone of the DNA molecule is shown in Figure 5.7. Between every two adjacent phosphate groups, there are six bonds (α through ζ). These bonds can twist with various ranges [157] , but the cumulative bending angle between subsequent phosphate groups does not exceed 90° . Thus, we simplify the problem by joining all of these degrees of freedom into one single angle (two in the case of 3-D modeling), and setting a maximum

range of fluctuation of this angle to span the range from -90° to 90° . At any segment, the angle 0° is measured from the extension of the previous segment.

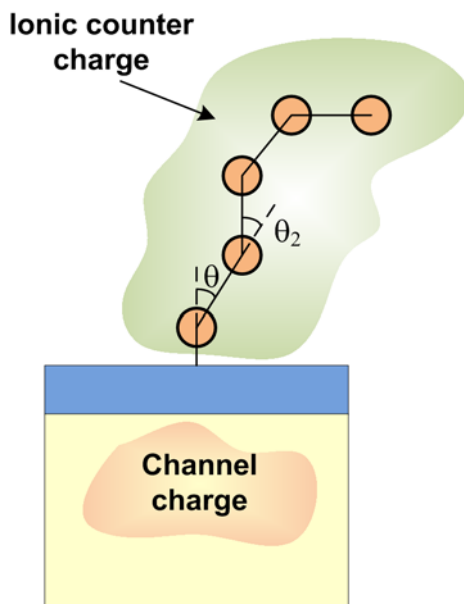


Figure 5.6 Ball and stick model used for the MCM simulation

The spheres are meant to approximate the tetrahedral phosphate groups. The van-der-Waals radius of the spheres is taken to be 0.3 nm. This is larger than the reported [157] P-O bond length of 0.171 nm. The reason for enlarging the radius is twofold: firstly, the van-der-Waals radius of the molecule is larger than the bond length, since the bond length merely considers the center-to-center atomic distance, without considering the outer electron cloud. Secondly, a larger sphere will prevent the DNA chain from crossing itself. The alternative would be to model the connecting rods as rigid elements. However, this is computationally and geometrically inefficient. To model the connecting rods, a fixed distance of 0.61nm was imposed upon the adjacent spheres. This number was chosen as the sum of the bond lengths of all the links between the two phosphate groups in Figure 5.7, namely, two ester bonds, an aromatic C-C bond, and a single C-C bond. Of course, this is another approximation since these links are not fully extended.

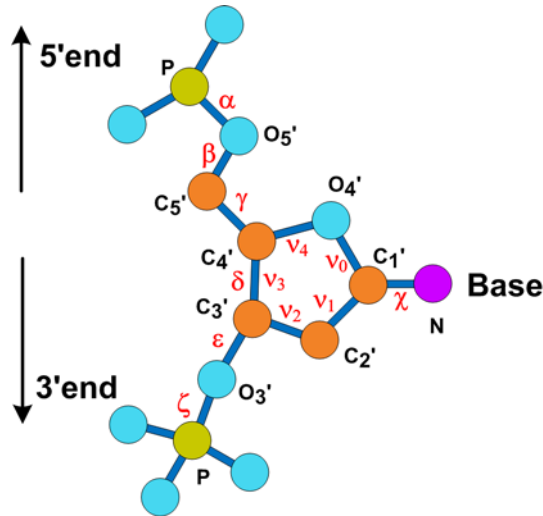


Figure 5.7 Atomic organizational structure of a DNA backbone

The DNA molecule model is fixed on top of the insulator and a semiconductor. Steric interactions are accomplished using brick-wall volume exclusion. In software, this was done by counting the number of subdomains for each DNA conformation. A legal conformation would result in 28 subdomains (25 for each sphere in the DNA molecule, 1 for the electrolyte, 1 for the insulator, and 1 for the semiconductor). If the counted domains increase (two intersecting spheres making 3 subdomains, or the sphere intersecting the insulator layer), or decrease (two or more completely overlapping spheres counting as one), then this conformation is rejected as a high-energy state.

The equations to model this system are the same as those discussed in Chapter 3. The nonlinear Poisson-Boltzmann equation is used for the electrolyte solution, and the nonlinear transport equations, i.e. Equation (3.9), are used for the semiconductor. The spheres are assumed each to have a charge of $-q$. Thus, Poisson's equation is used to model potential variation within the sphere. It is acknowledged that the internal electronic structure and more advanced water models are needed to properly model the average conformation of DNA at these small length scales. However, our goal here is to see if pure classical electrostatics can suffice to predict a more realistic conformation of the DNA.

To predict the conformation of the DNA molecule, we perform a Monte-Carlo simulation by selecting random bending angles for each segment in the DNA model. Instead of choosing a completely new angle each time, the randomized value is the *change* in the angle. The value is chosen uniformly within a small range from the current value, while respecting the overall limits of -90° to 90° from the extension of the previous link. This is done so that once the DNA has been “trapped” into a conformation of low energy; it cannot immediately come out of it. The average conformation has to be taken after the DNA molecule has settled into a low energy conformation. It is important, therefore, that once a low-energy conformation is achieved, only thermal agitation can cause the DNA molecule to temporarily be released from it, and not the Monte-Carlo algorithm.

For each Monte-Carlo step, a complete FEM problem is solved to find the potential and ionic distribution in the solution, as well as the electron and hole distribution within the semiconductor. The Monte-Carlo-Metropolis algorithm calculates the total free energy of the ensemble of DNA, ions, electrons, and holes to estimate the free energy of the conformation. Firstly, the electrostatic energy of the DNA molecule, in electron volts, is given by:

$$E_{DNA} = \frac{1}{2} \sum_n N_{DNA} \int (V_n(\mathbf{r}) - V_{ref}) d\mathbf{r}, \quad (5.7)$$

where N_{DNA} is the charge density of each DNA sphere, V_{ref} is the reference potential in the bulk of the solution, and the variable n sums over all DNA segments. Similarly, the electrostatic energy contributions of the ions and carriers in the semiconductor are given by:

$$E_{ions} = \frac{1}{2} \int (z c_0 \sinh(z \beta (V(\mathbf{r}) - V_{ref}))) (V(\mathbf{r}) - V_{ref}) d\mathbf{r}, \quad (5.8)$$

and

$$E_{carriers} = \frac{1}{2} \int n_i \left(e^{\beta(\phi_F - V(\mathbf{r}) + V_{body})} - e^{-\beta(\phi_F - V(\mathbf{r}) + V_{body})} \right) (V(\mathbf{r}) - V_{body}) d\mathbf{r}, \quad (5.9)$$

respectively, where ϕ_F is the Fermi level of the semiconductor and V_{body} is the potential of the bulk. In addition, there is energy associated with the fixed impurity charges in the semiconductor N_{imp} . This is given by:

$$E_{dopants} = \frac{1}{2} \int n_i \left(e^{-\beta\phi_F} - e^{\beta\phi_F} \right) \left(V(\mathbf{r}) - V_{body} \right) d\mathbf{r}. \quad (5.10)$$

In addition to the energy calculations, the entropy of the ions and carriers must be included. The PB equation guarantees the ionic configuration that will maximize the entropy (hence, places the system in equilibrium). However, the value of this entropy is not known, and it becomes necessary to know so as to decide on which DNA conformation is more likely. The expression for the entropy of a real solvated ion can be very complex. Here, we adopt the entropy expression for an ideal gas of many components c_i , given by:

$$S_{ions} = -k \sum_i \int (c_i \ln c_i - c_i) d\mathbf{r}. \quad (5.11)$$

Equation (5.11) gives the entropy of the ideal gas, correct to a constant factor. This unknown constant factor does not matter in our calculations since the MCM method only converges based on the change of the total free energy change of the system. For the ions, Equation (5.11) becomes:

$$S_{ions} = \frac{-kC_0}{q} \int \left(\left(e^{\beta(V - V_{ref})} \right) \left(\beta(V - V_{ref}) - 1 + \ln(c_0) \right) + \left(e^{-\beta(V - V_{ref})} \right) \left(-\beta(V - V_{ref}) - 1 + \ln(c_0) \right) \right) d\mathbf{r}, \quad (5.12)$$

whereas for the carriers, the formula is

$$S_{carriers} = \frac{-kn_i}{q} \int \left(\left(e^{\beta(-\phi_F + V(\mathbf{r}) - V_{body})} \right) \left(\beta(V(\mathbf{r}) - V_{body}) - 1 \right) + \left(e^{-\beta(-\phi_F + V(\mathbf{r}) - V_{body})} \right) \left(-\beta(V(\mathbf{r}) - V_{body}) - 1 \right) \right) d\mathbf{r}. \quad (5.13)$$

The total free energy is then given by:

$$G = E - TS = E_{ions} + E_{DNA} + E_{carriers} + E_{dopants} - T (S_{ions} + S_{carriers}). \quad (5.14)$$

We notice here that the entropy of the dopants and that of the DNA are not included. The dopants are considered immobilized such that they cannot change their configurational entropy upon change of bias, and hence have no entropy component. As for the DNA, this model treats it within a microscopic model, unlike the mean-field ions

and carriers. The concept of entropy is an extensive macroscopic thermodynamic property, and only has meaning when the internal configurations of the molecule are considered in an average sense. After the MCM simulation stabilizes, the DNA molecule will continue to hop between low-energy configurations. The more these configurations there are, the higher will be the entropy of this molecule.

5.2.4 Results

The simulation was run for electrolyte concentration of 1mM and flat-band bias, to remove the effect of the double layer in which the DNA is immersed. The simulation was carried out twice, for 100,000 iterations each. The simulation took a week of a single PC execution time. The main reason for the long simulation is that most randomized conformations had to be discarded due to overlap of subdomains. A “smart” randomization scheme is possible, but such a scheme might contaminate the attempt to replicate a truly thermodynamic system. For the first simulation, all Monte-Carlo steps were used, whereas for the second simulation, the MCM algorithm was invoked, in which lower energy conformations are immediately selected, whereas conformations with larger energy are selected with a decaying exponential probability that depends on the energy difference, thus accomplishing equilibrium thermal fluctuations. Figure 5.8 shows superimposed images of the locations of the DNA nodes throughout both simulations. For the figure on the left, it can be seen that the conformation seems indeed to be spanning a hemispherical shape. When the energetic bias is included, we can see from the figure on the right that the “mushroom” shape of the DNA is apparent. This means that the DNA molecule prefers to be more vertical near the base, whereas the ends conform to a locally hemispherical shape. This average conformation dramatically changes the expected signal from the BioFET, since the edges of the single-stranded DNA are not close to the semiconductor. The result is independent on the starting position, as the same result was obtained with the starting DNA molecule being completely vertical or completely horizontal.

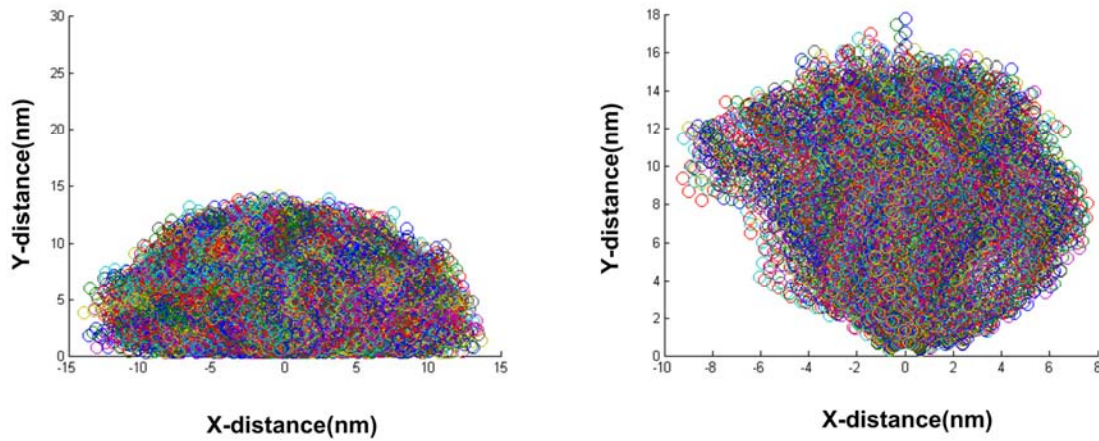


Figure 5.8 Superimposed conformation profile of the single stranded DNA molecule throughout the Monte Carlo simulation, without energy bias (left) and with energy bias (right).

From Figure 5.8, we can conclude that the DNA molecule is forced to a more vertical position by means of the Debye layer of the ions shielding it. Thus, the single-stranded DNA prefers to be surrounded by ions than semiconductor carriers. This makes sense since the ions are much closer to the DNA than the carriers. Paradoxically, this causes the sensitivity of the BioFET to be larger as the conformation of the DNA changes to the cylindrical, double stranded shape.

Figure 5.9 shows the radial and angular histograms of the DNA nodes, which are indicative of the probability distributions of these quantities. As seen, the radial histogram is very different from that of Equation (5.5), supporting our hypothesis that a radial distribution function is not appropriate for describing the average charge distribution in the DNA hemisphere. The histogram is not monotonically decreasing, but seems to be somewhat flat in the middle. This suggests that while the initial nodes of the DNA (closer to the tethering point) have a stretched profile, the end tends to curl on itself and increase the local charge density. A snapshot of one of the MCM conformations is shown in Figure 5.10. The maximum radial distance of the DNA is around 15 nm, which is almost double the expected 8.5nm from a 35 base pair coiled up DNA. The angular histogram also shows that the DNA segments are within around 30° from the vertical position. This means that the hemispherical model is indeed incorrect for tethered DNA molecule.

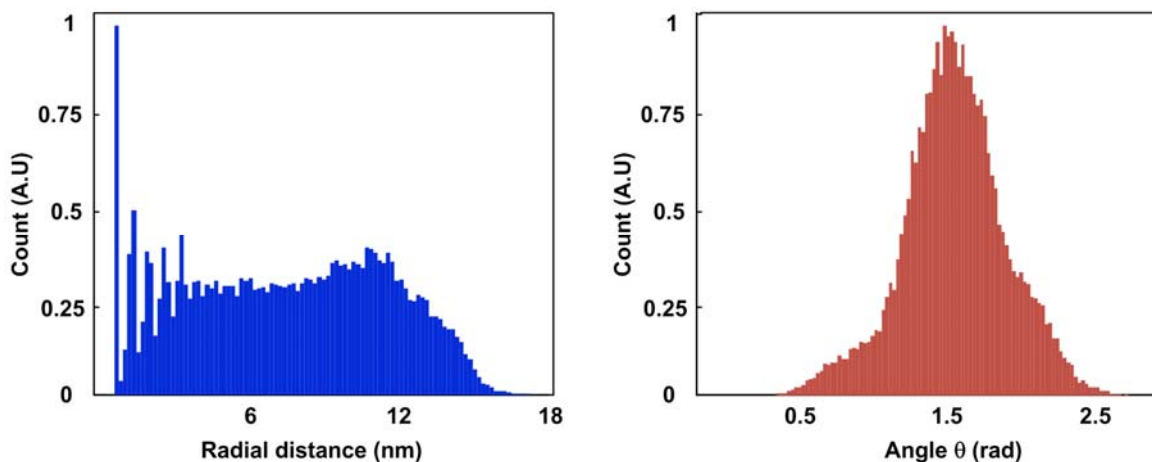


Figure 5.9 Histogram of the simulated radial (left) and angular (right) positions for the DNA segments.

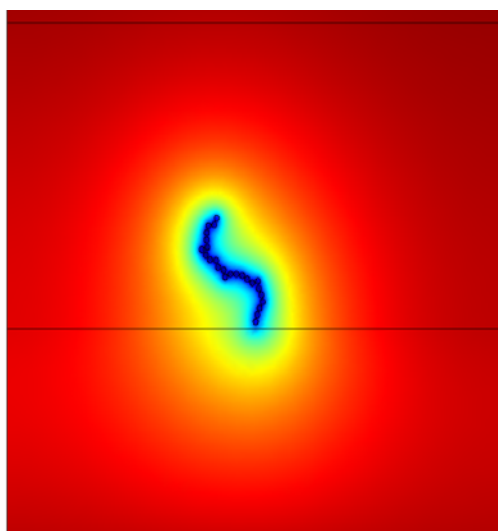


Figure 5.10 A sample conformation from the MCM-FEM algorithm

It is interesting to see whether a reference electrode bias would have any influence on the conformational properties of the BioFET. At first, one might expect the potential to attract or repel the DNA molecules and make them more flat or more vertical. However, in reality, the double layer that screens the DNA molecule, as well as the double layer on top of the insulator, can combat the effect of the applied potential in changing the conformation of the molecule. This phenomenon is interesting to observe because if it is shown that bias can severely change the conformation of the DNA, this would give

another technique of sensing DNA hybridization that has the potential of being extremely sensitive. One could monitor the variation of a low-frequency cyclic voltammogram before and after hybridization. CV experiments are often used to detect the prevalence of certain reactions. In this case, however, the CV measurement would give information about the conformational change of the DNA molecule. A hybridized layer would not change conformation with the applied potential and would have minimal effect on the voltammogram, whereas a nonhybridized layer would be more flexible and could potentially cause severe changes to the voltammogram.

The MCM-FEM simulation was carried out under a reference electrode bias of -1V. Figure 5.11 shows the simulated radial and angular distribution of the DNA nodes. The results seem very similar to those of Figure 5.9. However, there are subtle differences. Firstly, by comparing the radial histogram to that of Figure 5.9, it is clear that the average moves towards lower values. In particular, the second peak has moved from around 11 nm to 9 nm. The overall swelling of the DNA molecule has not changed, but the distribution of the charges within the occupied volume is different. This is explained by a net repulsion of the DNA due to the bias on the reference electrode. This phenomenon can lead to a reduction in the sensitivity of the BioFET, as the main influence of the conformational change is to bring the charges closer to the surface of the insulator. The angular distribution also supports this repulsion by predicting a more distributed angular span than that which is seen by Figure 5.9. The repulsion of the DNA serves to “flatten” the mushroomed top and bring it closer to the surface. However, the overall change does not appear so dramatic, as a change of 2nm in the presence of 18nm of insulation will lead to a very small change in sensitivity. It is not expected, therefore, that the DNA charge distribution will be changed significantly with the applied bias.

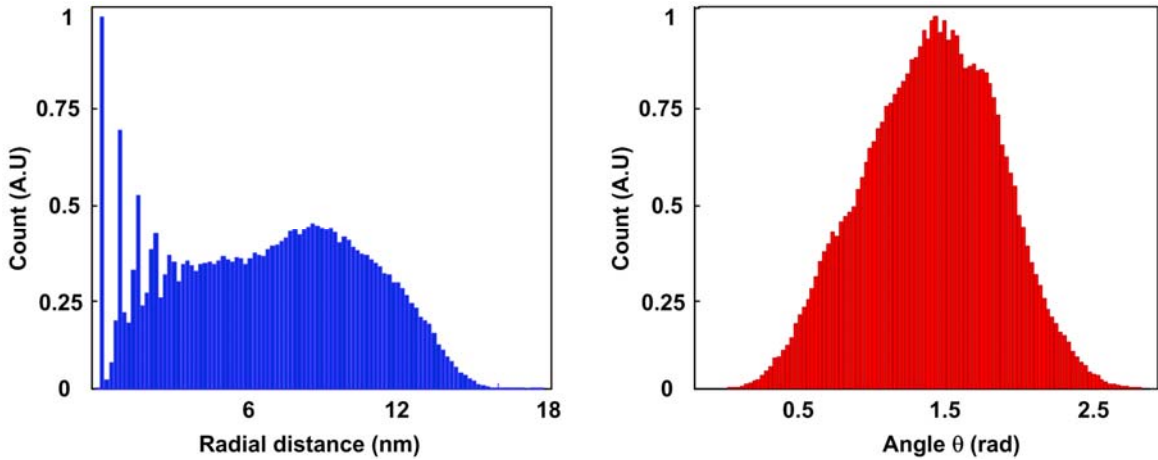


Figure 5.11 Histogram of the DNA conformation with a reference electrode bias of $-1V$.

To summarize the results of this simulation, the main reason for the negative signal received with the simulation results of Figure 5.2 is that the hemispherical model of DNA is not appropriate to describe the average conformation of the DNA. Additionally, the DNA molecule is more swollen and extends deeper into the solution. These two observations indicate that the change in the conformation, from a flailing coil to a compact stiff cylinder, is the main cause of high sensitivity in the BioFET.

5.3 MCM-FEM Model of DNA Distribution within the BioFET

Here, the Monte-Carlo-Metropolis simulation is used to investigate the effect of varying the positions of the DNA probes on the sensor's output signal. It was demonstrated in Chapter 3 how the sensitivity is not uniform throughout the surface of the insulator, especially when the device is operated in saturation. It was also shown that for a uniform distribution of molecules, the sensitivity is optimum. Here, we wish to get a measure of the severity of this variation in the sensed signal. This variation can be seen as a source of "noise" in DNA microarrays. Of course, this noise source is expected to be constant randomized shifts in the sensed signal between cells. However, if the probe DNA molecules are capable of diffusing laterally within the sensor's surface, then this noise becomes a random process and will be characterized by its power spectral density. In this

simulation, we assume that the probes are frozen in place, and focus on the amount of variations in the sensed signal as the positions of the probes are varied.

5.3.1 Evidence for DNA aggregation

Before we proceed with the simulations, it is important to discuss whether there is need to conduct this study. DNA probes are generally transported to the sticky surface by isotropic diffusion. For very low density DNA coverage, it has been shown [109] that Langmuir's isotherm explains the experimentally observed immobilization yield, suggesting that there are no lateral interactions between the probes and that it is expected that the coverage will be uniform. On the other hand, even at moderate densities generally used in DNA microarrays, correction factors have to be included to Langmuir's model to account for probe-probe interaction [109]. Furthermore, it has been shown that bulk long DNA molecules have the tendency to aggregate together [170] in spite of their repulsive electrostatics. We wish here to investigate the energetics of this aggregation and whether or not it is of significance in DNA biosensors.

A simplified, top view model of DNA cylinders is used for the simulation. The cylinders (circles using a top view) are given a charge density consistent with that of a single-stranded DNA. Then, the PB equation is solved for the entire structure. Equations (5.7), (5.8), (5.12), and (5.14) are used to calculate the free energy of the ensemble. Six DNA molecules are placed as shown in Figure 5.12. The FEM simulation is repeated as these DNA molecules are brought closer to each other, and the total energy is plotted as a function of the distance between probes in Figure 5.13.

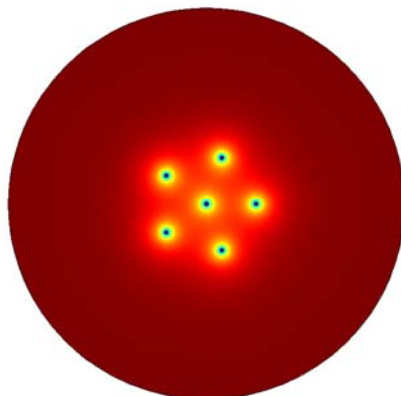


Figure 5.12 Simulated potential profile with six DNA molecules

The result of Figure 5.13 shows that there exists a potential minimum at a specific inter-probe spacing. This is an interesting observation seeing how both DNA molecules are negatively charged. The attractive force, however, comes from the energy contribution of the shielding ions. When the shielding ions are shared amongst two or more DNA molecules, their energies are decreased since they spend most of their time close to a negative charge. This is very similar to the bonding orbital that results from solving Schrödinger's equation for a covalent bond, even though the physics in these two cases has completely different origins.

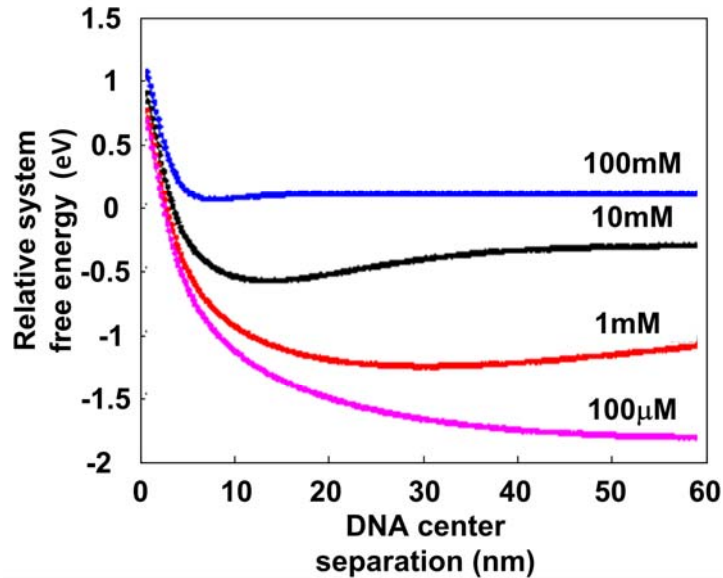


Figure 5.13 Total free energy of the system of six DNA molecules as a function of their inter-distance, at different electrolyte concentrations

The potential minimum in Figure 5.13 depends on the electrolyte concentration. Lower electrolyte concentrations result in larger separations. Since immobilization and hybridization experiments are generally conducted under high salt conditions, the equilibrium distribution of DNA molecules is expected to aggregate due to the low energy close packing evidenced by the results of Figure 5.13. Additionally, it is also expected that there might be several of these aggregates at several different locations within the BioFET. This can be seen by examining the depth of the potential wells in Figure 5.13. We can see that the potential well changes from just around 0.1eV at high electrolyte concentrations up to 0.5eV or more at low concentrations. Thus, it is more possible for the free DNA probe to break loose of the gravitational field of neighboring immobilized probes. At lower electrolyte concentrations, fewer numbers of aggregates will occur since the potential well is deeper and it will be harder for molecules to break free of them by thermal energy alone. However, the aggregation will be more disperse, as the energy minimum occurs at a larger distance.

Since the thermal energy at room temperature is around 25meV, these potential wells are significant, and the issue of DNA aggregation at different locations on the

biosensor's surface should not be disregarded. Of course, one could elongate the incubation time for the DNA molecules to tether and create a uniform film. However, higher probe density can severely hinder hybridization [60] due to crowding of molecules. Additionally, as nano-biosensors emerge, attention is being focused to detecting the smallest number of molecules. This can be accomplished when the number of probes is deliberately made small in a nano-sensor. In all these cases, therefore, it is essential to study the variation of the sensed signal with the position of the DNA probes.

5.3.2 Monte Carlo Model

The 3-D model of the BioFET is used for this simulation, since it is essential to capture the full 3-D shielding effect of the ions to get accurate estimates of the free energy. The structure and equations of the BioFET have already been presented in Chapter 3. Here, we randomize the positions of the DNA molecules on the insulator's surface. This can lead to many practical problems in meshing and modeling. To make the problem more tractable, the randomized locations of the DNA probes on the surface of the insulator were restricted to fall within a grid of square cells shown in Figure 5.14. Each cell allowed a tolerance of 0.2 nm on all sides such that adjacent occupied DNA cells do not share a DNA's cylinder edge, as this could cause very low quality meshing and divergence of the solution.

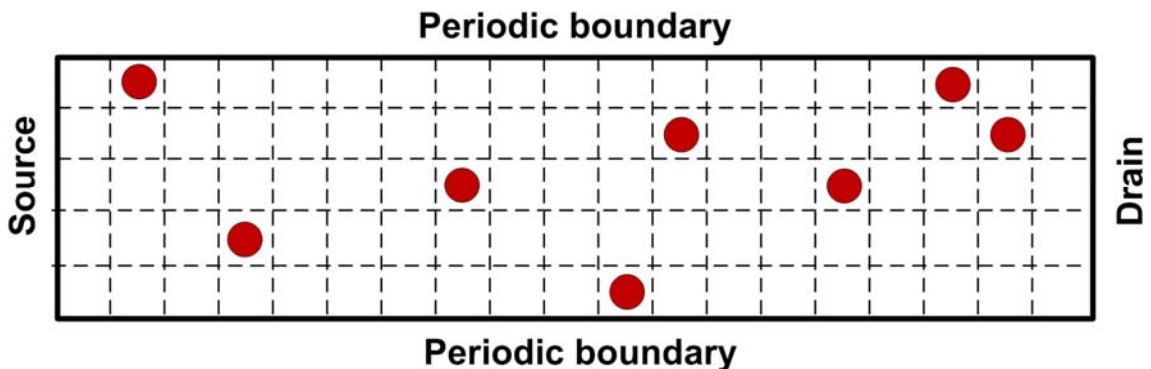


Figure 5.14 Grid used to place the randomized DNA molecules

The computational requirements for this MCM simulation are immense. On the one hand, the size of the BioFET must be made relatively large (400nm length, 10nm

slice width) to de-emphasize short channel effects. Compared to the DNA molecules, this is a very large surface area, and can potentially host several hundreds of DNA molecules. Computational restrictions, however, only allowed the accurate simulation of up to 50 molecules. To relax the computational burden, linear element shape functions were used. This can dramatically reduce the number of degrees of freedom. The mesh was chosen coarse enough to comply with the memory constraints, but fine around the DNA molecules to allow convergence.

5.3.3 Results

The simulations were carried out for DNA counts of 5, 10, 20, 30, and 50. In each case, the current is calculated before and after hybridization, and the signal is taken as the current change between these two values for various different values of V_{DS} . The MCM-FEM algorithm was repeated 1000 times in each case. Figure 5.15 shows the mean signal of all the Monte Carlo runs for the different DNA densities. As expected, higher DNA densities and deeper saturated operation give a higher mean signal. However, we notice that a sharp increase in the mean signal is observed with 50 DNA molecules than the other cases. This sharp increase is due to the more even distribution of DNA along the channel at this density. Conduction of current in a channel is a collective process involving the DNA molecules along the current direction (from source to drain). The DNA density increase in the perpendicular direction (along the width of the transistor) is of smaller effect than its increase over the longitudinal direction. This can be demonstrated with a simple example: Let the channel's conductance associated with the presence of each DNA be given by G_i , with i being the index of the DNA, and let there be 3 DNA molecules along the length of the channel, and one extra DNA molecule along the width. The conductive network is shown in Figure 5.16. If all the conductance values are the same, then the total conductance change with respect to a change in the longitudinal DNA molecules is given by:

$$\frac{\partial G}{\partial G_1} = \frac{1}{G_1^2 (G_1^{-1} + (G_2 + G_4)^{-1} + G_3^{-1})^2} = \frac{1}{(1 + G_1 (G_2 + G_4)^{-1} + G_1 G_3^{-1})^2} = \frac{1}{2.5^2} = 0.16, \quad (5.15)$$

whereas the conductance change with respect to a change in G_4 is:

$$\frac{\partial G}{\partial G_4} = \frac{1}{((G_2 + G_4)G_1^{-1} + 1 + (G_2 + G_4)G_3^{-1})^2} = \frac{1}{5^2} = 0.04. \quad (5.16)$$

We can see, therefore, that G_1 is more important than G_4 in determining the total conductance. With 50 DNA molecules, and with our chosen geometry, the probability of many of them contributing to the lateral conductance starts to be considerable, and the total sensed current sharply increases.

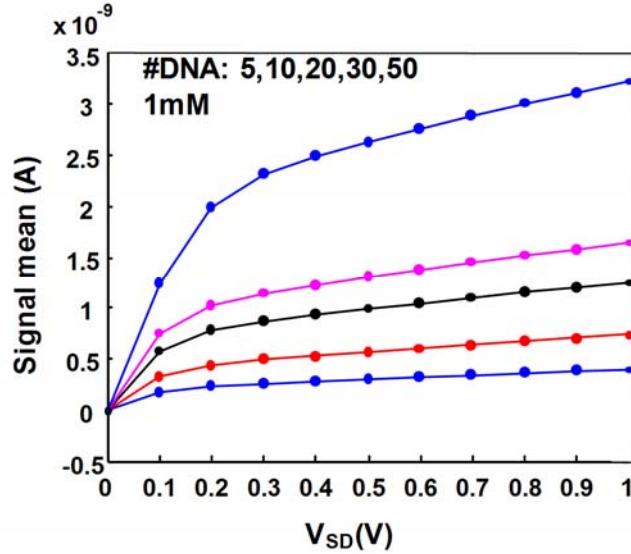


Figure 5.15 Mean BioFET signal for different DNA probe densities

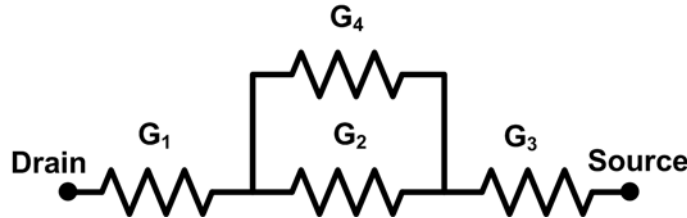


Figure 5.16 Resistor network used to examine the conductance sensitivity of the BioFET's channel to parallel and series image charges

Figure 5.17 shows the standard deviation of the sensed current, for the different DNA molecule counts, plotted against the source-drain bias. It is shown that the variance increases with the bias. Moreover, the rate of increase in saturation seems to vary slightly for lower DNA concentrations. As the DNA concentration is increased, however, the variance begins to flatten out. This is an expected behavior at very high concentrations, at which the number of different permutations for the DNA locations is limited. In our case, the maximum fill factor is below 10%, and still many permutations of the DNA locations are possible. The flattening of the variance in saturation might also be the result of desensitization of a portion of the channel to the presence of DNA molecule due to pinch-off [139] , [141] , [171] . This results in a smaller effective area for the sensed DNA, and fewer permutations.

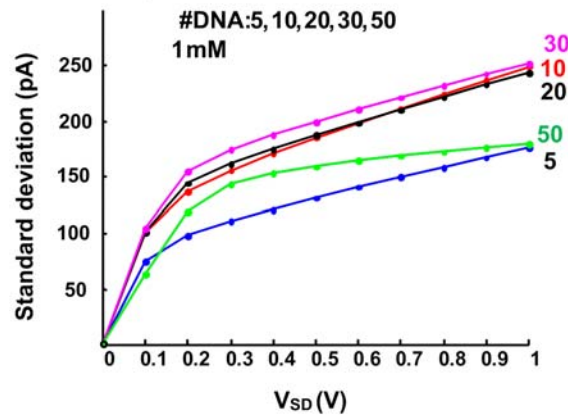


Figure 5.17 Calculated standard deviation of the observed BioFET current for different Monte Carlo runs

In a parallel micro-array, the variations between cells can severely contaminate the data. Noise in microarrays can be attributed to several factors, including biological process-related noise and measurement noise [172] , [173] . Our calculated variance of the signal due to random placements of the DNA is also a source of variation between the cells. This variation can be static, as in the case of covalently tethered DNA probes, or can be present as stochastic processes such as in the case of physisorption of probes, or surface diffusion of unhybridized targets [174] . In such a case, our simulation can only

give an estimate of the total power of the noise and not its complete power spectral density. Molecular dynamics simulations can be used if such detail is needed.

The simulated Signal-to-Noise Ratio (SNR) of the BioFET cell, due to random placement of the DNA probes, is shown in Figure 5.18. Once again, it is intuitive that the higher DNA density will result in higher SNR. The simulation sets a limit to how low the density of DNA should be, before the low SNR value can render the microarray unreliable. We can see that a DNA count of 10 within our simulation domain, which corresponds to coverage of 0.4%, will result in a low value of SNR (below 10). While this might seem to be a low coverage, it is worth mentioning that steric hindering of DNA hybridization can start at coverages as low as 12% [60]. Single molecule sensors and nanosensors can have much lower coverage ratios. Additionally, the other sources of variation (such as doping profile variation or post-processing variations) can introduce their own noise, forcing the minimum coverage to be well above our simulated values. Finally, single-stranded DNA probes do not generally occupy the same area as double-stranded ones, and may swell as a result of their thermodynamic motion. Thus, an apparent coverage, as measured by scanning tunneling microscope probes, might be larger than the actual coverage (the mushroom regime as in [158]).

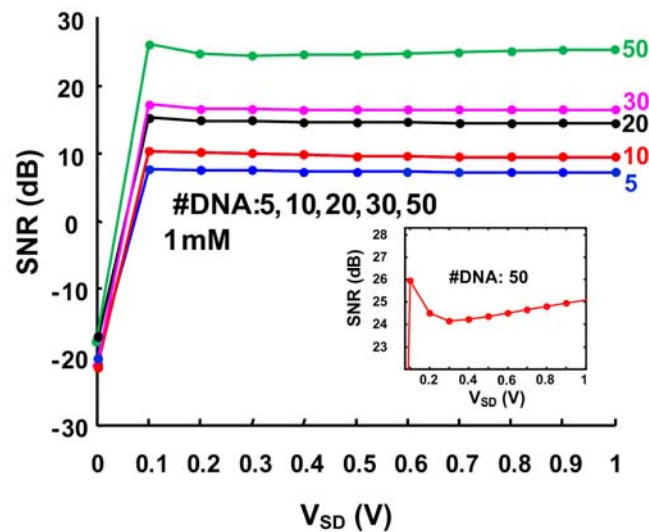


Figure 5.18 Signal-to-noise ratio, as simulated for different DNA densities. Inset: magnified signal-to-noise-ratio for 50 DNA molecules as a function of source-drain bias

The magnified inset of Figure 5.18 also shows that the drain-source bias can affect the SNR value. The maximum value is achieved at the onset of saturation, at which a balance is achieved between the device's transconductance and the desensitization of the BioFET's bioactive surface due to pinch-off. As we transition into deeper saturation, this balance is disturbed and we notice a local minimum of SNR, which quickly begins to pick up again as the pinch-off region ceases to advance farther into the channel. Thus, for maximum desensitization to DNA charge, one should bias the BioFET at the onset of saturation. The generally used ISFET source-drain follower [175], which keeps the BioFET in linear region, is therefore very susceptible to variations in output signal due to random placement of DNA molecules.

The histogram of the Monte-Carlo trials can also yield valuable information about the performance of the BioFET. Figure 5.19 shows sample histograms of the hybridization signal for the Monte Carlo simulations done for 30, 20, 10, and 5 DNA probes within our area of simulation, and for three different electrolyte concentrations: 10mM, 1mM, and 100 μ M. Whereas the histograms for the 10mM concentrations show symmetry with respect to the mean value (as expected from an unbiased Monte Carlo simulation), we notice a gradual departure from symmetry and migration of the mean signal to the higher end of the spectrum. This phenomenon is very evident at high DNA concentration but is almost absent for very low DNA coverage. This can be explained by noting that as the electrolyte concentration is decreased, the double layer condensation around the DNA strands thickens, and the opportunity for counter-ion sharing increases. We have shown that this charge sharing is associated with a decrease in the free energy, making it more probable. However, we also see from the histogram that the signals registered by the conformations that contain overlaps, and which are more likely at lower electrolyte concentrations, result in signals that fall higher in the spectrum. This shows that charge sharing between adjacent DNA probes works in favor of the BioFET sensor, and that more inversion charge is induced in the channel of the semiconductor than in the electrolyte region when the counter-ions are shared. This result encourages post-hybridization dilution of the solution, as this will not only result in an increase in the

mean sensed signal, but will also lower the variance due to random placement of DNA probes.

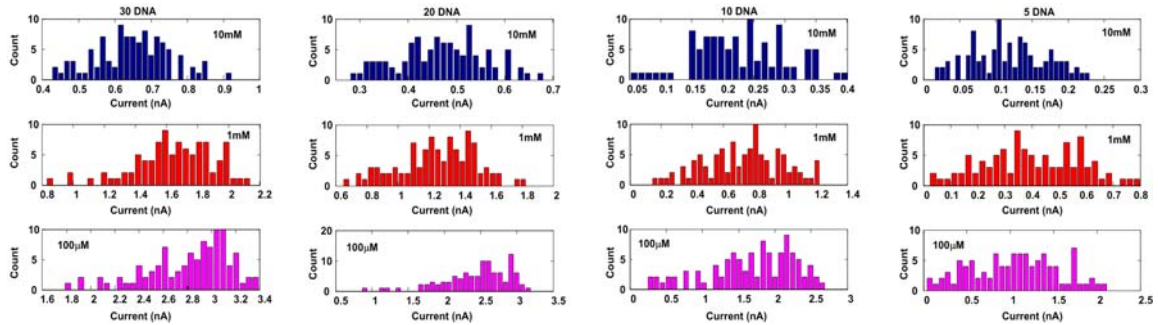


Figure 5.19 Comparison of the signal histograms for different DNA probe densities, at different electrolyte concentrations

5.4 Conclusion

In this chapter, the Monte Carlo-Metropolis algorithm was augmented with the Finite-Element method to model problems of practical significance in the design of the BioFET. This includes the average conformation and charge distribution of the unhybridized DNA probes, and the variation of the output signal with different placements of the DNA probes. It is concluded that the change in the conformation of the DNA molecule, rather than the charge doubling, is the main driving force behind the sensed signal, even though both of these phenomena give signals of roughly the same order. It is also concluded that for low-density sensors, such as nanowire sensors, the variation in the positions of the DNA probes can cause the SNR to fall as low as 10, which severely compromises the operation of the sensor. Thus, there is a dire need for very well-controlled experimental environment to achieve reliable performance for biosensors, and the needs become more stringent as the device size decreases.

Chapter 6

SUMMARY, CONCLUSIONS, AND FUTURE WORK

6.1 Thesis Summary and Main Contributions

This thesis presented a theoretical study of several phenomena that are prevalent in DNA biosensors and that contribute greatly to the lack of control over fabrication of such sensors. The models presented in this thesis addressed the need for higher-dimensional modeling of biosensors and providing accurate geometries. Thus, reliable compact modeling of DNA biosensors is not an option at the current time, but complete physical modeling is necessary. We have shown that several often neglected effects, such as ionic crowding and permeability of the DNA molecules, can have large effects on the sensed outcome. These phenomena become more important as the size of the device shrinks, and with current quantum devices such as DNA nanowires and quantum dot sensors, such effects become extremely important.

The first main contribution of this work is to provide a computational framework for calculating performance parameters of interest for DNA biosensors, such as sensitivity, optimum electrolyte and bias conditions, and others. The finite-element method has been shown to possess the flexibility to deal with the complex geometries and sharp function gradients often encountered in biochemical systems. Furthermore, with the availability of several mean-field expressions for side-effects that affect the performance of the biosensor, incorporating them and studying their effects becomes an easy task in our models.

The second major contribution was the development of a small-signal AC model for the BioFET. As attention is directed towards detection by impedance changes, the

community desperately needs physical models for the transient behavior of the DNA BioFET. To our knowledge, our AC model is the first to be successfully developed and that can be used to predict the magnitude of impedance change and determine optimum frequency operation points for the BioFET.

Our third major contribution is the study of the effects of randomness in the distribution of DNA probes on the sensitivity of the biosensor. Although a similar study was conducted for distributions of dopants in a nanowire biosensor [176] , no such simulation was carried out for the DNA molecules themselves. Our simulation allowed us to propose a method of operation of the BioFET and an optimum biasing condition to maximize the signal-to- noise ratio, thus increasing the reliability of BioFET microarrays.

The fourth major contribution is to use simulations to identify the change of DNA conformation as a major factor that explains the operation of the BioFET. Monte-Carlo studies show that the distribution of charges for the single-stranded DNA is not hemispherical, as that would cause an anomalous negative signal. The single-stranded DNA molecule is shown to have a more vertical, mushroom shaped conformation with a non-uniform radial charge distribution. It is also shown that this distribution is only very slightly dependent on the reference electrode bias, but more on the solution concentration.

6.2 Future Work

The field of biosensors is one of the fastest growing fields in modern biomedical research, and many newer architectures and techniques of sensing are being discovered. Modeling will have an extremely deep impact on the success of these new designs. As the sensor sizes decrease, more detailed physics will be needed to properly model the operation of these sensors. Additionally, system-level simulations will be needed as these sensors are integrated with microfluidic chips into a fully integrated biosensor. Some of the identified possible areas of research in this field are listed here:

6.2.1 Quantum Modeling of Nanowire Sensors

As nanowire biosensors gain momentum in experimental research, the theoretical aspects are expected to follow closely. Nanowire sensors were proposed as superior biosensors due to their large surface area-to-volume ratio. This allows fewer DNA molecules to cause a severe change in the conductive properties of the nanosensor. However, although the main mode of sensing is often cited as field-effect, this is not obvious. In most cases, the native insulator layer that grows naturally on silicon is not altered. This insulator layer is thin enough to allow Faradaic reactions to take place. It is therefore possible that the DNA molecule alters the semiconductor by allowing Faradaic reactions to take place. To our knowledge, this possibility has not been explored in silicon nanowires.

Another issue when modeling nanowire sensors is that the classical transport equations no longer predict how the carriers transport current in the nanowire (except for thick nanowires in excess of 100 nm diameters). A quantum transport formulation is needed. Generally, this is done either using a Schrödinger-Poisson self-consistent solver and a phenomenological quantum transport model, or using a complete quantum transport model such as the NEGF formalism. The Schrödinger-Poisson solver is generally used for systems at equilibrium or very close to equilibrium. One would start by solving Schrödinger's wave equation for the eigenstates ψ :

$$\frac{-\hbar^2}{2m^*} \nabla^2 \psi(\mathbf{r}) - qV(\mathbf{r})\psi(\mathbf{r}) = \epsilon\psi(\mathbf{r}). \quad (6.1)$$

The eigenstates are filled according to Fermi's function, and their squared amplitudes give the charge density, taking into account the spin degeneracy:

$$n(\mathbf{r}) = -2 * \sum_i |\psi_{\epsilon_i}(\mathbf{r})|^2 f(\beta(\epsilon_i - E_F)), \quad (6.2)$$

where:

$$f(x) = (1 + \exp(x))^{-1}. \quad (6.3)$$

The calculated charge density is then used in Poisson's equation:

$$-\nabla \cdot (\epsilon_s \nabla V(\mathbf{r})) = q(n(\mathbf{r}) + N(\mathbf{r})), \quad (6.4)$$

and the potential is substituted back into Equation (6.1) until convergence. Once the potential and charge profiles have been calculated, a suitable transport model is used for current calculation. This can be, for example, Landauer's model:

$$I = \frac{2q}{h} \int (f(E - \mu_R) - f(E - \mu_L)) M(E) T(E) dE, \quad (6.5)$$

where μ_R and μ_L are the electrochemical potentials of the right and left contacts, respectively, $M(E)$ is the number of transmission modes, and $T(E)$ is the transmission function. Landauer's formula assumes a continuum of states due to the long channel dimension along the direction of current travel. Each one of these states, however, can manifest with different transverse modes, and this is captured by $M(E)$. Additionally, scattering centers at the contacts or within the device can cause change of the state of the electron. This is generally described by a scattering matrix.

For devices far from equilibrium, Landauer's approach does not suffice, but instead, the NEGF method needs to be employed. In the NEGF formulation, the Green's function for the Schrödinger equation is evaluated:

$$[E - H - \Sigma]G(\mathbf{r}, \mathbf{r}') = \delta(\mathbf{r} - \mathbf{r}'), \quad (6.6)$$

where H is the unperturbed Hamiltonian of the system, E is the energy, δ is the Dirac delta function, and Σ is the self-energy of different processes such as the contacts or the scattering centers within the device. The scattering self-energy allows for broadening of the energy spectrum, which models dissipative processes within the device. The Green's function has to be evaluated over many different energies of interest. Regardless of the type of numerical computation, the result can always be formulated as a matrix inversion problem:

$$\mathbf{G}(E) = [\mathbf{E}\mathbf{I} - \mathbf{H} - \mathbf{\Sigma}(E)]^{-1}. \quad (6.7)$$

With the Green's function evaluated, the carrier density can be calculated from:

$$\rho = \frac{1}{2\pi} \int_{-\infty}^{\infty} f(\beta(E - \mu)) \mathbf{A}(E) dE, \quad (6.8)$$

where the spectral function is defined as:

$$\mathbf{A}(E) = \mathbf{G}(E) \mathbf{\Gamma}(E) \mathbf{G}^\dagger(E), \quad (6.9)$$

and the broadening function is given by:

$$\mathbf{\Gamma}(E) = i(\mathbf{\Sigma}(E) - \mathbf{\Sigma}^\dagger(E)). \quad (6.10)$$

Using Equations (6.7)-(6.10), the density matrix is obtained, from which the carrier density can be obtained:

$$n(\mathbf{r}) = \text{Tr}(\rho). \quad (6.11)$$

The carrier density is inserted into Poisson's equation to calculate the self-consistent field, which is then used iteratively in the Hamiltonian of Equation (6.7) until convergence. After convergence, the current is calculated using Equation (6.5) with $M(E)=1$ and transmission coefficient given by the following formula:

$$T(E) = \text{Tr}(\mathbf{\Gamma}^1(E) \mathbf{G}(E) \mathbf{\Gamma}^2(E) \mathbf{G}^\dagger(E)). \quad (6.12)$$

One of the problems with using the NEGF formulation with FEM for the numerical simulation is the non-orthogonality of the basis functions in FEM. This requires modification of the basis to maintain the validity of all the previous equations. Specifically, the density matrix cannot be represented in the finite-element basis, but must instead use the following transformation:

$$\rho_{new} = \mathbf{L} \rho \mathbf{L}^\dagger, \quad (6.13)$$

where the matrix \mathbf{L} is the Cholesky decomposition (square root) of the FEM overlap matrix \mathbf{S} :

$$\mathbf{S} = \mathbf{L} \mathbf{L}^\dagger. \quad (6.14)$$

Quantum simulation requires formidable computation power for even simple geometries and systems, and often uses parallel supercomputers for the simulations.

However, such simulations become very necessary when the performance of nanoscale sensors is to be examined. These quantum simulations can be used with nanoelectrodes to determine electrode reaction kinetics. This can be useful for AC modeling of nanoscale sensors. The NEGF provides a framework of computation that is adaptable to many different transport scenarios, which makes it a very valuable tool. However, the details of the calculation of the different quantities involved depend on the nature of the problem.

6.2.2 Hybrid Methods

Even though the Finite-Element Method is adaptable to problems of varying geometries, it becomes inefficient when the molecular structure details are needed, in addition to bulk material models. Molecular geometries are often conveniently solved using ab-initio techniques that rely on non-localized basis functions, whereas the FE method uses localized shapes. To properly model nanosensors, the interface between the sensor and the molecules will have to be simulated using hybrid methods. There have been some attempts at this [177] , [178] . However, such methods have not been generalized to realistic geometries of DNA biosensors.

Another possibility at hybrid models is the use of a combined FEM model with molecular dynamics, depicted in Figure 6.1. This can be used to examine the fluctuations at the sensor's interfaces due to random thermal motion and particularly to examine the variations in the electrical double layer. The geometry is generally too large for a complete molecular dynamics simulation. Therefore, only a small portion of the domain will be modeled in MD, whereas the rest of the domain will be modeled using FEM. At the interface between these two domains, special boundary conditions must be used that allow energy and matter conservation across the interface. This method is very useful in simulation of biosensors and has been the subject of a few studies [179] , [180] .

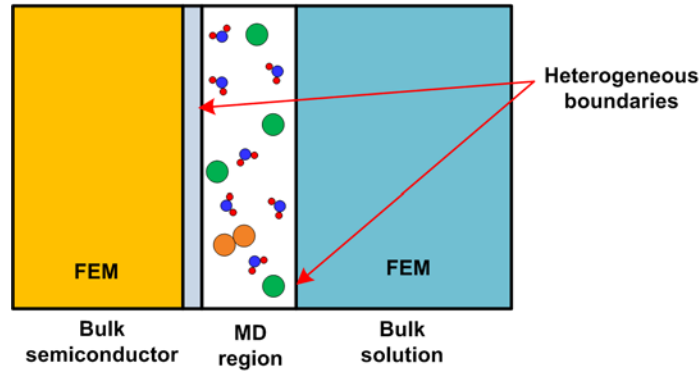


Figure 6.1 Possible hybrid FEM/MD model for the BioFET, emphasizing variations in the double layer through accurate MD simulations

The hybrid FEM/Ab-initio method requires special treatment of the boundaries. As shown in Figure 6.2, the non-localized elements belonging to the Ab-initio model diffuse into the FEM region. Thus, additional overlap integrals are required between the elements of the FEM model and those of the Ab-initio model. This can complicate proper boundary modeling. Additionally, the expressions for the derivatives of the Ab-initio elements are complicated, unlike those of the FEM elements. This makes Neumann conditions harder to implement in a systematic fashion, and special attention must be made to accommodate the boundary conditions.

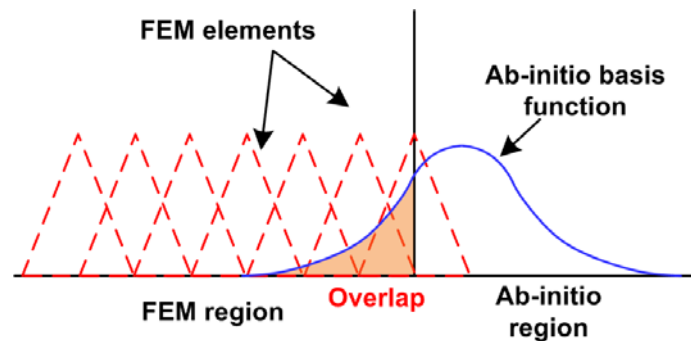


Figure 6.2 Illustration of the overlap between nonlocalized Ab-initio elements and FEM elements in a hybrid model

6.2.3 Modeling Reaction Kinetics of the Biosensor

In addition to higher sensitivity, an advantage of making the sensor smaller is to speed up the settling time for the biosensor. This is because of the fewer hybridization events needed to cause a significant signal modulation in the sensor. While nanosensors are generally assumed to provide the ultimate performance in low-concentration detection, the settling time can be prohibitively large for low target concentrations. This is because the probability of collision between the probe and a target is much smaller, and the target might be in an almost perpetual diffusion, in search of the probe. A good kinetic model would allow one to determine the optimum device geometry for best compromise between low detection limit and speedy settling time.

For hybridization of targets with higher concentrations, such as post-PCR DNA assays, the rate-determining step is usually the reaction kinetics. The more complicated the geometry of the molecule, the slower the reaction will progress. This is shown in Figure 6.3, wherein the hybridization can be hampered by intermediary partial hybridizations, or misalignments in the mutual orientation of the molecules. Mean-field models for hybridization have proven to be inaccurate because of many side-effects in the reaction of molecules with complex geometries [109], or the presence of secondary structures in the targets [181]. However, it is possible to extract mean-field parameters from a more detailed molecular dynamics model as a first step in the model. On the other hand, coarse-grained DNA models could be used directly to extract reaction constants, since they can be used in long time molecular dynamics simulations.

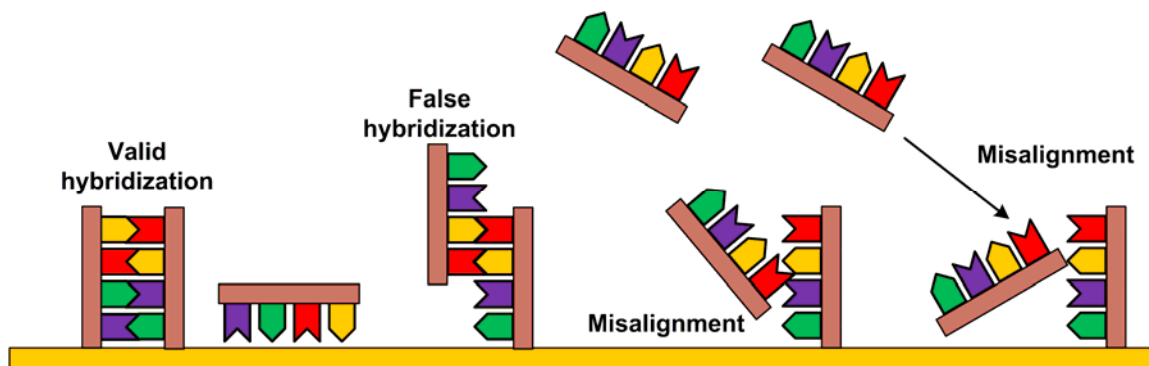


Figure 6.3 Different possibilities during DNA probe-target hybridization

Another possible area of research is to study the effects of the DNA sequence on the reaction rate. It is known that G-C bonds have lower bond energies than A-T bonds. Thus, it is expected that the hybridization of G-C rich molecules will be faster. However, this is not strictly the case. While the denaturation of G-C rich molecules is less likely, the hybridization rate is almost independent of the bases. This is most probably due to the fact that DNA probes initially recognize their targets at one or a few neighboring bases, and then zipper up, completing the hybridization. Thus, the orientation alignment is more important than the energetics of creating the bond. Molecular dynamics simulations can be used to determine the conditions under which such reasoning is valid. Additionally, research has shown [182] that the hybridization of the synthetic **Peptide Nucleic Acids** (PNA) to DNA targets is much stronger and more stable than DNA-DNA binding, and results in better hybridization yield. Molecular dynamics models can be used to examine the conditions under which such enhancements in performance are observed. This will lead to design and operation recommendations for best biosensor performance.

6.2.4 Modeling of Filtration and Purification of DNA

The DNA sensor is expected to be part of a total integrated system that includes pre-processing steps such as cell lysing and DNA extraction and purification chambers. It is critical to the successful readout of the DNA sensor that the targets are of similar length. Thus, any purification step, such as gel electrophoresis chambers, should provide high selectivity for DNA molecules of similar lengths. This depends on the applied voltage, dynamics of DNA in the viscous medium, and the presence of any nanoparticles in this chamber. It is necessary to couple molecular-level models of DNA with mean-field fluid mechanics equations to predict the performance of the filtration and transport process. An example of this was done in [183], wherein the variation in the electrophoretic mobility of DNA segments with the buffer solution used was examined. This was accomplished by simultaneously solving the mean-field Navier-Stokes equation and Poisson's equation in the presence of a detailed DNA molecule.

Another simulation was carried out in [184] , wherein the effect of different microfluidic channel structures on the transport of DNA was studied. Using a channel with a slotted structure, it was observed that the transported DNA could travel in a fast mode using the bulk of the solution, or along the slotted surface in a slower fashion that depends on the length of the DNA. This can be used in electrophoresis chambers for higher separation yield of DNA fragments of differing lengths. The simulations carried out here were a combination of mean-field Poisson's equation and a coarse-grained molecular-dynamics level simulation of the DNA molecules. In a similar study [185] , a simplified model for DNA electrophoresis through a porous membrane was studied. The effect of the pore sizes and the DNA length on the quality of the separation was deduced using this simulation.

Hydrodynamic simulations can also be used to help with the design of stable and reliable microfabricated reference electrodes. By using novel materials such as nanoporous membranes or other coatings, the diffusion process can be limited to potential-determining ions, while other ions are prevented. This causes a more stable potential on the reference electrode. Simulations can be used to study the effect of the electrode of choice, pore size, and distribution on the performance of the electrode. Thus, every aspect of the design of the biosensor can benefit from physical modeling, and such models will help guide the design and fabrication of the most stable integrated lab-on-chip.

References

- [1] K. Carrick, M. Barney, A. Navarro and D. Ryder, "The comparison of four bioluminometers and their swab kits for instant hygiene monitoring and detection of microorganisms in the brewery," *Journal of the Institute of Brewing*, Vol. 107, No. 1, pp. 31-37, 2001.
- [2] J. Wang, "Electrochemical glucose biosensors," *Chemical Review*, Vol. 108, No. 2, pp. 814-825, 2008.
- [3] J. Bartlett and D. Stirling, "A short history of the polymerase chain reaction," *Methods in Molecular Biology*, Vol. 226, No. 1, pp. 3-6, 2003.
- [4] M. Waleed Shinwari, "Modeling and simulation of electrochemical DNA biosensors in CMOS technology," Master Thesis, McMaster University, Department of Electrical and Computer Engineering, Hamilton, April 2007.
- [5] A. Chaubey and B. Malhotra, "Mediated biosensors," *Biosensors & Bioelectronics*, Vol. 17, No. 6-7, pp. 441-456, 2002.
- [6] C. Ding, F. Zhao, R. Ren, and J-M Lin, "An electrochemical biosensor for α -fetoprotein based on carbon past electrode of room temperature ionic liquid and gold nanoparticles," *Talanta*, Vol. 78, No. 3, pp. 1148-1154, 2009.
- [7] J. Lee, S. Hwang, J. Kwak, S. Park, S. Lee, and K-C Lee, "An electrochemical impedance biosensor with aptamer-modified pyrolyzed carbon electrode for label-free protein detection," *Sensors and Actuators B: Chemical*, Vol. 129, No. 1, pp. 372-379, 2008.
- [8] Y. Bo, W. Wang, J. Qi, and S. Huang, "A DNA biosensor based on graphene paste electrode modified with Prussian blue and chitosan," *Analyst*, DOI: 10.1039/c1an15084g, 2011.
- [9] M. Waleed Shinwari, D. Zhitomirsky, I. A. Deen, P. R. Selvaganapathy, M. J. Deen, and D. Landheer, "Microfabricated reference electrode and their biosensing applications," *Sensors*, Vol. 10, No. 3, pp. 1679-1715, 2010.
- [10] D. Baselt, G. Lee, and R. Colton, "Biosensor based on force microscope technology," *Journal of Vacuum Science and Technology B: Microelectronics and Nanometer Structures*, Vol. 14, No. 2, pp. 789-793, 1996.
- [11] A. Boisen and T. Thundat, "Design & fabrication of cantilever array biosensors," *Materials Today*, Vol. 12, No. 9, pp. 32-38, 2009.
- [12] V. Dauksaite, M. Lorentzen, F. Besenbacher, and J. Kjems, "Antibody-based protein detection using piezoresistive cantilever arrays," *Nanotechnology*, Vol. 18, No. 12, 125503 (5pp), 2007.
- [13] C. Ziegler, "Cantilever-based biosensors," *Analytical and Bioanalytical Chemistry*, Vol. 379, No. 7-8, pp. 946-959, 2004.
- [14] K. Besteman, J-O Lee, F. Wiertz, H. Heering, and C. Dekker, "Enzyme-coated carbon nanotubes as single-molecule biosensors," *Nano Letters*, Vol. 3, No. 6, pp. 727-730, 2003.
- [15] H. Sun, T. Choy, D. Zhu, W. Yam, and Y. Fung, "Nano-silver modified PQC/DNA biosensor for detecting E.coli in environmental water," *Biosensors and Bioelectronics*, Vol. 24, No. 5, pp. 1405-1410, 2009.
- [16] J. Pingarrón, P. Yáñez-Sedeño, A. González-Cortés, "Gold nanoparticle-based electrochemical biosensors," *Electrochimica Acta*, Vol. 53, No. 19, pp. 5848-5866, 2008.

- [17] S. Guo and S. Dong, "Biomolecule-nanoparticle hybrids for electrochemical biosensors," *Trends in Analytical Chemistry*, Vol. 28, No. 1, pp. 96-109, 2009.
- [18] X. Lu, H. Zhang, Y. Ni, Q. Zhang, and J. Chen, "Porous nanosheet-based ZnO microspheres for the construction of direct electrochemical biosensors," *Biosensors and Bioelectronics*, Vol. 24, No. 1, pp. 93-98, 2008.
- [19] F. Patolsky, G. Zheng, and C. Lieber, "Nanowire-based biosensors," *Analytical Chemistry*, Vol. 78, No. 13, pp. 4260-4269, 2006.
- [20] M. Basu, *et al*, "Nano-biosensor development for bacterial detection during human kidney infection: use of glycoconjugate-specific antibody-bound gold nanowire arrays (GNWA)," *Glycoconjugate Journal*, Vol. 21, No. 8-9, pp. 487-496, 2004.
- [21] S. Pal, E. Alocilja, and F. Downes, "Nanowire labeled direct-charge transfer biosensor for detecting bacillus species," *Biosensors and bioelectronics*, Vol. 22, No. 9-10, pp. 2329-2336, 2007.
- [22] G. Zheng, F. Patolsky, Y. Cui, W. Wang, and C. Lieber, "Multiplexed electrical detection of cancer markers with nanowire sensor arrays," *Nature Biotechnology*, Vol. 23, pp. 1294-1301, 2005.
- [23] C. Thaxton, D. Georganopouloy, and C. Mirkin, "Gold nanoparticle probes for the detection of nucleic acid targets," *Clinica Chimica Acta*, Vol. 363, No. 1-2, pp. 120-126, 2006.
- [24] T. Taton, C. Mirkin, and R. Letsinger, "Scanometric DNA array detection with nanoparticle probes," *Science*, Vol. 289, No. 5485, pp. 1757-1760, 2000.
- [25] M. Waleed Shinwari, M. J. Deen, and D. Landheer, "Study of the electrolyte-insulator-semiconductor field-effect transistor (EISFET) with applications in biosensor design," *Microelectronics Reliability*, Vol. 47, No. 12, pp. 2025-2057, 2007.
- [26] P. Bergveld, "The development and application of FET-based biosensors," *Biosensors*, Vol. 2, No. 1, pp. 15-33, 1986.
- [27] D-S Kim, J-E Park, J-K Shin, P. Kim, G. Lim, and S. Shoji, "An extended gate FET-based biosensor integrated with a Si microfluidic channel for detection of protein complexes," *Sensors and Actuators B*, Vol. 117, No. 2, pp. 488-494, 2006.
- [28] J. Liu, L. Liang, G. Li, R. Han, and K. Chen, "H⁺ISFET-based biosensor for determination of penicillin G," *Biosensors and Bioelectronics*, Vol. 13, No. 9, pp. 1023-1028, 1998.
- [29] J-K Shin, D-S Kim, H-J Park, and G. Lim, "Detection of DNA and protein molecules using an FET-type biosensor with gold as a gate metal," *Electroanalysis*, Vol. 16, No. 22, pp. 1912-1918, 2004.
- [30] T. Windbacher, V. Sverdlov, and S. Selberherr, "Biotin-streptavidin sensitive BioFETs and their properties," *Biomedical Engineering Systems and Technologies*, Vol. 52, No. 2, pp. 85-95, 2010.
- [31] H. Suzuki, A. Hiratsuka, S. Sasaki, and I. Karube, "Problems associated with the thin-film Ag/AgCl reference electrode and a novel structure with improved durability," *Sensors and Actuators B: Chemical*, Vol. 46, No. 2, pp. 104-113, 1998.
- [32] J-H Han, S. Park, H. Boo, H. Kim, J. Nho, and T. Chung, "Solid-state reference electrode based on electrodeposited nanoporous platinum for microchip," *Electroanalysis*, Vol. 19, No. 7-8, pp. 786-792, 2007.
- [33] F. Heuck and U. Stauffer, "Silver/silver-chloride electrode fabrication in closed microfluidic capillaries," *Microelectronic Engineering*, Vol. 87, No. 5-8, pp. 1383-1385, 2010.

- [34] M. J. Deen, M. Waleed Shinwari, D. Landheer, and G. Lopinski, "High sensitivity detection of biological species via the field-effect," *Proceedings of the 6th International Caribbean Conference on Devices, Circuits, and Systems*, pp. 381-385, 2006.
- [35] K-Y Park, M-S Kim, and S-Y Choi, "Fabrication and characteristics of MOSFET protein chip for detection of ribosomal protein," *Biosensors and Bioelectronics*, Vol. 20, No. 10, pp. 2111-2115, 2005.
- [36] T. Sakata, M. Kamahori, and Y. Miyahara, "DNA analysis chip based on field-effect transistors," *Japanese Journal of Applied Physics*, Vol. 44, pp. 2854-2859, 2005.
- [37] A. Hassibi and T. Lee, "A programmable 0.18- μ m CMOS electrochemical sensor microarray for biomolecular detection," *IEEE Sensors journal*, Vol. 6, No. 6, pp. 1380-1388, 2006.
- [38] K. Dorfman, "DNA electrophoresis in microfabricated devices," *Reviews of Modern Physics*, Vol. 82, pp. 2903-2947, 2010.
- [39] C. Zhang and D. Xing, "Miniaturized PCR chips for nucleic acid amplification and analysis: latest advances and future trends," *Nucleic Acids Research*, Vol. 35, No. 13, pp. 4223-4237, 2007.
- [40] H. Yin, K. Killeen, R. Brennen, D. Sobek, M. Werlich, and T. van de Goor, "Microfluidic chip for peptide analysis with an integrated HPLC column, sample enrichment column, and nanoelectrospray tip," *Analytical Chemistry*, Vol. 77, No. 2, pp. 527-533, 2005.
- [41] G. Hybarger, J. Bynum, R. Williams, J. Valdes, and J. Chambers, "A microfluidic SELEX prototype," *Analytical and Bioanalytical Chemistry*, Vol. 384, No. 1, pp. 191-198, 2006.
- [42] U-B Giang, M. King, and L. DeLouise, "Microfabrication of bubbular cavities in PDMS for cell sorting and microcell culture applications," *Journal of Bionic Engineering*, Vol. 5, No. 4, pp. 308-316, 2008.
- [43] S. Safari-Mohsenabad, P. R. Selvaganapathy, A. Derardja, and M. Deen, "Nanosheet formation by electrodeposition and its application to miniaturized reference electrodes," in *217th ECS Meeting, Vancouver*, 2010.
- [44] J. Liu, C-F Chen, S. Yang, C-C Chang, and D. DeVoe, "Mixed-mode electrokinetic and chromatographic peptide separations in a microvalve-integrated polymer chip," *Lab Chip*, Vol. 10, No. 16, pp. 2122-2129, 2010.
- [45] A. Ezkerra, L. Fernández, K. Mayora, and J. Ruano-López, "A microvalve for lab-on-a-chip applications based on electrochemically actuated SU8 cantilevers," *Sensors and Actuators B: Chemical* (in press), 2010.
- [46] P. Abgrall and A-M Gué, "Lab-on-chip technologies: making a microfluidic network and coupling it into a complete microsystem-a review," *Journal of Micromechanics and Microengineering*, Vol. 17, No. 5, R15-R49, 2007.
- [47] V. Srinivasan, V. Pamula, M. Pollack, and R. Fair, "A digital microfluidic biosensor for multianalyte detection," in *16th Annual International Conference on Micro-Electro-Mechanical Systems, Kyoto*, 2003.
- [48] J. Luong, K. Male, and J. Glennon, "Biosensor technology: technology push versus market pull," *Biotechnology Advances*, Vol. 26, No. 5, pp. 492-500, 2008.
- [49] "Analytical review of world biosensors market," *Frost & Sullivan*, 2010.
- [50] R. Wallace, J. Shaffer, R. Murphy, J. Bonner, T. Hirose, and K. Itakura, "Hybridization of synthetic oligonucleotides to ϕ_x 174 DNA: the effect of single base pair mismatch," *Nucleic Acids research*, Vol. 6, No. 11, pp. 3543-3558, 1979.

- [51] O. Tcherkasskaya, E. Davidson, M. Schmerr, and C. Orser, "Conformational biosensor for diagnosis of prion infections," *Biotechnology Letters*, Vol. 27, No. 9, pp. 671-675, 2005.
- [52] D. Lockhart, *et al.* "Expression monitoring by hybridization to high-density oligonucleotide arrays," *Nature Biotechnology*, Vol. 14, pp. 1675-1680, 1996.
- [53] F. Lucarelli, G. Marrazza, A. Turner, and M. Mascini, "Carbon and gold electrodes as electrochemical transducers for DNA hybridisation sensors," *Biosensors and Bioelectronics*, Vol. 19, No. 6, pp. 515-530, 2004.
- [54] E. Souteyrand, *et al.* "Direct detection of the hybridization of synthetic homo-oligomer DNA sequences by field effect," *Journal of Physical Chemistry B*, Vol. 101, No. 15, pp. 2980-2985, 1997.
- [55] K-S Song, *et al.* "Label-free DNA sensors using ultrasensitive diamond field-effect transistors in solution," *Physical Review E*, Vol. 74, 041919, 2007.
- [56] S. Yamaguchi, T. Shimomura, T. Tatsumo, and N. Oyama, "Adsorption, immobilization, and hybridization of DNA studied by the use of quartz crystal oscillators," *Analytical Chemistry*, Vol. 65, No. 14, pp. 1925-1927, 1993.
- [57] X. Wang, *et al.* "Label-free DNA sequence detection using oligonucleotide functionalized optical fiber," *Applied Physics Letters*, Vol. 89, 163901, 2006.
- [58] H. Peng, *et al.* "Label-free electrochemical DNA sensor based on functionalized conducting copolymer," *Biosensors and Bioelectronics*, Vol. 20, No. 9, pp. 1821-1828, 2005.
- [59] M. Waleed Shinwari, M. J. Deen, E. Starikov, and G. Cuniberti, "Electrical conductance in biological molecules," *Advanced Functional Materials*, Vol. 20, No. 12, pp. 1865-1883, 2010.
- [60] A. Peterson, R. Heaton, and R. Georgiadis, "The effect of surface probe density of DNA hybridization," *Nucleic Acids Research*, Vol. 29, No. 24, pp. 5163-5168, 2001.
- [61] M. Hegner, P. Wagner, and G. Semenza, "Immobilizing DNA on gold via thiol modification for atomic force microscopy imaging in buffer solutions," *FEBS Letters*, Vol. 336, No. 3, pp. 452-456, 1993.
- [62] J. Love, L. Estroff, J. Kriebel, R. Nuzzo, and G. Whitesides, "Self-assembled monolayers of thiolates on metals as a form of nanotechnology," *Chemical Reviews*, Vol. 105, No. 4, pp. 1103-1170, 2005.
- [63] M. Manning and G. Redmond, "Formation and characterization of DNA microarrays at silicon nitride substrates," *Langmuir*, Vol. 21, No. 1, pp. 395-402, 2005.
- [64] L. Henke, P. Piuino, A. McClure, and U. Krull, "Covalent immobilization of single-stranded DNA onto optical fibers using various linkers," *Analytica Chimica Acta*, Vol. 344, No. 3, pp. 201-213, 1997.
- [65] R. GhoshMoulick, X. Vu, S. Gilles, D. Mayer, A. Offenhäusser, and S. Ingebrandt, "Impedimetric detection of covalently attached biomolecules on field-effect transistors," *Physica Status Solidi A*, Vol. 206, No. 3, pp. 417-425, 2009.
- [66] C. Batchelor-McAuley, G. Wildgoose, and R. Compton, "The physicochemical aspects of DNA sensing using electrochemical methods," *Biosensors and Bioelectronics*, Vol. 24, No. 11, pp. 3183-3190, 2009.
- [67] M. Nakayama, T. Ihara, K. Nakano, and M. Maeda, "DNA sensors using a ferrocene-oligonucleotide conjugate," *Talanta*, Vol. 56, No. 5, pp. 857-866, 2002.
- [68] D. Nikolelis, U. Krull, J. Wang, and M. Mascini, *Biosensors for direct monitoring of environmental pollutants in field*. Dordrecht: Kluwer Academic Publishers, 1997.

- [69] W. Simon, "CPU transistor counts 1971-2008 & Moore's law"
http://en.wikipedia.org/wiki/File:Transistor_Count_and_Moore's_Law_-_2008.svg
- [70] A. Poghosian, A. Cherstvy, S. Ingebrandt, A. Offenhäusser, and M. Schöning, "Possibilities and limitations of label-free detection of DNA hybridization with field-effect-based devices," *Sensors and Actuators B*, Vol. 111-112, pp. 470-480, 2005.
- [71] M. J. Deen, M. Waleed Shinwari, J. C. Ranuárez, and D. Landheer, "Noise considerations in field-effect biosensors," *Journal of Applied Physics*, Vol. 100, 074703, 2006.
- [72] M. J. Deen, M. Waleed Shinwari, and D. Landheer, "Noise characteristics in integrated biosensing devices," *Proceedings on the 19th International conference on noise and fluctuations (ICNF2007)*, Vol. 922, pp. 399-404, 2007.
- [73] X. Gao, G. Zheng, and C. Lieber, "Subthreshold regime has the optimal sensitivity for nanowire FET biosensors," *Nano Letters*, Vol. 10, No. 2, pp. 547-552, 2010.
- [74] M. Waleed Shinwari, M. J. Deen, and P. R. Selvaganapathy, "Analytic modelling of biotransistors," *IET Circuits, Devices, and Systems*, Vol. 2, No. 1, pp. 158-165, 2008.
- [75] Encyclopædia Britannica 2007, "<http://www.britannica.com/EBchecked/media/106485/The-human-genome-is-made-up-of-approximately-three-billion>"
- [76] C. Bustamante, S. Smith, J. Liphardt, and D. Smith, "Single-molecule studies of DNA dynamics," *Current Opinion in Structural Biology*, Vol. 10, No. 3, pp. 279-285, 2000.
- [77] A. Baumgärtner, "Statics and dynamics of the freely jointed polymer chain with Lennard-Jones interaction," *Journal of Chemical Physics*, Vol. 72, No. 2, pp. 871-879, 1980.
- [78] M. Karplus and J. McCammon, "Molecular dynamics simulations of biomolecules," *Nature Structural Biology*, Vol. 9, pp. 646-652, 2002.
- [79] F. Jensen, *Introduction to Computational Chemistry*, Second Edition, West Sussex: Wiley, 2007.
- [80] http://nobelprize.org/nobel_prizes/chemistry/laureates/1998/illpres/computers.html
- [81] N. Kurita and K. Kobayashi, "Density functional MO calculation for stacked DNA base-pairs with backbones," *Computers and Chemistry*, Vol. 24, No. 3-4, pp. 351-357, 2000.
- [82] T. Natsume, Y. Ishikawa, K. Dedachi, T. Tsukamoto, and N. Kurita, "DFT study of the electronic properties of DNA-DNA and PNA-DNA double strands," *International Journal of Quantum Chemistry*, Vol. 106, pp. 3278-3287, 2006.
- [83] G. Cuniberti, L. Craco, D. Porath, and C. Dekker, "Backbone-induced semiconducting behavior in short DNA wires," *Physical Review B*, Vol. 65, 241314(R), 2002.
- [84] M. Young, B. Jayaram, and D. Beveridge, "Local dielectric environment of B-DNA in solution: results from a 14 ns molecular dynamics trajectory," *Journal of Physical Chemistry B*, Vol. 102, pp. 7666-7669, 1998.
- [85] A. Morriss-Andrews, J. Rottler, and S. Plotkin, "A systematically coarse-grained model for DNA and its predictions for persistence length, stacking, twist, and chirality," *The Journal of Chemical Physics*, Vol. 132, 035105, 2010.
- [86] S. Marrink, H. Risselada, S. Yefimov, D. Tieleman, and A. de Vries, "The MARTINI force field: coarse grained model for biomolecular simulations," *Journal of Physical Chemistry B*, Vol. 111, pp. 7812-7824, 2007.
- [87] E. Sambriski, D. Schwartz, and J. de Pablo, "A mesoscale model for DNA and its renaturation," *Biophysical Journal*, Vol. 96, No. 5, pp. 1675-1690, 2009.
- [88] J. Bockris and A. Reddy, *Modern Electrochemistry 1: Ionics*, Second Edition, New York: Plenum Press, 1998.

- [89] M. Kilic and M. Bazant, "Steric effects in the dynamics of electrolytes at large applied voltages. I. double-layer charging," *Physical Review E*, Vol. 75, 021502, 2007.
- [90] M. Kilic, M. Bazant, and A. Ajdari, "Steric effects in the dynamics of electrolytes at large applied voltages. II. Modified Poisson-Nernst-Planck equations," *Physical Review E*, Vol. 75, 021503, 2007.
- [91] I. Borukhov and D. Andelman, "Steric effects in electrolytes: a modified Poisson-Boltzmann equation," *Physical Review Letters*, vol. 79, No. 3, pp. 435-438, 1997.
- [92] K. Pitzer and G. Mayorga, "Thermodynamics of electrolytes II. Activity and osmotic coefficients for strong electrolytes with one or both ions univalent," *The Journal of Physical Chemistry*, Vol. 77, No. 19, pp. 2300-2308, 1973.
- [93] K. Dill, T. Truskett, V. Vlach, and B. Hribar-Lee, "Modeling water, the hydrophobic effect, and ion solvation," *Annual Review of Biophysics and Biomolecular Structure*, Vol. 34, pp. 173-199, 2005.
- [94] J. Koplik, J. Banavar, and J. Willemsen, "Molecular dynamics of Poiseuille flow and moving contact lines," *Physical Review Letters*, Vol. 60, No. 13, pp. 1282-1285, 1988.
- [95] J. McElroy, "Nonequilibrium molecular dynamics simulation of diffusion and flow in thin microporous membranes," *Journal of Chemical Physics*, Vol. 101, No. 6, pp. 5274-5280, 1994.
- [96] W. Schmickler, *Interfacial Electrochemistry*, New York: Oxford University Press, 1996.
- [97] C. Shenidorf and M. Rebhun, "A Freundlich-type multicomponent isotherm," *Journal of Colloid and Interface Science*, Vol. 79, No. 1, pp. 136-142, 1981.
- [98] A. Maczewski and M. Jaroniec, "A new isotherm equation for single-solute adsorption from dilute solutions on energetically heterogeneous solids," *Monatshefte für Chemie*, Vol. 114, No. 6-7, pp. 711-715, 1983.
- [99] O. Hamdaoui and E. Naffrechoux, "Modeling of adsorption isotherms of phenol and chlorophenols onto granular activated carbon. part I. two-parameter models and equations allowing determination of thermodynamic parameters," *Journal of Hazardous Materials*, Vol. 147, No. 1-2, pp. 381-394, 2007.
- [100] I. Quiñones and G. Guiochon, "Derivation and application of a Jovanovic-Freudlich isotherm model for single-component adsorption on heterogeneous surfaces," *Journal of Colloid and Interface Science*, Vol. 183, No. 1, pp. 57-67, 1996.
- [101] D. Misra, "New adsorption isotherm for heterogeneous surfaces," *Journal of Chemical Physics*, Vol. 52, No. 11, pp. 5499-5501, 1970.
- [102] D. Misra, "Adsorption on heterogeneous surfaces: a Dubinin-Radushkevich equation," *Surface Science*, Vol. 18, No. 2, pp. 367-372, 1969.
- [103] A. Khelifa, L. Benchehida, and Z. Derriche, "Adsorption of carbon dioxide by x zeolites exchanged with Ni^{2+} and Cr^{3+} : isothermic and isosteric heat," *Journal of Colloid and Interface Science*, Vol. 278, No. 1, pp. 9-17, 2004.
- [104] P. Nikitas, "A simple statistical mechanical approach for studying multilayer adsorption: extensions of the BET adsorption isotherm," *Journal of Physical Chemistry*, Vol. 100, No. 37, pp. 15247-15254, 1996.
- [105] R. Johnson and F. Arnold, "The Temkin isotherm describes heterogeneous protein adsorption," *BioChimica et Biophysica Acta*, Vol. 1247, No. 2, pp. 293-297, 1995.
- [106] D. Schwartz, "Mechanisms and kinetics of self-assembled monolayer formation," *Annual Reviews on Physical Chemistry*, Vol. 52, pp. 107-137, 2001.
- [107] A. Alsunaidi, "Adsorption of semiflexible chains on nanostriped surfaces: monte-carlo simulations," *Macromolecular Theory and Simulations*, Vol. 16, No. 1, pp. 86-92, 2007.

- [108] A. Vainrub and B. Pettitt, "Coulomb blockage of hybridization in two-dimensional DNA arrays," *Physical Review E*, Vol. 66, No. 4, 041905, 2002.
- [109] A. Halperin, A. Buhot, and E. Zhulina, "Sensitivity, specificity, and the hybridization isotherms in DNA chips," *Biophysical Journal*, Vol. 86, No. 2, pp. 718-730, 2004.
- [110] A. Pozhitkov, *et al*, "Tests of rRNA hybridization to microarrays suggest that hybridization characteristics of oligonucleotide probes for species discrimination cannot be predicted," *Nucleic Acids Research*, Vol. 34, No. 9, e66, 2006.
- [111] E. Carlon and T. Heim, "Thermodynamics of RNA/DNA hybridization in high-density oligonucleotide microarrays," *Physica A*, Vol. 362, No. 2, pp. 433-449, 2006.
- [112] C. Burden, Y. Pittelkow, and S. Wilson, "Adsorption models of hybridization and post-hybridization behaviour on oligonucleotide microarrays," *Journal of Physics: Condensed Matter*, Vol. 18, No. 23, pp. 5545-5565, 2006.
- [113] J. Bockris, A. Reddy, and M. Gamboa-Adelco, *Modern Electrochemistry 2A: Fundamentals of Electrode Processes*, Second Edition, New York: Plenum Press, 1998.
- [114] M. Lundstrom, *Fundamentals of Carrier Transport*, Second Edition, Cambridge: Cambridge University Press, 2000.
- [115] S. Datta, *Electronic Transport in Mesoscopic Systems*, Cambridge: Cambridge University Press, 1995.
- [116] S. Datta, *Quantum Transport: Atom to Transistor*, Cambridge: Cambridge University Press, 2005.
- [117] M. Naser, "Theoretical modeling of quantum dot infrared photodetectors", PhD Dissertation, McMaster University, Department of Electrical and Computer Engineering, Hamilton, 2009.
- [118] W. Jorgensen, "Transferable intermolecular potential functions for water, alcohols, and ethers. Applications to liquid water," *Journal of the American Chemical Society*, Vol. 103, No. 2, pp. 335-340, 1981.
- [119] W. Jorgensen, J. Chandrasekhar, J. Madura, R. Impey, and M. Klein, "Comparison of simple potential functions for simulating liquid water," *Journal of Chemical Physics*, Vol. 79, No. 2, pp. 926-935, 1983.
- [120] H. Berendsen, J. Grigera, and T. Straatsma, "The missing term in effective pair potentials," *Journal of Physical Chemistry*, Vol. 91, No. 24, pp. 6269-6271, 1987.
- [121] W. Jorgensen, "Revised TIPS for simulation of liquid water and aqueous solutions," *Journal of Chemical Physics*, Vol. 77, No. 7, pp. 4156-4163, 1982.
- [122] J. Abascal, E. Sanz, R. Fernández, and C. Vega, "A potential model for the study of ices and amorphous water: TIP4P/ice," *Journal of Chemical Physics*, Vol. 122, 234511, 2005.
- [123] F. Stillinger and A. Rahman, "Improved simulation of liquid water by molecular dynamics," *Journal of Chemical Physics*, Vol. 60, No. 4, pp. 1545-1557, 1974.
- [124] M. Mahoney and W. Jorgensen, "A five-site model for liquid water and the reproduction of the density anomaly by rigid, nonpolarizable potential functions," *Journal of Chemical Physics*, Vol. 112, No. 20, pp. 8910-8922, 2000.
- [125] J. Whiteman, *The Mathematics of Finite Elements and Applications*, London: Academic Press, 1973.
- [126] O. Zienkiewicz, *The Finite Element Method: Its Basis and Fundamentals*, Sixth edition, Amsterdam; London: Elsevier Butterworth-Heinemann, 2005.
- [127] M. Forray, *Variational Calculus in Science and Engineering*, New York: McGraw-Hill, 1968.

- [128] I. Babuška, "The finite-element method with Lagrange multipliers," *Numerische Mathematik*, Vol. 20, No. 3, pp. 179-192, 1973.
- [129] W. Dahmen and A. Kunoth, "Appending boundary conditions by Lagrange multipliers: analysis of the LBB conditions," *Numerische Mathematik*, Vol. 88, No. 1, pp. 9-42, 2001.
- [130] K. Ho-Le, "Finite-element mesh generation methods: a review and classification," *Computer-Aided Design*, Vol. 20, No. 1, pp. 27-38, 1988.
- [131] T. Davis, "Algorithm 832: umfpack v4.3-an unsymmetric-pattern multifrontal method," *ACM Transactions on Mathematical Software*, Vol. 30, No. 2, pp. 196-199, 2004.
- [132] C. Farhat and F-X. Roux, "An unconventional domain decomposition method for an efficient parallel solution of large-scale finite element systems," *SIAM Journal on Scientific Computing*, Vol. 13, No. 1, pp. 379-396, 1992.
- [133] D. Landheer, G. Aers, W. McKinnon, M. J. Deen, and J. C. Ranuárez, "Model for the field effect from layers of biological macromolecules on the gates of metal-oxide semiconductor transistors," *Journal of Applied Physics*, Vol. 94, No. 4, 044701, 2005.
- [134] C. Tien and J. Lienhard, *Statistical Thermodynamics*, Revised Printing, Washington: Hemisphere Publishing Corporation, 1979.
- [135] K. Stowe, *Introduction to Statistical Mechanics and Thermodynamics*, New York: Wiley, 1984.
- [136] C. Fung, P. Cheung, and W. Ko, "A generalized theory of an electrolyte-insulator-semiconductor field-effect transistor," *IEEE Transactions on electron devices*, Vol. ED-33, No. 1, pp. 8-18, 1986.
- [137] R. van Hal, J. Eijkel, and P. Bergveld, "A general model to describe the electrostatic potential at electrolyte oxide interfaces," *Advances in Colloid and Interface Science*, Vol. 69, No. 1-3, pp. 31-62, 1996.
- [138] G. Cerofolini, G. Ferla, and G. Spadini, "Determination of the state density at the Si-SiO₂ interface," *Thin Solid Films*, Vol. 68, No. 2, pp. 315-332, 1980.
- [139] M. Waleed Shinwari, M. J. Deen, and P. R. Selvaganapathy, "Finite-element modelling of biotransistors," *Nanoscale Research Letters*, Vol. 5, No. 3, pp. 494-500, 2009.
- [140] W. McKinnon and D. Landheer, "Sensitivity of a field-effect transistor in detecting DNA hybridization, calculated from the cylindrical Poisson-Boltzmann equation," *Journal of Applied Physics*, Vol. 100, No. 5, 054703, 2006.
- [141] M. Waleed Shinwari, M. J. Deen, and P. R. Selvaganapathy, "Optimization of DNA detection using FETs," in *1st Microsystems and Nanoelectronics Research Conference MNRC2008, Ottawa*, 2008.
- [142] J. Fritz, E. Cooper, S. Gaudet, P. Sorger, and S. Manalis, "Electronic detection of DNA by its intrinsic molecular charge," *Proceedings of the National Academy of Sciences*, Vol. 99, No. 22, pp. 14142-14146, 2002.
- [143] D. Lide, *CRC Handbook of Chemistry and Physics*, Student Edition, New York: CRC Press, 2004.
- [144] H. Cai, Y. Xu, P. He, and Y. Fang, "Indicator free DNA hybridization detection by impedance measurement based on the DNA-doped conducting polymer film formed on the carbon nanotube modified electrode," *Electroanalysis*, Vol. 15, No. 23-24, pp. 1864-1870, 2003.
- [145] Y. Fu, R. Yuan, L. Xu, Y. Chai, X. Zhong, and D. Tang, "Indicator free DNA hybridization detection via EIS based on self-assembled gold nanoparticles and bilayer two-dimensional 3-mercaptopropyltrimethoxysilane onto a gold substrate," *Biochemical engineering journal*, Vol. 23, No. 1, pp. 37-44, 2005.

- [146] A. Li, F. Yang, Y. Ma, and X. Yang, "Electrochemical impedance detection of DNA hybridization based on dendrimer modified electrode," *Biosensors and Bioelectronics*, Vol. 22, No. 8, pp. 1716-1722, 2007.
- [147] K. Ma, H. Zhou, J. Zoval, and M. Madou, "DNA hybridization detection by label free versus impedance amplifying label with impedance spectroscopy," *Sensors and Actuators B*, Vol. 114, No. 1-3, pp. 58-64, 2006.
- [148] M. Gheorghe and A. Guiseppi-Elei, "Electrical frequency characterization of DNA hybridization," *Biosensors and Bioelectronics*, Vol. 19, No. 2, pp. 95-102, 2003.
- [149] M. Waleed Shinwari and M. J. Deen, "Impedance modelling of FET-based biosensors," *Journal of the Electrochemical Society*, Vol. 158, No. 6, pp. J189-J194, 2011.
- [150] M. Kilic, M. Bazant, and A. Ajdari, "Steric effects in the dynamics of electrolytes at large applied voltages. II. Modified Poisson-Nernst-Planck equations," *Physical Review E*, Vol. 75, No. 2, 021503, 2007.
- [151] B. Corry, S. Kuyucak, and S. Chung, "Tests of continuum theories as models of ion channels. II. Poisson-Nernst-Planck theory versus Brownian dynamics," *Biophysical Journal*, Vol. 78, No. 5, pp. 2364-2381, 2000.
- [152] R. Impey, P. Madden, and I. McDonald, "Hydration and mobility of ions in solution," *Journal of Physical Chemistry*, Vol. 87, No. 25, pp. 5071-5083, 1983.
- [153] N. Agmon, "Proton solvation and proton mobility," *Israel Journal of Chemistry*, Vol. 39, pp. 493-502, 1995.
- [154] A. Poghossian, S. Ingebrandt, M. Abouzar, and M. Schöning, "Label-free detection of charged macromolecules by using a field-effect-based sensor platform: experiments and possible mechanisms of signal generation," *Appl. Phys. A*, Vol. 87, pp. 517-524, 2007.
- [155] Personal Communication with Dr. Sven Ingebrandt, *Electrochemical Society Conference ECS 219*, Montreal, 2011.
- [156] H. Weetall, "Biosensor technology what? where? when? and why?," *Biosensors and Bioelectronics*, Vol. 11, No. 2, pp. i-iv, 1996.
- [157] W. Saenger, *Principles of Nucleic Acid Structure*, New York: Springer, 1988.
- [158] A. Halperin, A. Buhot, and E. Zhulina, "Brush effects on DNA chips: thermodynamics, kinetics, and design guidelines," *Biophysical Journal*, Vol. 89, No. 2, pp. 796-811, 2005.
- [159] P. Flory, "Thermodynamics of high polymer solutions," *Journal of Chemical Physics*, Vol. 9, No. 8, pp. 660-661, 1941.
- [160] P. Flory, "Thermodynamics of high polymer solutions," *Journal of Chemical Physics*, Vol. 10, No.10, pp. 51-61, 1942.
- [161] R. Jernigan and P. Flory, "Distribution functions for chain molecules," *Journal of Chemical Physics*, Vol. 50, No. 10, pp. 4185-4200, 1969.
- [162] R. Chang and A. Yethiraj, "Osmotic pressure of salt-free polyelectrolyte solutions: a Monte Carlo simulation study," *Macromolecules*, Vol. 38, No. 2, pp. 607-616, 2005.
- [163] H. Meirovitch and H. Scheraga, "Computer simulation of the entropy of continuum chain models: the two-dimensional freely jointed chain of hard disks," *Journal of Chemical Physics*, Vol. 84, No. 11, pp. 6369-6375, 1986.
- [164] J. de la Torre, A. Jimenez, and J. Freire, "Monte Carlo calculation of hydrodynamic properties of freely jointed, freely rotating, and real polymethylene chains," *Macromolecules*, Vol. 15, No. 1, pp. 148-154, 1982.
- [165] J. Fried, *Polymer Science & Technology*, Second Edition, New Jersey: Prentice Hall, 2003.

- [166] J. Wilhelm and E. Frey, "Radial distribution function of semiflexible polymers," *Physical review Letters*, Vol. 77, No. 12, pp. 2581-2584, 1996.
- [167] A. Baumgärtner and K. Binder, "Monte Carlo studies on the freely jointed polymer chain with excluded volume interaction," *Journal of Chemical Physics*, Vol. 71, No. 6, pp. 2541-2545, 1979.
- [168] A. Baumgärtner, "Statics and dynamics of the freely jointed polymer chain with Lennard-Jones interaction," *Journal of Chemical Physics*, Vol. 71, No. 2, pp. 871-879, 1979.
- [169] M. Ullner and B. Jönsson, "A Monte Carlo study of titrating polyelectrolytes in the presence of salt," *Macromolecules*, Vol. 29, No. 20, pp. 6645-6655, 1996.
- [170] Y. Burak, G. Ariel, and D. Andelman, "Onset of DNA aggregation in presence of monovalent and multivalent counterions," *Biophysical Journal*, Vol. 85, No. 4, pp. 2100-2110, 2003.
- [171] M. Waleed Shinwari and M. J. Deen, "Geometric and conformational considerations in biotransistors," in *217th Electrochemical Society Meeting*, Vancouver, 2010.
- [172] Y. Tu, G. Stolovitzky, and U. Klein, "Quantitative noise analysis for gene expression microarray experiments," *Proceedings of the National Academy of Sciences*, Vol. 99, No. 22, pp. 14031-14036, 2002.
- [173] J. Mills and J. Gordon, "A new approach for filtering noise from high-density oligonucleotide microarray datasets," *Nucleic Acids Research*, Vol. 29, No. 15, e72, 2001.
- [174] D. Erickson, D. Li, and U. Krull, "Modeling of DNA hybridization kinetics for spatially resolved microchips," *Analytical Biochemistry*, Vol. 317, No. 2, pp. 186-200, 2003.
- [175] B. Palán, F. Santos, J. Karam, B. Courtois, and M. Husák, "New ISFET sensor interface circuit for biomedical applications," *Sensors and Actuators B*, Vol. 57, No. 1-3, pp. 63-68, 1999.
- [176] P. Nair and M. Alam, "Design considerations of silicon nanowire biosensors," *IEEE Transactions on Electron Devices*, Vol. 54, No. 12, pp. 3400-3408, 2007.
- [177] J. Guo, S. Datta, and M. Lundstrom, "Towards multi-scale modeling of carbon nanotube transistors," *International Journal of Multiscale Computational Engineering*, Vol. 2, pp. 257-277, 2004.
- [178] C. Heitzinger, N. Mauser, and C. Ringhofer, "Multi-scale modeling of planar and nanowire field-effect biosensors," *Siam Journal on Applied Mathematics*, Vol. 70, No. 5, pp. 1634-1654, 2010.
- [179] S. Ogata, E. Lidorikis, F. Shimojo, A. Nakano, P. Vashishta, and R. Kalia, "Hybrid finite-element/molecular-dynamics/electronic-density-functional approach to material simulations on parallel computers," *Computer Physics Communications*, Vol. 138, No. 2, pp. 143-154, 2001.
- [180] S. Xiao and T. Belytschko, "A bridging domain method for coupling continua with molecular dynamics," *Computer Methods in Applied Mechanics and Engineering*, Vol. 193, No. 17-20, pp. 1645-1669, 2004.
- [181] Y. Gao, L. Wolf, and R. Georgiadis, "Secondary structure effects on DNA hybridization kinetics: a solution versus surface comparison," *Nucleic Acids Research*, Vol. 34, No. 11, pp. 3370-3377, 2006.
- [182] K. Jensen, H. Ørum, P. Nielsen, and B. Nordén, "Kinetics for hybridization of peptide nucleic acids (PNA) with DNA and RNA studied with the BIAcore technique," *Biochemistry*, Vol. 36, No. 16, pp. 5072-5077, 1997.

- [183] S. Mazur, C. Chen, and S. Allison, "Modeling the electrophoresis of short duplex DNA: counterions K^+ and $tris^+$," *Journal of Physical chemistry B*, Vol. 105, No. 5, pp. 1100-1108, 2001.
- [184] M. Streek, F. Schmid, T. Dong, D. Anselmetti, and A. Ros, "Two-state migration of DNA in a structured microchannel," *Physical Review E*, Vol. 71, No. 1, 011905, 2005.
- [185] C. Liu, X. Xu, Q. Wang, and J. Chen, "Mathematical model for DNA separation by capillary electrophoresis in entangled polymer solutions," *Journal of Chromatography A*, Vol. 1142, No. 2, pp. 222-300, 2007.